Masterarbeit

zur Erlangung des Hochschulgrades
Master of Science
im Master-Studiengang Physik

Study of Polarization Fractions in the Scattering of Massive Gauge Bosons $W^{\pm}Z \to W^{\pm}Z$ with the ATLAS Detector at the Large Hadron Collider

Carsten Bittrich
geboren am 09.02.1989 in Görlitz

Technische Universität Dresden
Institut für Kern- und Teilchenphysik
Fachrichtung Physik
Fakultät Mathematik und Naturwissenschaften

27.04.2015

Eingereicht am 27. April 2015

1. Gutachter: Prof. Dr. M. Kobel
2. Gutachter: Prof. Dr. D. Stöckinger

Zusammenfassung

Die Streuung von massiven, elektroschwachen Eichbosonen ist ein Schlüsselprozess bei der Untersuchung der Elektroschwachen Symmetriebrechung. Vor allem die Streuung von longitudinal polarisierten Bosonen ist sensitiv darauf wie die Elektroschwache Symmetrie gebrochen ist, aber auch auf Erweiterungen des Standardmodells, da diese Streuung die Unitarität verletzen würde, ohne dass zum Beispiel ein standardmodellähnliches Higgsboson die Divergenzen aufhebt. Am Large Hadron Collider ist dieser Prozess im Endzustand mit den Zerfallsprodukten von zwei massiven Eichbosonen und zwei zusätzlichen Jets $VVjj$ messbar.

Um die longitudinalen Polarisationszustände aus den leptonischen Endzuständen aus einem $W^{\pm}Z$ Bosonenpaar zu extrahieren, werden verschiedene Methoden der Simulation von Ereignissen mit bekannter Bosonenpolarisation in verschiedenen Phasenräumen untersucht und validiert. Die Methode, den Prozess in die Produktion von Bosonen mit bekannter Polarisation und deren Zerfall mittels der „Narrow-Width"-Näherung (sinngemäß: Näherung der schmalen Breite) zu faktorisieren, wird gegenüber der verbreiteten Umgewichtungsmethode bevorzugt, da die Umgewichtungsmethode nach dem Einführen von Auswahlkriterien zusätzliche methodische Probleme aufweist. In der erstgenannten Methode wird die Produktion der Bosonen mit Whizard und MadGraph5_aMC@NLO simuliert. Das Programm WZdecay wird entwickelt um den Zerfall der Bosonen entsprechend deren Polarisation zu simulieren. Außerdem wird die Anwendbarkeit der vorausgesetzten Näherungen getestet.

Die Sensitivität verschiedener Observablen auf die Polarisation der Bosonen wird im $W^{+}Zjj$ Endzustand bei einer Schwerpunktsenergie von 13 TeV untersucht. Die höchsten Sensitivitäten auf den Polarisation des W^{+}-Bosons wurden dabei bei der Pseudorapidiät und dem transversalen Impuls des geladenen Leptons, das dem W^{+}-Boson zugeordnet wurde sowie der skalaren Summe dieses transversalen Impulses und dem fehlenden transversalen Impuls beobachtet. Im Fall der Polarisation des Z-Bosons erwiesen sich der Cosinus des Zerfallswinkels und die skalare Summe der transversalen Impulse der beiden zum Z zugeordneten Leptonen als am meisten sensitiv.

Abstract

The scattering of massive electroweak gauge bosons is an essential process for the study of the mechanism of electroweak symmetry breaking. Especially the scattering of longitudinally polarized bosons is sensitive to the way in which electroweak symmetry is broken and extensions of the Standard Model, since it would violate unitarity without e. g. a Standard Model Higgs boson canceling the divergences. At the Large Hadron Collider this process is measureable in the final states with decay products of two massive gauge bosons and two additional jets $VVjj$.

To extract longitudinal polarization modes in leptonic final states originating from a $W^{\pm}Z$ boson pair, different methods to obtain simulated events of known boson polarization are studied and validated in different phase spaces. The approach of factorizing the decay of the bosons and the production with defined helicity utilizing the narrow-width approximation is favored over the commonly used reweighting procedure due to methodical deficiencies after applying selection criteria. For the former the production process of bosons is simulated using Whizard and MadGraph5_aMC@NLO. The tool WZdecay is developed to simulate the leptonic decay according to the helicity of the boson and the validity of the applied approximation is tested.

The sensitivity of different observables to the polarization of the bosons are studied in the $W^{+}Zjj$ final state at a center-of-mass energy of 13 TeV. The highest sensitivity of different to the polarization of the W^{+} boson is found in the pseudorapidity as well as the transverse momentum of the charged lepton assigned to the W^{+} boson and the scalar sum of this transverse momentum and the missing transverse momentum. For the Z boson the cosine of its decay angle and the scalar sum of the transverse momenta of the lepton pair assigned to the Z boson are most sensitive.

Contents

Chapter 1

Introduction

Particle physics is the study of fundamental particles and their interactions. Some of its most driving questions go back to ancient Greek philosophers. What are the building blocks of matter? Are there fundamental particles?

However, it was only 120 years ago when mankind started finding answers to these questions. In 1897 the electron was the first particle to be discovered [1] which is still assumed to be fundamental. Since then many other particles have been discovered. Most of them were found to be composite, for instance the proton, discovered in 1917 by Ernest Rutherford [2], or the neutron, discovered in 1932 [3]. However, some particles are still assumed to be fundamental.

The theory describing all known particles is called the Standard Model of particle physics. The predictions of this theory are extremely accurate in describing the behavior of the known particles, thus making it one of the greatest intellectual achievements of mankind. Nevertheless, this theory is known to be incomplete. Some of the remaining problems the Standard Model cannot explain are dark matter, dark energy, or the matter-antimatter asymmetry. Over the years theorists have developed different theories that extend the Standard Model in an attempt to explain these deficiency. However, despite extensive searches no experimental evidence for these predictions has been found yet.

Historically many theories were confirmed by finding newly predicted particles. Most of these particles were found in the outcome of scattering processes. In order to achieve the necessary energies for the production of new particles, over the years many accelerators and detectors have been built. The most recent and most impressive being the Large Hadron Collider at CERN. With its circumference of about 27 km it is the largest machine ever built.

The observation of a boson compatible with the Standard Model Higgs boson in collisions produced at the Large Hadron Collider in 2012 [4, 5] was the latest and one of the most sought-after building blocks of the Standard Model. However, none of the additional particles predicted for instance by Supersymmetry [6], a widely favored theory beyond the Standard Model, was found.

Another way to find physics beyond the Standard Model is to precisely measure the properties of known particles and their interactions. Deviations from the Standard Model predictions indicate the effect of new physics. The data collected during the second run of the Large Hadron Collider will also offer a great opportunity to observe such deviations due to the previously unachieved center-of-mass energy of $\sqrt{s} = 13$ TeV. In addition, the expected amount of data will reduce the statistical uncertainty for these measurements and thus opens up the possibility to study previously unmeasured processes.

The scattering of longitudinally polarized states of massive gauge bosons is one of these processes of special interest. From a measurement of this process conclusions about the gauge structure of the Standard Model and the mechanism through which electroweak symmetry breaking proceeds can be deduced. For the first time the scattering of massive gauge bosons was measured in 2014 by the ATLAS collaboration in

the final state of two like-sign W bosons accompanied by two jets $W^{\pm}W^{\pm}jj$ [7]. Due to the two neutrinos in the leptonic final state a measurement of the polarization fractions is, however, very challenging in this final state. The $W^{\pm}Zjj$ final state is much easier to reconstruct and, consequently, the polarization fractions are better measurable.

This work aims to study and evaluate different tools necessary for a later study of polarization in the $W^{\pm}Zjj$ final state. In Chapter 2, the Standard Model of particle physics is introduced focusing on electroweak physics. In addition, polarization and predictions for the different polarization states are introduced. Chapter 3 motivates the importance of the scattering of massive gauge bosons and outlines the effects of the different polarization states in this process. In Chapter 4, the Large Hadron Collider and the ATLAS detector are reviewed. Different approaches to obtain simulated events with known polarization of the bosons are described in Chapter 5. These methods are then validated and compared in Chapter 6. In Chapter 7, a set of observables is introduced and its sensitivity to the boson polarization are analyzed. In addition, an outlook on the second run of the LHC is given in this chapter. Chapter 8 summarizes the results obtained in this thesis.

Chapter 2

Theoretical Foundation

One aim of physics is to find a theory able to make predictions about the outcome of processes. But this theory should not only explain which processes are realized. By including plausible explanations it should outclass purely phenomenological theories.

In particle physics such a theory should therefore be able to predict which particles exist and how they interact. The following chapter outlines this theory, examining some parts of special interest for this thesis in more detail. A more detailed description can be found in [8, 9].

2.1 Standard Model of particle physics

The *Standard Model of particle physics (SM)* is the most fundamental theory of particle physics. It describes elementary particles and their interactions. It was developed over the last few decades and expanded to incorporate previously unexpected measurements. This resulted in a theory not only in good agreement with measurements. The SM was also able to make predictions, many of which were confirmed. The presumably greatest success was the discovery of a Higgs boson in 2012 [4, 5]. In the 1960's theorists have developed a model to solve one of the main problems of the SM at the time. A side effect of this was the prediction of a new particle. This particle was found more than 40 years later. While maybe the most impressive, this prediction is only one out of many. Due to these successes the SM is widely accepted.

The SM is a non-Abelian relativistic quantum field theory based on local gauge symmetries. Three out of four of the fundamental forces can be described by the SM, the *electromagnetic*, the *weak*, and the *strong force*. This means their equations of motion can be derived from the full Lagrangian of the SM.

Local gauge symmetries imply invariance under certain transformations. For the SM, the set of these transformations can be denoted by

$$U(1)_Y \otimes SU(2)_L \otimes SU(3)_C \,. \tag{2.1}$$

The invariance causes the conservation of the weak hypercharge Y_W, the electric charge Q, the third component of the weak isospin T_3, and the color charge according to Noether's theorem [10]. To ensure local gauge invariance of the Lagrangian additional fields are introduced. These fields are interpreted as particles, the so called *gauge bosons*.

The remaining force is the gravitational force. It can be described by *general relativity*. Despite intensive studies for a long time currently no experimental evidence for models which unify the gravitational force with the SM, has been found. The gravitational force is very weak compared to the other three. Consequently, its influence at the scales of particle physics is very small. Therefore it is possible to neglect it at the energy scale studied in this thesis.

The SM distinguishes between two groups of elementary particles, fermions and

Generation	Fermion		Electric charge	Mass m in MeV
1st	e^-	electron	-1	0.511
	ν_e	electron-neutrino	0	$< 2 \cdot 10^{-6}$
	u	up	$2/3$	$2.3^{+0.7}_{-0.5}$
	d	down	$-1/3$	$4.8^{+0.7}_{-0.3}$
2nd	μ^-	muon	-1	105.7
	ν_μ	muon-neutrino	0	$< 2 \cdot 10^{-6}$
	c	charm	$2/3$	1275 ± 25
	s	strange	$-1/3$	95 ± 5
3rd	τ^-	tau	-1	1177
	ν_τ	tau-neutrino	0	$< 2 \cdot 10^{-6}$
	t	top	$2/3$	$(1.735 \pm 0.014) \cdot 10^5$
	b	bottom	$-1/3$	$(4.18 \pm 0.03) \cdot 10^3$

Table 2.1: List of fermions in the Standard Model sorted by generations. Each fermion has a corresponding anti-particle with opposite charges. Data from [11].

bosons.[1] *Fermions* are particles with half-integer spin[2] and follow the Fermi-Dirac statistics. Fermions can be divided according to their color charge. Color neutral Fermions are called *leptons*, *quarks* on the other hand have color charge. Also the (electric) charges[3] of leptons and quarks differ. While leptons carry integer electric charges, charges of quarks are always multiples of 1/3. However, only groups of quarks with integer charges are observable.

Six leptons and their corresponding anti-particles are currently known, divided into three generations. Each generation contains one charged, one neutral lepton, called neutrino, and the corresponding anti-particles. Particles of different generation differ only in their masses. The charged leptons are called electron e^-, muon μ^-, and tau τ^- with their anti-particles, anti-electron, or positron, e^+, anti-muon μ^+, and anti-tau τ^+. The SM contains also six pairs of quarks and their anti-quarks, divided into three generations. The different quark types, also referred to as flavors, are: up u, down d, charm c, strange s, top t, and bottom b. Each of these has three representatives each with a defined color charge (red, blue, green). Anti-quarks carry the corresponding anti-colors. By construction, states carrying only a color and its anti-color and those carrying a combination of all colors are color neutral. A list of all known fermions can be found in Table 2.1.

Bosons have integer spin and obey Bose-Einstein statistics. In the SM they are the mediators of the forces. The only exception of this is the Higgs boson, which is not connected to a force but is introduced via the Higgs mechanism as the excitation of the Higgs field. The SM-Higgs is the only fundamental particle with spin zero. The other bosons are called *gauge bosons* due to their introduction to conserve gauge symmetry. An alternative name is *vector bosons*, referring to their spin of one. In this thesis the electroweak bosons $W^\pm$, Z, and γ^* are denoted with V. A list of all known bosons is given in Table 2.2.

Charges describe how particles couple via an interaction. Neutral charges (0 or color neutral) imply an inability to participate in the corresponding interactions. The color charge corresponds to the strong interaction, mediated by gluons g. Gluons and quarks are the only particles with a color, i. e. able to interact via the strong force. A special property of this interaction called "confinement" leads to the fact, that single quarks are not observable, but only color neutral groups of them. The theory describing

[1] While this classification is also valid for composite particles, if not noted otherwise only elementary particles are considered in this thesis.

[2] In particle physics "natural units" are often used, demanding $c = \hbar = e = 1$ with unit charge e. This is also used throughout this thesis.

[3] The electric charge is often only referred to as charge.

	Boson	Electric charge	Spin	Interaction	Mass m in GeV
γ	photon	0	1	electromagnetic	$< 1 \cdot 10^{-27}$
$W^{\pm}$	W bosons	± 1	1	weak	80.385 ± 0.015
Z^0	Z boson	0	1	weak	91.188 ± 0.002
g	gluons	0	1	strong	0
H	Higgs	0	0		125.09 ± 0.24

Table 2.2: List of bosons in the Standard Model. Data taken from [11] and [12].

confinement and the strong force in general is *quantum chromodynamics (QCD)* [13–16].

The electric charge is connected to the electromagnetic force with the photon γ as gauge boson. This is described by *quantum electrodynamics (QED)*. Additionally, there is an extension of QED describing also the weak force. As electroweak gauge bosons are described by this theory, it will be looked at in more detail in the following section.

2.1.1 Electroweak theory

The *electroweak theory* was introduced by Glashow, Salam, and Weinberg [17–19] in the 1960s. It is a unified theory to describe the electromagnetic and weak force. A key aspect of this theory is the violation of parity conservation whereas pure QED or QCD processes obey parity conservation. In order to account for the violation, different chiralities have to be treated separately. Therefor, projection operators are applied on the fermion fields to obtain left- (L) or right-handed (R) fields, respectively

$$\psi_{L/R} = \frac{1}{2}\left(1 \mp \frac{\gamma^5}{2}\right)\psi \tag{2.2}$$

where ψ denotes the four-component Dirac fermion field and γ^5 the Dirac matrix (see Appendix A). These projections are chosen such that

$$\psi_L + \psi_R = \psi\,. \tag{2.3}$$

To achieve parity violation the weak isospin T_a is introduced. T_a can be represented as $T_a := \frac{1}{2}\sigma_a$ with the Pauli matrices σ_a (see Appendix A). $|T_a|$ is $\frac{1}{2}$ for left-handed fermion fields. They can be represented as $SU(2)_L$ doublets in terms of the third component of the weak isospin T_3. However, right-handed fields have $|T_a| = 0$. Thus, they are represented as singlets with $T_3 = 0$. For instance the first generation of leptons can be written as

$$L_L^j = \begin{pmatrix} \nu_{e,L} \\ e_L \end{pmatrix}, \qquad\qquad l_R = e_R. \tag{2.4}$$

Right-handed neutrinos have never been observed and are therefore not considered here. However, for quarks one has two singlets with right-handed fields in each generation, one for the up-type quark u_R and one for the down-type quark d_R. The doublet containing left-handed quark fields is denoted by Q_L^j. In addition, the weak hypercharge Y_W is introduced. The left-handed lepton fields L_L^j have $Y_W = -\frac{1}{2}$, the quark fields Q_L^j have $Y_W = +\frac{1}{6}$. It can be shown, that

$$Q = Y_W + T_3 \tag{2.5}$$

with the electric charge Q. For right-handed fermion fields follows $Y_W = Q$. This also shows the validity of the chosen representation in Equation (2.4). The first component of the $SU(2)_L$ doublet has $T_3 = +\frac{1}{2}$, hence $Q = 0$ and the second has $T_3 = -\frac{1}{2}$, hence $Q = -1$.

Using these left- and right-handed fields, the full electroweak theory can be formulated using the electroweak Lagrangian

$$\begin{aligned}\mathcal{L}_{\text{ew}} = &\sum_{j=1}^{3} i\bar{L}_L^j \gamma^\mu D_\mu L_L^j + i\bar{l}_R^j \gamma^\mu D_\mu l_R^j \\ &+ i\bar{Q}_L^j \gamma^\mu D_\mu Q_L^j + i\bar{u}_R^j \gamma^\mu D_\mu u_R^j + i\bar{d}_R^j \gamma^\mu D_\mu d_R^j \\ &- \frac{1}{4} W_{a,\mu\nu} W_a^{\mu\nu} - \frac{1}{4} B_{\mu\nu} B^{\mu\nu} \,. \end{aligned} \tag{2.6}$$

Here the Einstein summation convention is used, γ^μ denotes the Dirac matrices (see Appendix A) and the adjoint spinor is $\bar{\psi} := \psi^\dagger \gamma^0$. The index of summation j is used for the different fermion generations. D_μ denotes the covariant derivative

$$D_\mu = \partial_\mu + i g_W T_a W_\mu^a + i g_Y Y B_\mu \,. \tag{2.7}$$

The terms $W_{\mu\nu}^a$ and $B_{\mu\nu}$ are the field strength tensors of the gauge fields, defined as

$$B_{\mu\nu} = \partial_\mu B_\nu - \partial_\nu B_\mu \tag{2.8}$$

$$W_{\mu\nu}^a = \partial_\mu W_\nu^a - \partial_\nu W_\mu^a + g_W \epsilon^{abc} W_\mu^b W_\nu^c \,, \tag{2.9}$$

with the Levi-Civita symbol ϵ^{abc} and the gauge fields B_μ and W_μ^a.

The individual terms in Equation (2.6) can be interpreted as kinematic terms and interactions of particles. The first line represents kinematic terms of the leptons and the second line these of quark fields. Additionally, terms proportional to the adjoint fermion field, the fermion field, and the gauge field are introduced by the covariant derivative to ensure gauge symmetry. These terms can be interpreted as interactions of fermions with gauge bosons. The terms in the third line contain the kinematic terms of the gauge bosons. Since the SM is a non-Abelian theory, the field strength tensors of the W_μ^a (see Eq. (2.9)) gauge field is allowed to contain additional terms proportional to the coupling g_W. These terms are mixtures of the three W_μ^a fields and introduce self-interactions of the bosons. They will be discussed in more detail in Chapter 3.

$\mathcal{L}_{\text{ew}}$ is invariant under local gauge transformations of the group $U(1)_Y \otimes SU(2)_L$. These transformations can be interpreted as electroweak interactions and written as

$$\psi \to \exp\left(i(\alpha(x) Y_W + \beta_a(x) T_a)\right) \psi \,. \tag{2.10}$$

Here T_a can be interpreted as the generators of the $SU(2)_L$ group. Then Y_W is the generator of the $U(1)_Y$ group.

The invariance is ensured by introducing new gauge fields W_μ^a and B_μ with the corresponding gauge couplings g_W and g_Y. The gauge fields have to be transformed such that all α- or β_a-dependent terms cancel in the Lagrangian. These transformations are given by

$$W_\mu^a \to W_\mu^a - \frac{1}{g_W} \partial_\mu \beta_a - \epsilon_{abs} \beta_b \beta_c \,, \tag{2.11}$$

$$B_\mu \to B_\mu - \frac{1}{g_Y} \partial_\mu \alpha \,. \tag{2.12}$$

They are introduced in the covariant derivative and are contained in the terms of the third line in Equation (2.6). However, the gauge fields cannot be identified with the observed gauge bosons. This can easily be seen for the photon. The photon does not couple to neutrinos. All of the introduced gauge fields on the other hand do. Hence the physical fields must be combinations of the gauge fields. The Z boson's field (Z_μ) and the photon field (A_μ) are a linear combination of W_μ^3 and B_μ according to

$$\begin{pmatrix} A_\mu \\ Z_\mu \end{pmatrix} = \begin{pmatrix} \cos\theta_W & \sin\theta_W \\ -\sin\theta_W & \cos\theta_W \end{pmatrix} \begin{pmatrix} B_\mu \\ W_\mu^3 \end{pmatrix} . \tag{2.13}$$

The weak mixing angle θ_W is chosen such that A_μ decouples from the neutrinos and couples in the same way to left- and right-handed electrons. The Z boson is identified as a mixture of the gauge fields W_μ^3 and B_μ. B_μ couples equally to left- and right-handed fields, while W_μ^3 only couples to left-handed fermion fields. Thus, the Z boson does couple to left- and right-handed fermions, but not equally. The remaining gauge fields can be identified with the $W^\pm$ bosons, whose fields then can be represented as

$$W_\mu^\pm = \frac{1}{\sqrt{2}}(W_\mu^1 \mp iW_\mu^2)\,. \tag{2.14}$$

The $W^\pm$ bosons originate purely from the gauge fields of the $SU(2)_L$ group. Consequently, the $W^\pm$ bosons do not couple to right-handed fermions.

2.1.2 Electroweak symmetry breaking

The electroweak Lagrangian given in Equation (2.6) contains kinematic terms of the SM particles and their electroweak interactions. However, no mass terms are included. Mass terms contain only a particle's field in quadrature and a scalar function of the mass. These functions are known and differ for fermions and bosons. The resulting terms are

$$\mathcal{L}_{\text{fermion mass}} = m\bar{\psi}\psi \qquad \mathcal{L}_{\text{boson mass}} = -\frac{1}{2}M_V^2 V_\mu V^\mu\,. \tag{2.15}$$

Thus, a particle's mass can be "read of" the Lagrangian if terms proportional to its field in quadrature are present. These terms are not gauge invariant. Since observed particles, however, do have masses gauge symmetry must be broken.

In the 1960's Brout, Englert, and Higgs proposed [20–24] a mechanism to introduce mass terms while preserving global gauge invariance, the BEH or Higgs mechanism. Gauge symmetry is then spontaneously broken, called *electroweak symmetry breaking (EWSB)*.

To achieve this a complex scalar $SU(2)_L$ doublet field Φ, called BEH or Higgs field, with a weak hypercharge of $Y_W = \frac{1}{2}$ is introduced as

$$\Phi = \begin{pmatrix}\Phi^+\\ \Phi^0\end{pmatrix}. \tag{2.16}$$

This field transforms under the symmetry group $U(1)_Y \otimes SU(2)_L$ according to Equation (2.10) as

$$\Phi \to \exp\left(i\alpha(x)Y_W + i\beta_a(x)T_a\right)\Phi\,. \tag{2.17}$$

In addition, a potential is introduced as

$$V(\Phi) = -\mu^2\Phi^\dagger\Phi + \lambda\left(\Phi^\dagger\Phi\right)^2, \tag{2.18}$$

with the free scalar parameters μ, $\lambda > 0$. These terms are gauge invariant. Thus, it is allowed to add them to the Lagrangian in addition to the kinematic term as

$$\mathcal{L}_{\text{Higgs}} = |D_\mu\Phi|^2 + \mu^2\Phi^\dagger\Phi - \lambda\left(\Phi^\dagger\Phi\right)^2. \tag{2.19}$$

The parameters μ and λ are chosen such that the potential is minimal for

$$|\Phi_0|^2 = \frac{\mu^2}{2\lambda} =: \frac{v^2}{2}\,, \tag{2.20}$$

using the vacuum expectation value v. An infinite number of points fulfill this condition. They can be transformed into each other using gauge transformations. It is therefore possible to choose the vacuum state to be

$$\langle 0|\Phi|0\rangle = \frac{1}{\sqrt{2}}\begin{pmatrix}0\\ v\end{pmatrix}. \tag{2.21}$$

Picking one single state breaks the gauge symmetry. Thus, the vacuum state is not gauge invariant under $U(1)_Y \otimes SU(2)_L$ transformations. This state is, however, invariant under the transformation given by

$$\Phi \to \exp\left(i\theta_a(Y_W + T_a)\right)\Phi\,. \tag{2.22}$$

Using Equation (2.5) this can be identified as the $U(1)_{QED}$ symmetry of QED. Thus, the symmetry breaking can be described as

$$U(1)_Y \otimes SU(2) \to U(1)_{QED}\,. \tag{2.23}$$

The full first order expansion of the field Φ around the vacuum state can be parametrized as

$$\Phi = \begin{pmatrix} G_1(x) + iG_2(x) \\ \frac{1}{\sqrt{2}}(v + H(x)) + iG_3(x) \end{pmatrix}, \tag{2.24}$$

with real scalar fields H and G_i. The G_i are massless Goldstone fields as dictated by the Nambu-Goldstone theorem [25, 26]. The field H is the field of an additional scalar particle, called the Higgs boson H. This expansion can be transformed to the special case with vanishing G_i

$$\Phi = \frac{1}{\sqrt{2}}\begin{pmatrix} 0 \\ v + H(x) \end{pmatrix}. \tag{2.25}$$

This expansion can be identified with the general first order expansion around the vacuum state. Using this expansion in $\mathcal{L}_{\text{Higgs}}$ from Equation (2.19) adds several additional terms. The terms of the potential $V(\Phi)$ introduce a kinematic term, a mass term, and terms for three- and four-particle Higgs self-interactions. The mass of the Higgs boson is given by

$$m_H = \sqrt{2\lambda v} = \sqrt{2}\mu\,. \tag{2.26}$$

The term $|D_\mu \Phi|^2$ leads to mass terms for the gauge bosons given by

$$M_{W^\pm} = \frac{v g_W}{2}\,, \tag{2.27}$$

$$M_Z = \frac{v}{2}\sqrt{g_W^2 + g_Y^2}\,, \tag{2.28}$$

$$M_A = 0\,, \tag{2.29}$$

and interaction terms between the gauge bosons and the Higgs boson. Massless particles do not have a state of longitudinal polarization (see Section 2.2). The introduction of masses for the $W^\pm$ and Z boson gives each of them an additional degree of freedom. These additional degrees of freedom are identified with the Goldstone bosons g_i, which were removed by the gauge transformation. Thus, the longitudinally polarized states of the massive gauge bosons are deeply linked to the mechanism of electroweak symmetry breaking. This will be discussed further in Chapter 3.

Equation (2.27) can also be used to calculate v. Using the Fermi constant

$$G_F = \frac{g_W^2}{4\sqrt{2}M_W^2} \approx 1.16 \cdot 10^{-5}\ \text{GeV}^{-2}\,, \tag{2.30}$$

precisely measured in muon decays, leads to

$$v = 2\frac{M_{W^\pm}}{g_W} = \frac{1}{\sqrt{\sqrt{2}G_F}} \approx 246\ \text{GeV}. \tag{2.31}$$

This constrains one out of the two new free parameters μ and λ. The mass of the Higgs boson is not predicted by theory and can therefore be used to constrain the second parameter. Provided the Higgs boson, found in 2012, is a SM Higgs boson as introduced here, this mass is now also known to be [12]

$$m_H \approx 125.09\ \text{GeV}\,. \tag{2.32}$$

At this point the theory only gives masses to bosons. However, it is now possible to introduce interaction terms of fermion fields with the BEH fields "by-hand"

$$\mathcal{L}_{\mathrm{Y}} = \sum_{j=1}^{3} y_l^j \overline{L}_L^j \Phi l_R^j + y_u^j \overline{Q}_L^j i\sigma_2 \Phi u_R^j + y_d^j \overline{Q}_L^j \Phi d_R^j + h.\,c.\,. \tag{2.33}$$

The Yukawa couplings y_f are free parameters constrained by measurements of the fermion masses. Using the extension in Equation (2.25) this leads to mass terms for the fermions and interactions between fermions and the Higgs boson. The couplings for interactions with the Higgs boson are always proportional to the masses of the involved particles.

The electroweak part of the Lagrangian $\mathcal{L}_{\mathrm{ew}}$ (see Eq. (2.6)) combined with Higgs and Yukawa terms ($\mathcal{L}_{\mathrm{Higgs}}$, $\mathcal{L}_{\mathrm{Y}}$) can now explain electroweak physics and particle masses. Adding the Lagrangian for QCD $\mathcal{L}_{\mathrm{QCD}}$ (see i. e. [27]) one obtains the Lagrangian of the full Standard Model

$$\mathcal{L}_{\mathrm{SM}} = \mathcal{L}_{\mathrm{ew}} + \mathcal{L}_{\mathrm{Higgs}} + \mathcal{L}_{\mathrm{Y}} + \mathcal{L}_{\mathrm{QCD}}\,. \tag{2.34}$$

2.1.3 From Lagrangian to event rate

So called *Feynman rules* can be obtained from the SM Lagrangian $\mathcal{L}_{\mathrm{SM}}$. These rules describe the conversion of Feynman graphs into the *matrix elements* $\mathcal{M}$ of the corresponding processes. The full matrix element is given by the sum of all possible Feynman graphs with given initial and final states. For the full calculation also processes of higher order, i. e. including loops or additional radiations, have to be taken into account. Since this is an infinite series with in general decreasing influence, calculations are often performed at "leading order" (LO). This means only processes with the minimal number of vertices are considered.

This full matrix element is needed to calculate the rate for a final state in a specific phase space region. The calculation of this rate $\dot{N}$ is factorized in the following way

$$\dot{N} = \sigma \cdot \mathscr{L}\,. \tag{2.35}$$

One of factors is the cross section σ, which contains all process and phase space dependent variables. The luminosity $\mathscr{L}$ on the other hand incorporates all detector and experiment specific values.

The differential cross section $\mathrm{d}\sigma$ is independent of the experimental setup. It can be calculated from the matrix element $\mathcal{M}$ as

$$\mathrm{d}\sigma \propto \left|\mathcal{M}^2\right| \mathrm{d}\Phi\,. \tag{2.36}$$

Here $\mathrm{d}\Phi$ denotes a differential volume of the phase space.

The luminosity at the LHC (see Chap. 4) can be calculated as [28]

$$\mathscr{L} = \frac{N_B^2 n_b f_{\mathrm{rev}} \gamma_r}{4\pi\epsilon_n \beta^*} F\,. \tag{2.37}$$

Here N_B is the number of particles in each of the n_b bunches per beam. Furthermore, the revolution frequency f_{rev}, the relativistic gamma factor γ_r, the normalized transverse beam emittance ϵ_n, and the beta function at the collision point β^* are used. In order to correct for the crossing angle at the interaction point an additional factor F is introduced reducing the geometric luminosity.

2.2 Polarization

If the spin of a particle has a preferred direction the particle is polarized. In order to quantify this direction the helicity h is used. The helicity is defined as the projection of the particle's spin S onto the direction of its momentum $\vec{p}$

$$h = S \cdot \frac{\vec{p}}{|p|}\,. \tag{2.38}$$

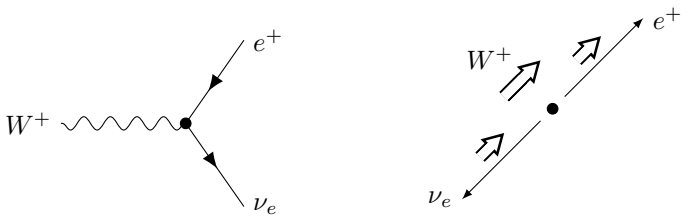

(a) Feynman diagram

(b) Directions of momenta and spins in boson rest frame

Figure 2.1: Leptonic decay of W^+ boson. In (a) the Feynman diagram is depicted. In (b) a sketch of the directions of the particles' momenta and spins is depicted. ν_e is left-handed, e^+ is right-handed.

Considering boosts along the particles momentum it can easily be seen that the helicity is not Lorentz invariant. Traveling at the speed of light, massless particles have an invariant helicity. In this case it can be identified with the particles chirality (see Eq. (2.2)). If not noted otherwise the helicity in the laboratory frame will be considered throughout this thesis.

Depending on the particle's spin different eigenvalues are possible. Since the focus of this work is laid on the polarization of particles with spin one, namely the $W^\pm$ and Z bosons, only this case is considered from here on. The possible helicity values for these particles are -1, 0, and 1. For massless bosons only -1 and 1 are allowed. This means the spin can either be parallel or anti-parallel to the momentum. A state with $h = 1$ has right-handed helicity and is called transversally polarized. Also states with $h = -1$ are transversally polarized, but with left-handed helicity. The polarization of states with $h = 0$ is referred to as longitudinal.

Throughout this thesis transversally polarized particles will be denoted with index T and longitudinal polarization with L. Note the second meaning of the index T as projection into the transverse plane. If this index is used for a particle (variable), it denotes the polarization (projection). Variables related to the helicity will be marked with the helicity eigenvalue as index.

2.2.1 Angular distributions

Conservation of the spin dictates relations of the helicity of a particle and the angular distributions of the decay products. These can be easily understood for the W boson since it does only couple to left-handed particles and right-handed anti-particles. Thus, in the rest frame of the boson the charged lepton is expected to escape in the direction of the spin for W^+ and in opposing direction for W^- (see Fig. 2.1).

This can be quantified using the *decay angle* θ^*_W. It is defined as the angle between the z-axis and the charged lepton's momentum in the $W^\pm$ rest frame. The z-axis is chosen as the direction of the momentum of the boson transfered to its rest frame. The exact frame in which the momentum of the boson is considered, is not unique. Usually the frame the helicity is defined in, is used. For the definition of an equivalent angle for the Z boson decay θ^*_Z the particle, i. e. not the anti-particle, of the decay products is used. This is illustrated in Figure 2.2.

For W^+ with right-handed helicity the boson's spin then points along the z-axis, resulting in a small decay angle θ^*_W. For opposite helicity large angles are expected. For longitudinally polarized W^+ bosons θ^*_W is expected to be approximately $\frac{\pi}{2}$. It can be shown, that the expected differential cross section for mixtures of the helicity states is [29]

$$\frac{1}{\sigma}\frac{\mathrm{d}\sigma}{\mathrm{d}\cos\theta^*_W} = \frac{3}{8}\left(1 \mp \cos\theta^*_W\right)^2 f_{-1} + \frac{3}{8}\left(1 \pm \cos\theta^*_W\right)^2 f_{+1} + \frac{3}{4}\sin^2\theta^*_W f_0 \qquad \text{for } W^\pm, \tag{2.39}$$

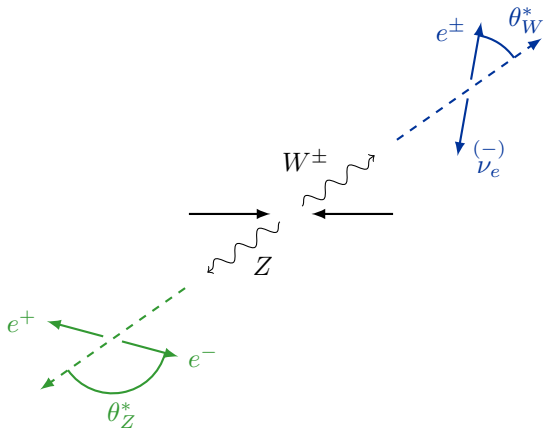

Figure 2.2: Definition of decay angle θ^*_V. Black lines (center) are depicted in frame used for definition of helicity, i. e. laboratory frame. Blue lines (upper right side) are boosted along $W^{\pm}$ boson's momentum to $W^{\pm}$ rest frame. Green lines (lower left side) are defined similarly for Z boson.

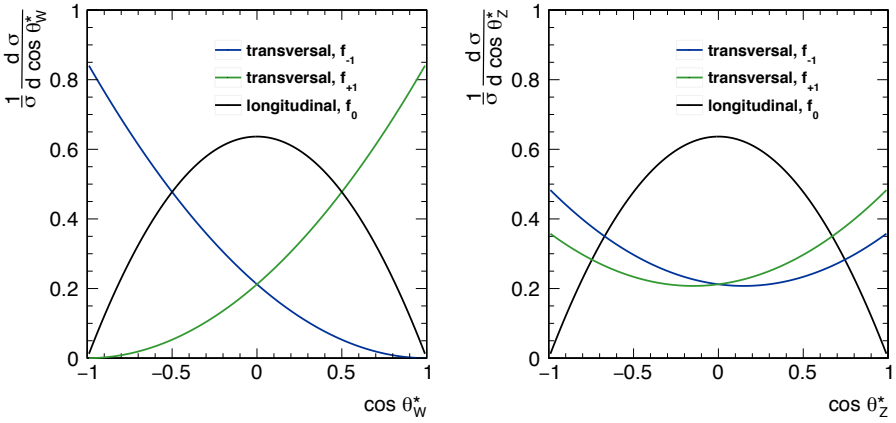

Figure 2.3: Normalized differential distributions of the cross section over the cosine of the decay angle of a W^+ boson (left) or Z boson (right) for bosons of given helicity. Helicity state -1 is shown in blue, 0 in black, and $+1$ in green.

with the fractions f_{-1}, f_0, and f_{+1} for the helicity denoted by the index. For the Z boson some differences arise from the additional coupling to right-handed fermions [29]

$$\frac{1}{\sigma}\frac{\mathrm{d}\sigma}{\mathrm{d}\cos\theta^*_Z} = \frac{3}{8}\left(1+\cos^2\theta^*_Z - \frac{2(c_L^2-c_R^2)}{(c_L^2+c_R^2)}\cos\theta^*_Z\right) f_{-1} + \frac{3}{8}\left(1+\cos^2\theta^*_Z + \frac{2(c_L^2-c_R^2)}{(c_L^2+c_R^2)}\cos\theta^*_Z\right) f_{+1} + \frac{3}{4}\sin^2\theta^*_Z f_0\,. \tag{2.40}$$

2.2.2 Spin density matrix

In order to fully describe a general spin system the helicity fractions are not sufficient. In addition to the quantum-mechanical effects, quantum-statistical effects also have to be taken into account.

The full spin density matrix ρ has to be used in order to consider these effects. A system of two vector bosons which occurs for instance in vector boson scattering, the density matrix ρ^{VV} can be represented by a complex 9×9 matrix. The diagonal elements of the density matrix ρ_{ii} can be interpreted as statistical probabilities to be in a certain state. For ρ^{VV} these states are the nine possible combinations of pure helicity. This

dictates $\mathrm{Tr}\,\rho^{VV}$ to be one and ρ_{ii}^{VV} to be positive and real. The complex off-diagonal elements account for the interference effects between the helicity amplitudes.

Summing over the helicity states of one of the particles one gets the one-particle spin density matrix ρ^V represented by a complex 3×3 matrix with the aforementioned properties. This summation is not sensitive to interference effects between the bosons anymore. However, all interferences between the single helicity states are fully included. The diagonal elements ρ_{ii}^V are then identical to the helicity fractions f_{-1}, f_0, and f_{+1} introduced in Equation (2.39).

Using ρ^W the full angular dependence of the cross section for the W decay can be calculated at NLO QCD from [30]

$$\frac{\mathrm{d}\sigma}{\mathrm{d}\left(p_\mathrm{T}(W)\right)^2\,\mathrm{d}y(W)\,\mathrm{d}\cos\theta_W^*\,\mathrm{d}\phi_W^*} = \sum_a g_a(\theta_W^*, \phi_W^*)\frac{3}{16\pi}\frac{\mathrm{d}\sigma^a}{\mathrm{d}\left(p_\mathrm{T}(W)\right)^2\,\mathrm{d}y(W)}\,. \quad (2.41)$$

Here $p_\mathrm{T}(W)$ is the transverse momentum of the W boson[4]. σ^a are the helicity cross sections corresponding to the nine elements of the spin density matrix ρ^W. ϕ_W^* denotes the azimuthal angle of the charged lepton in the W rest frame and the sum is applied over all nine helicity cross sections σ^a. Introducing the angular coefficients A_i ($i = 0, \ldots, 7$) as shown in [30] leads to

$$\begin{aligned}\frac{\mathrm{d}\sigma}{\mathrm{d}\left(p_\mathrm{T}(W)\right)^2\,\mathrm{d}y(W)\,\mathrm{d}\cos\theta_W^*\,\mathrm{d}\phi_W^*} = \frac{3}{16\pi}\frac{\mathrm{d}\sigma}{\mathrm{d}\left(p_\mathrm{T}(W)\right)^2\,\mathrm{d}y(W)} \cdot \Bigg(& (1+\cos^2\theta_W^*) \\ & + \frac{1}{2}A_0(1-3\cos^2\theta_W^*) + A_1 \sin 2\theta_W^* \cos\phi_W^* \\ & + \frac{1}{2}A_2 \sin^2\theta_W^* \cos 2\phi_W^* + A_3 \sin\theta_W^* \cos\phi_W^* \\ & + A_4 \cos\theta_W^* + A_5 \sin^2\theta_W^* \sin 2\phi_W^* \\ & + A_6 \sin 2\theta_W^* \sin\phi_W^* + A_7 \sin\theta_W^* \sin\phi_W^* \Bigg),\end{aligned} \quad (2.42)$$

with the unpolarized cross section σ. The angular coefficients A_i depend on the boson's p_T and y and are associated to the elements of the spin density matrix. Similar to the helicities they also depend on the chosen reference frame. At LO A_5, A_6, and A_7 vanish due to conservation of parity.

As it can be seen in Equation (2.42) the interference effects introduce a ϕ_W^* dependency. For efficiencies and acceptances uniformly distributed in ϕ_W^*, the cross section can be integrated over ϕ_W^* though. Integrating Equation (2.42) over $p_\mathrm{T}(W)$ and $y(W)$ leads to [31]

$$\frac{1}{\sigma}\frac{\mathrm{d}\sigma}{\mathrm{d}\cos\theta_W^*} = \frac{3}{8}\left((1+\cos^2\theta_W^*) + A_0\frac{1}{2}(1-3\cos^2\theta_W^*) + A_4\cos\theta_W^*\right). \quad (2.43)$$

Comparing Equation (2.43) with (2.39) yields

$$f_{-1}(y(W), p_\mathrm{T}(W)) = \frac{1}{4}\left(2 - A_0(y(W), p_\mathrm{T}(W)) \mp A_4(y(W), p_\mathrm{T}(W))\right), \quad (2.44)$$

$$f_{+1}(y(W), p_\mathrm{T}(W)) = \frac{1}{4}\left(2 - A_0(y(W), p_\mathrm{T}(W)) \pm A_4(y(W), p_\mathrm{T}(W))\right), \quad (2.45)$$

$$f_0(y(W), p_\mathrm{T}(W)) = \frac{1}{2}A_0(y(W), p_\mathrm{T}(W))\,, \quad (2.46)$$

where the upper sign applies for W^+ and the lower for W^-.

For a real detector the assumption of uniform distribution does not hold. Selection criteria and constraints arising from the detector composition Thus, have a large influence on measured angular coefficients and reconstructed θ_W^* [29].

For the Z boson the above Equations (2.41) to (2.46) are more complicated due to the additional coupling to right-handed fermions. For the studies shown in this thesis Equation (2.40) contains all necessary information.

[4]This notation will be used for all variables associated to specific particles throughout this thesis.

Chapter 3

Vector Boson Scattering

As introduced in Subsection 2.1.1 the SM Lagrangian $\mathcal{L}_{\text{SM}}$ contains terms for gauge boson self-interactions. They are predicted by the gauge structure of the SM. These self-interactions contain three-particle and four-particle vertices. This chapter introduces a process containing these self-interactions.

3.1 Process definition

The scattering of massive gauge bosons, also called vector boson scattering (VBS), is a process extremely sensitive to several predictions of the SM and models beyond the SM. Its small cross section makes it challenging to measure. Nevertheless, its clean signature allows a good suppression of backgrounds in some channels.

The pure scattering process contains several Feynman diagrams connecting two initial and two final state massive gauge bosons. All possible channels are depicted in Figure 3.1. Besides the four-particle vertex and s, u, and t channel[1] vector boson exchange, the Higgs boson can also be exchanged via s, u, or t channel diagrams. Depending on the studied boson combinations, some channels are forbidden due to violation of charge conservation. In addition to this constraint, all of the self-interactions contain at least two $W^{\pm}$ bosons. In this thesis, the focus is set on the scattering of $WZ \to WZ$. For this channel an exchange of vector bosons is only possible via a $W^{\pm}$ in an s or u channel diagram. The Higgs boson contributes only via a t channel diagram.

At the LHC (see Chapter 4), being a p-p collider, the vector bosons are radiated off by quarks. The outgoing quarks are only weakly deflected, resulting in a large rapidity difference and a large invariant mass of the resulting jets. Combined with small hadronic activity between these jets this is an important signature of vector boson fusion and vector boson scattering processes. This is exploited to tag events and for suppression of background processes. These jets are also called *tagging jets*.

After the scattering process the bosons decay into two fermions each. This results

[1] Throughout this thesis the following convention for the numbering of the incoming and outgoing particles is used. If a particle contributes as incoming and outgoing particle, the momenta of these particles are denoted with 1 and 3. If a second pair of momenta exists they are denoted by 2 and 4. Following this convention, it is possible to distinguish between an u and t channel diagram.

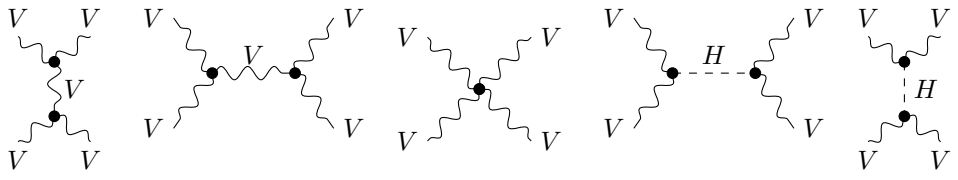

Figure 3.1: All possible Feynman diagrams connecting two initial and two final state massive gauge bosons.

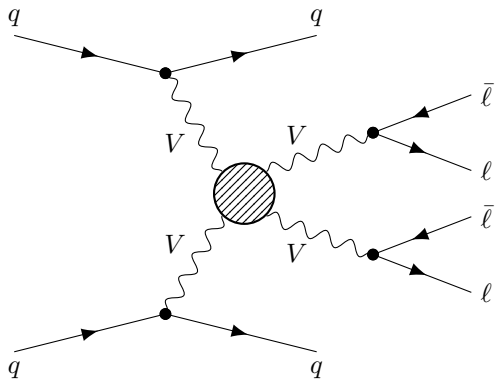

Figure 3.2: Schematic diagram of the vector boson scattering process at the LHC. The dashed circle stands for the possible interactions between the vector bosons shown in Figure 3.1.

in a final state containing the two tagging jets along with four fermions. A schematic diagram for this is depicted in Figure 3.2. Despite lower branching ratios, only the fully leptonic decays of the bosons are considered in this thesis. Decays containing τ leptons are also neglected. The advantages of restricted final state are a better suppression of backgrounds and a better momentum resolution for the decay products. The momentum resolution is especially vital in polarization measurements for the reconstruction of variables such as the decay angle θ_V^* (see Sec. 2.2). Thus, the final state is given by $\ell^{\pm}\nu_\ell\ell'^{-}\ell'^{+}jj$, where ℓ denotes either e or μ. Note that either the neutrino ν_ℓ or the lepton of same flavor ℓ have to be an anti-particle. For the sake of readability, this is not denoted for the neutrino, as it can be easily deduced from the charged lepton. This notation will be used throughout this thesis.

As quantum mechanics dictates, all diagrams leading to this final state contribute to the measurement. Some of these diagrams can be separated from the VBS process. The couplings of the VBS process are of the order $\mathcal{O}(\alpha_{EW}^6)$ at LO, i. e. it is a purely electroweak process. All purely electroweak processes with the same final state are not gauge invariantly separable from each other. This means all of these processes should be contained in the definition of the signal process. Some possible Feynman diagrams of other electroweak processes are depicted in Figure 3.3. These processes of order $\mathcal{O}(\alpha_{\mathrm{EW}}^6)$ are defined as signal and denoted by *WZjj-EW*. These diagrams can be divided into resonant and non-resonant diagrams. A diagram is called resonant if the final state fermions accompanying the tagging jets originate from two s channel vector bosons. In this case the diagram can be separated in the production of two vector bosons along with two jets and the decay of the vector bosons. This is not possible for non-resonant channels.

The definition of the signal process is restricted further in order to enhance the contribution of the VBS diagrams. An initial state bottom quark radiating of a $W^{\pm}$ boson causes a top quark resonance. This can only contribute to the VBS topology in higher orders due to the additional W radiated off during the decay of the top quark. However, other $\mathcal{O}(\alpha_{\mathrm{EW}}^6)$ diagrams, which also result in the $\ell^{\pm}\nu_\ell\ell'^{-}\ell'^{+}jj$ final state, contain a top quark resonance. Thus, the contribution of non-VBS diagrams is strongly enhanced if a bottom quark is present in the initial state. Since the initial state is not accessible experimentally it cannot be used for the process definition. However, the top quark resonance leads to final states containing a bottom quark. This is accessible, since bottom quarks can be distinguished from other quarks in the ATLAS detector (see Sec. 4.2) using b-tagging. Hence, diagrams with a bottom quark in the final state are not included in the signal process definition. These diagrams contribute to the background and are denoted by *tZj*.

There are other processes with the same final state of the order $\mathcal{O}(\alpha_{\mathrm{EW}}^4\alpha_{\mathrm{s}}^2)$. Some example processes are shown in Figure 3.4. These are separable and therefore defined

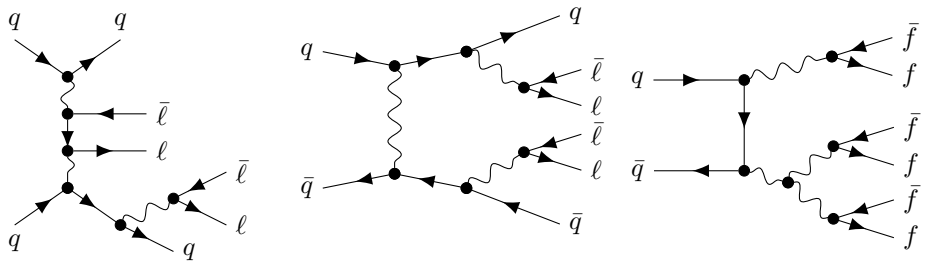

Figure 3.3: Feynman diagrams for some examples of non-VBS $\mathcal{O}(\alpha_{EW}^6)$ processes. These diagrams are not gauge invariantly separable from the VBS diagrams and are contained in the signal definition. Final states containing a bottom quark are defined as background. For processes with at least one bottom quark in the final state, the contribution of VBS diagrams is reduced due to a top quark resonance in the non-VBS diagrams. The diagram on the right-hand is an example for a so-called tri-boson diagram. One of the three produced bosons decays hadronically. Since each of the bosons can decay like this, decay products are not specified further.

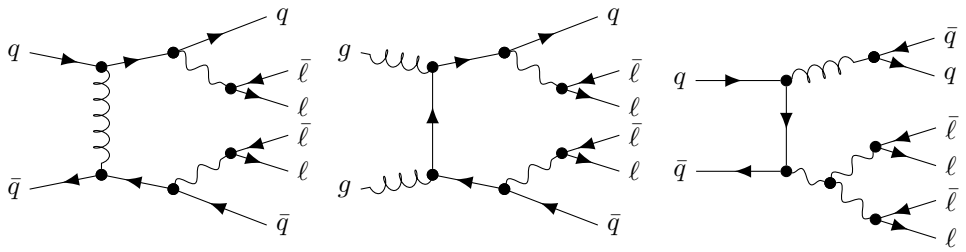

Figure 3.4: Feynman diagrams for some examples of $\mathcal{O}(\alpha_{EW}^4\alpha_s^2)$ background processes. These are gauge invariantly separable from the VBS diagrams and therefore contribute to the background.

as part of the background. This contribution to the background is called *WZjj-QCD*.

Other backgrounds can arise from detector effects such as leptons that were not reconstructed or other objects reconstructed as leptons. As a study of the background exceeds the scope of this work, this is not discussed further. A more detailed study of the background processes can be found in [32]. å

3.2 Polarization in vector boson scattering

As explained in Subsection 2.1.2 the massive gauge bosons acquire their masses via EWSB as described by the BEH mechanism. Without this symmetry breaking, the observed longitudinally polarized states, denoted by $W_{\mathrm{L}}^{\pm}$ and Z_{L} cannot be explained in the SM. Thus, these longitudinal states are deeply linked to the mechanism of EWSB and incorporate an important test of the SM. In the BEH mechanism they can be identified with the introduced Goldstone bosons. Although of interest in general, the difference between left- and right-handed helicities of the bosons is not connected to EWSB. Considering also the low cross section of the total VBS process, it is reasonable to omit distinguishing between the two transverse polarizations. Instead they will from here on be combined and denoted with V_{T}.

In the SM without EWSB the scattering of longitudinal bosons $V_{\mathrm{L}}V_{\mathrm{L}} \to V_{\mathrm{L}}V_{\mathrm{L}}$ violates unitarity. The cross section of the VBS process increases with the center-of-mass energy E_{cm}. Consequently, the cross sections exceed the unitarity limit for sufficiently large center-of-mass energy. According to scattering theory this can be interpreted as a probability for the process larger than one. This increase is solely caused by the scattering of the longitudinal states. In the BEH mechanism additional channels are

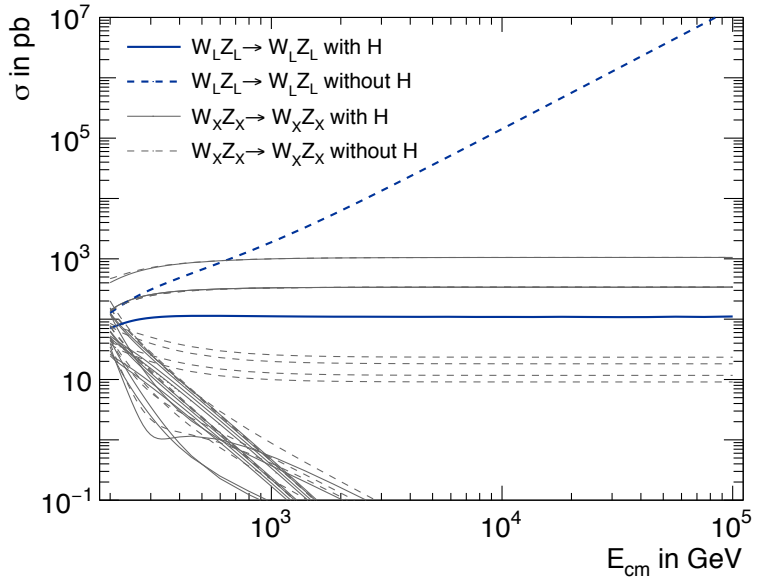

Figure 3.5: Dependency of the cross section of all polarization combinations of the scattering $WZ \to WZ$ on the center-of-mass energy E_{cm}. Full lines show the dependency including a SM-like Higgs boson and dashed lines for the case without a Higgs boson. Blue lines show the scattering of purely longitudinal boson polarization while all other polarization combinations are shown in gray. Cross sections are calculated using the MadGraph5_aMC@NLO Monte Carlo event simulator (see Chapter 5).

introduced via the Higgs boson. These cancel the increase leading to a constant cross section. This can be seen in Figure 3.5 for all different helicity combinations for the scattering $WZ \to WZ$. The violation of unitarity can be seen in the increase of the cross section over the center-of-mass energy. As shown only the scattering of purely longitudinal bosons in the Higgs-less case show this behavior.

In Figure 3.6 the scattering of longitudinal bosons is depicted for different boson combinations. It can be seen that the violation of unitarity occurs for all boson combinations. However, none of the processes including the SM Higgs boson shows this increase in σ.

This behavior motivates a more intensive study of the polarizations in VBS, in particular the scattering of longitudinal bosons.

3.2.1 Change of the polarization state in vector boson scattering

For the scattering process itself it is worthwhile to notice that the bosons are allowed to change their helicity while interacting with each other. The cross sections for this are depicted in Figure 3.7 for different boson combinations at a center-of-mass energy of the di-boson system of $E_{\text{cm}} = 250$ GeV. The mass of the SM Higgs boson is set to $m_H = 126$ GeV. In order to avoid divergences at least one of the final state bosons is required to have $p_{\text{T}} > 1$ GeV. It can be seen that the probability for a change in helicity is negligible if only $W^\pm$ bosons are involved. For $W^\pm W^\pm \to W^\pm W^\pm$ and $W^\pm W^\mp \to W^\pm W^\mp$ the spin properties can be assumed to be conserved while scattering.

In $W^\pm W^\pm \to W^\pm W^\pm$ the rows in Figure 3.7a which correspond to the $W^\pm_{\text{T}} W^\pm_{\text{L}}$ and $W^\pm_{\text{L}} W^\pm_{\text{T}}$ initial states, are identical. This behavior is expected since the bosons are identical and the order is arbitrary. The argument also applies to the columns with the corresponding final states. In this boson combination the difference between dominant and suppressed boson helicity combinations is the largest, spanning over ten orders of magnitude in cross section.

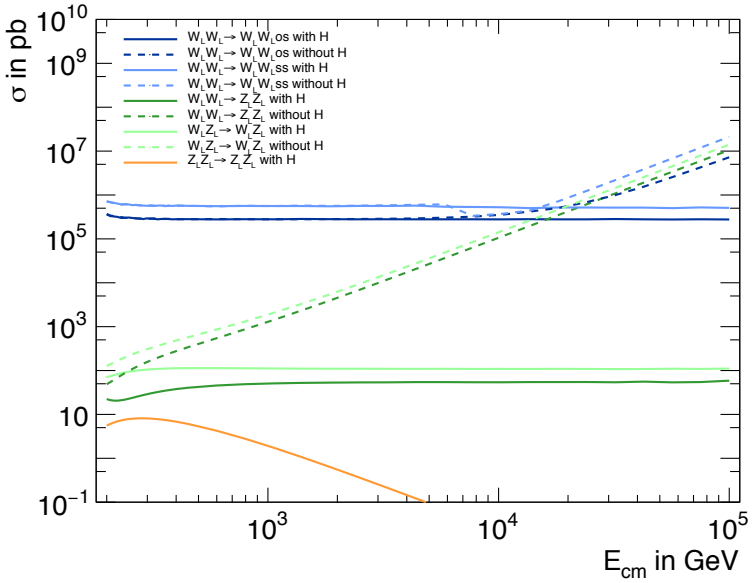

Figure 3.6: Dependency of the cross section of all boson combinations of the scattering of longitudinally polarized bosons $V_\mathrm{L}V_\mathrm{L} \to V_\mathrm{L}V_\mathrm{L}$ on the center-of-mass energy E_cm. Full lines show the dependency including a SM-like Higgs boson and dashed lines for the case without a Higgs boson. The scattering $Z_\mathrm{L}Z_\mathrm{L} \to Z_\mathrm{L}Z_\mathrm{L}$ is only allowed with a Higgs boson. Cross sections are calculated using the MadGraph5_aMC@NLO Monte Carlo event simulator (see Chapter 5).

The helicity conserving diagrams dominate also for the $W^\pm W^\mp \to W^\pm W^\mp$ scattering diagrams. The suppression of the other diagrams is much smaller, though. Again some identical diagrams are included, leading to identical results.

The $W^\pm Z \to W^\pm Z$ diagrams show a different behavior. In this case the diagrams where the polarizations of bosons swap dominate. The non-dominant boson helicity combinations are suppressed only in the order of 10^{-2}.

A possible explanation for the different dominant diagrams is illustrated in Figure 3.8. Here the spin does not change along the upper and lower boson line. In $W^\pm W^\pm \to W^\pm W^\pm$ scattering this corresponds to a conservation of the helicity states, as both bosons are identical. However, for the $W^\pm Z \to W^\pm Z$ scattering the bosons swap the lines. In this diagram the bosons exchange their polarization properties. In $W^\pm W^\mp \to W^\pm W^\mp$ scattering this diagram is not allowed, since no fundamental particle with electric charge two is known in the SM.

Applying the argument of constant spin along the boson line, on the t channel exchange diagrams explains the observed large cross sections for the dominant diagrams in pure W scattering. For both charge combinations a t channel exchange is possible for H, Z, and γ^*. However, for the $W^\pm Z \to W^\pm Z$ channel only a H exchange is allowed in a t channel diagram. The reduced number of allowed particles leads to a smaller contribution of this diagram. This argument requires the contribution of u and t channel diagrams to be dominant compared to s channel exchanges. As the center-of-mass energy was set to $E_\mathrm{cm} = 250$ GeV, a suppression of the s channel is reasonable since the propagating particle has to be off-shell with a large deviation from its resonance mass.

To quantify and compare the dominance, the relative contribution of the non-dominant diagrams to the sum over all diagrams which contribute to a given final state, are listed in Table 3.1. The strong suppression in the $W^\pm W^\pm \to W^\pm W^\pm$ scattering could be caused by the unavailable s channel exchange. Transfers of the polarizations seem to be more probable in this diagram.

It can be seen that the helicity combination of the initial state cannot be deduced from the helicity combination of the final state in $W^\pm Z \to W^\pm Z$.

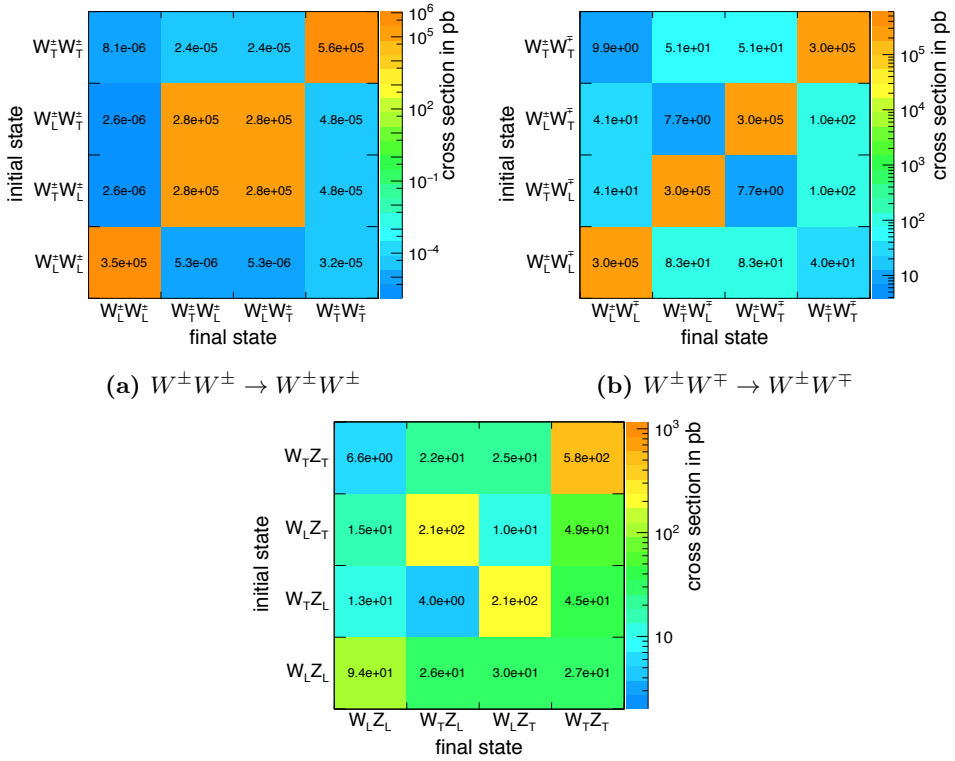

(a) $W^\pm W^\pm \to W^\pm W^\pm$ **(b)** $W^\pm W^\mp \to W^\pm W^\mp$

(c) $W^\pm Z \to W^\pm Z$

Figure 3.7: The cross section for all helicity combinations in the scattering of different boson combinations at a center-of-mass energy of the di-boson system of 250 GeV. One of the final state bosons is required to have a transverse momentum larger than 1 GeV in order to avoid divergences. On the x- (y)-axis all combinations for the final (initial) state bosons are plotted. Color represents the cross section in pb, which is also indicated in each bin. Uncertainties are not shown for the sake of readability. More precise values and uncertainties are shown in equivalent plots in Section D.1 in the Appendix. Cross sections are calculated using the MadGraph5_aMC@NLO Monte Carlo event simulator (see Chapter 5).

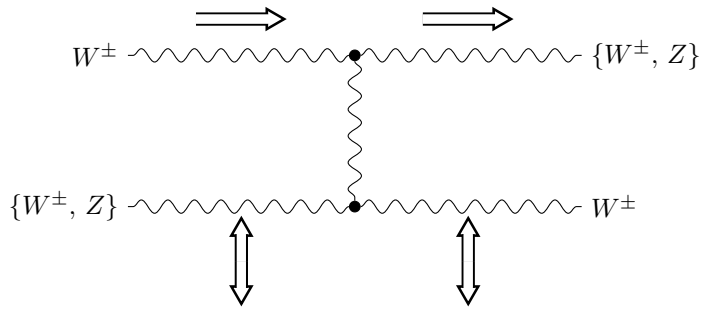

Figure 3.8: Feynman diagram for different boson combinations for the u channel exchange in the scattering process. Braces denote particles in the allowed channels. For $W^\pm W^\pm \to W^\pm W^\pm$ scattering Z and H exchanges are allowed. For the $W^\pm Z \to W^\pm Z$ scattering only an exchange of the $W\pm$ is allowed. The u channel for $W^\pm W^\mp \to W^\pm W^\mp$ is not allowed. The double arrows denote a special helicity combination.

Table 3.1: Ratio of the sum of cross sections of non-dominant diagrams over the sum of all cross sections contributing to a given final state. Note that for $W^{\pm}Z \to W^{\pm}Z$ this does not coincide with the off-diagonal diagrams in Figure 3.7c. Columns (rows) contain different helicity (boson) combinations. Identical diagrams contribute only once. Interferences between these diagrams are not considered. None of the cells or rows are expected to add up to one since each cell denotes a final state independent from the other cells.

	$V_\mathrm{L}V_\mathrm{L}$	$V_\mathrm{T}V_\mathrm{L}$	$V_\mathrm{L}V_\mathrm{T}$	$V_\mathrm{T}V_\mathrm{T}$
$W^{\pm}W^{\pm}$	$3.08 \cdot 10^{-11}$	$1.05 \cdot 10^{-10}$	$1.05 \cdot 10^{-10}$	$1.42 \cdot 10^{-10}$
$W^{\pm}W^{\mp}$	$1.71 \cdot 10^{-4}$	$4.72 \cdot 10^{-4}$	$4.72 \cdot 10^{-4}$	$4.72 \cdot 10^{-4}$
$W^{\pm}Z$	$2.66 \cdot 10^{-1}$	$1.95 \cdot 10^{-1}$	$2.3 \cdot 10^{-1}$	$1.72 \cdot 10^{-1}$

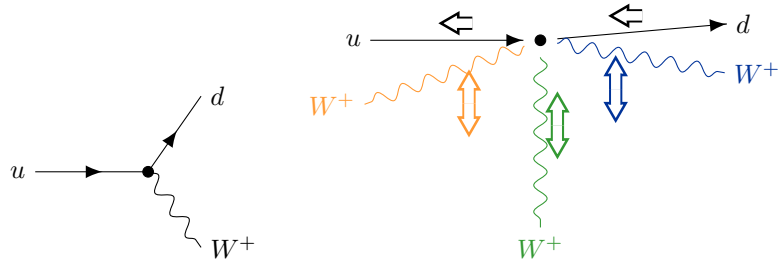

(a) Feynman diagram **(b)** Directions of momenta and spins

Figure 3.9: Kinematics of radiation process of a W^+ boson for an u in the initial state. (a) shows the Feynman diagram. In (b) the directions of spins and momenta are shown in the laboratory frame. The different colors correspond to different kinematics of the W^+ boson, only one of which is realized. Double arrows depict the direction of the spins.

3.2.2 Expected influence on kinematics

Another possibility to study the polarization of the initial bosons uses the kinematics of the tagging jets. The motivation for this is similar to the one used for the distribution of the decay angles. Some features of the kinematics of the radiated $W^{\pm}$ boson can be deduced since the $W^{\pm}$ only couples to left-handed quarks. In Figure 3.9 a schematic view of the radiation is shown. As the deflection of the quark is small the spin vectors of the initial and final state are similar. Therefore the projection of the bosons spin vector onto the direction of the initial quark's momentum is small. For high rapidities these directions of the boson spin correspond to longitudinal polarization. In the central region, though, this spin projection corresponds to transverse boson polarization. This should be reflected in the bosons transverse momentum and rapidity distributions. As the tagging jet balances the kinematics of the emitted boson in the transverse plane, their kinematics are also expected to discriminate between the bosons polarization.

The Z boson couples also to right-handed fermions, it does not mix between the chiralities, though. The kinematics should, therefore, be similar as for the $W^{\pm}$ boson.

Further expectations can be deduced from the *equivalence theorem* [33,34]. It states that the longitudinally polarized gauge boson states V_L can be replaced by the corresponding Goldstone boson at energies larger than the boson mass. The couplings of V_L then change and become proportional to the mass of the other particle participating in the interaction. Consequently, V_L decouple from light quarks. For instance it is therefore expected that the longitudinal states are suppressed in light quark initiated diagrams for high transverse momenta of the boson.

Chapter 4

Experimental Setup

This thesis is entirely based on simulated data without simulation of detector effects. However, selection criteria are chosen as in a specific analysis at the ATLAS detector [35]. Thus, a short overview of the ATLAS detector at the Large Hadron Collider is given below. Nevertheless, all results are expected to be valid regardless of specific detector design, as long as it covers the studied phase space.

4.1 The Large Hadron Collider

The *Large Hadron Collider* (LHC) [28] is the largest circular particle accelerator and collider ever built. It was constructed from 2000 to 2008 by the European Organization for Nuclear Research (CERN original French name "Conseil Européen pour la Recherche Nucléaire") near Geneva. The tunnel of the previous Large Electron-Positron Collider (LEP) was reused. Although some technical restrictions arose from this, financial benefits made the realization possible in the first place. The 26.7 km tunnel crosses the CERN facility on the Swiss side of the border, while the largest part of it is under French territory. The tunnel lies between 45 and 170 m beneath the surface with a slope of 1.4 %. The arcs are intersected by eight straight sections of a length of more than 500 m each hosting a possible interaction point.

The LHC is designed to collide counter-rotating beams of proton or heavy ion bunches. In order to accelerate and bend the beams two separate rings are required. The former LEP tunnel did not allow for completely separated beam lines without widening. This trade-off is a so called "two-in-one" solution. Both rings are contained within the same mechanical structure, sharing for instance the cryostat, but each ring has its own bore and set of coils. This limits flexibility but allows the beam-line to be much more compact. An overview of the LHC is depicted in Figure 4.1

Superconducting radio-frequency cavities are used to generate the magnetic fields needed to achieve the desired center-of-mass energies. In total 1232 dipoles and several thousand multi-pols are used to suppress dispersion and to accelerate and control the particle beams. The beams themselves consist of 2808 bunches each containing about $2 \cdot 10^{11}$ particles. About 20 to 40 single proton-proton collisions per bunch crossing occur simultaneously (pile-up). Distinguishing between these single events is crucial for good performance of the detectors.

The nominal maximum beam energy is limited by the peak dipole field. More advanced cooling techniques compared to previous accelerators allow a decrease in the run temperature from about 4 K to 1.9 K. This translates into an increase in field strengths from about 1.5 T to about 8 T. The resulting design center-of-mass energy for proton-proton collisions is 14 TeV. Several pre-accelerators are needed to inject particle bunches. For this, previous CERN colliders are used, namely the LINAC, the Proton Synchrotron BOOSTER, the Proton Synchrotron (PS), and the Super Proton Synchrotron (SPS). To provide enough statistics for the experiments the LHC was also designed to maximize luminosity (see Eq. (2.37)). The design luminosity is $\mathscr{L} =$

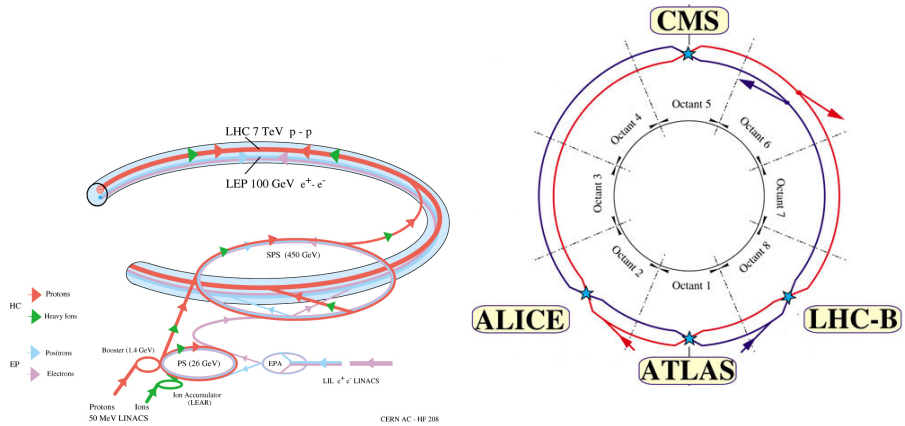

(a) Schematic representation of the injection complex. Graphic from [36].

(b) Main experiments and their interaction points. Graphic from [37].

Figure 4.1: Schematic overviews of the LHC acceleration complex.

$10^{34}\,\mathrm{cm^2 s^{-1}}$, resulting in an expected integrated luminosity of $\mathscr{L}_{\mathrm{int}} = 80 - 120\,\mathrm{fb}^{-1}$ per year.

The beams are not crossed at four of the eight possible interaction points in order to avoid their disruption. Instead they are used for acceleration and cleaning to ensure good beam quality. The other interaction points are used by the main experiments ATLAS [38], CMS [39], ALICE [40], and LHCb [41]. ATLAS (A Toroidal LHC ApparatuS) and CMS (Compact Muon Solenoid) are high luminosity detectors. Both are general purpose detectors, studying a wide range of predictions of the Standard Model and its extensions. The designs of LHCb (Large Hadron Collider beauty) and ALICE (A Large Ion Collider Experiment) on the other hand are optimized to study more specific research goals. LHCb is specialized on b-physics to study CP-violation in interactions of bottom quarks and thereby matter-antimatter asymmetry in the universe. ALICE focuses on heavy ion collisions to search for quark gluon plasma and test QCD. In addition to these experiments, TOTEM (TOTal Elastic and diffractive cross section Measurement) [42], LHCf (Large Hadron Collider forward) [43], and MoEDAL (Monopole and Exotics Detector At the LHC) [44] are hosted at the LHC.

Just nine days after the first complete beam line in September 2008 an accident occurred. A badly soldered contact caused excessive resistances. Heating up, the cavities in that area lost its superconducting properties. The rapid heating up lead to evaporation of helium. The expansion damaged a large part of the accelerator ring nearby. After a maintenance period for reparations, further testing, and enhancements to the magnets, the first proton-proton collisions were realized in March 2010 at a reduced proton beam energy of $E_{\mathrm{beam}} = 3.5$ TeV. After an increase to $E_{\mathrm{beam}} = 4$ TeV in 2012, the LHC ran until February 2013. The highly sophisticated operations during this time provided the necessary data for the discovery of a Higgs boson in 2012, and, thus, achieving one of the main goals of the LHC project. In order to fulfill further expectations LHC was shut down and updated from 2013 on to prepare for another increase of E_{beam} to 6.5 TeV and later to its design beam energy of 7 TeV. The second run period starts in summer of 2015 at a center-of-mass energy of 13 TeV. The integrated luminosity for this run ending in 2018 is expected to be about $\mathscr{L}_{\mathrm{int}} = 100\,\mathrm{fb}^{-1}$. After a short delay caused by a short circuit [45] in April 2015 p-p collisions at injection energy were performed [46] as well as the first successful acceleration of a single beam to $E_{\mathrm{beam}} = 6.5$ TeV [47].

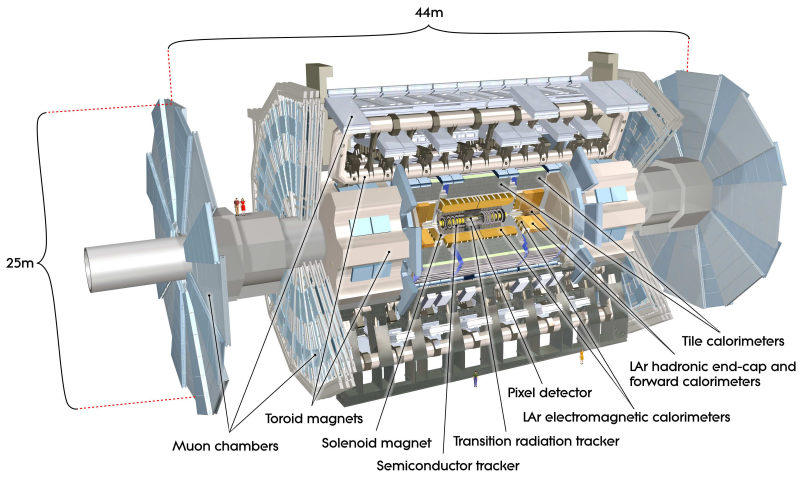

Figure 4.2: Cut-away view of the ATLAS detector [38].

4.2 The ATLAS detector

The ATLAS detector is one of the two general purpose detectors installed at the LHC. Its cylindrical geometry surrounds the beam pipe. It is forward-backward symmetric and has a length of 44 m and a height of 23 m. A schematic view of the ATLAS detector is shown in Figure 4.2.

ATLAS is designed to study a wide range of physics scenarios. Besides intensively testing of the SM, ATLAS searches for some new physics scenarios like supersymmetry and will study the characteristics of the Higgs boson. This dictates several requirements of the measuring capabilities of ATLAS. High spatial and momentum resolutions are essential for the reconstruction of particles and the measurement of their properties. Accurate charge identification allows for suppression of backgrounds. Excellent track reconstruction is important to suppress pile-up and for b-tagging. Large angular coverage combined with precise calorimetry are important to accurately reconstruct missing transverse momentum. Efficient triggering is required to find most interesting events while keeping data storage feasible.

The combination of these requirements lead to the design described below. Information is taken from reference [38] where not stated otherwise.

4.2.1 ATLAS coordinate system

For a consistent description of processes and analyses ATLAS uses a well-defined coordinate system. It is a right-handed cartesian coordinate system, with the center at the nominal interaction point. The z-axis points along the beam axis and the x- and y-axes lie in the transverse plane. The positive x direction is chosen to be towards the center of the LHC and the positive y-axis points upwards. Thus, also the positive z-axis is uniquely defined. The angles ϕ and θ and the distance R are defined as usual in a cylindrical coordinate system. The azimuth angle ϕ is defined as the angle from the positive x-axis to the projection of a given point into the transverse plane. The polar angle θ is the angle, which is spanned from the positive z-axis to the point itself. R is the distance from the origin of the coordinate system to the projection in the transverse plane. At a proton-proton collider the z component of the total initial momentum is not known, since the momentum fraction of quarks and gluons constituting the proton cannot be predicted. Therefore the center-of-mass frame of the hard interaction process is boosted along the z-axis with respect to the laboratory frame. Observables which are invariant under boosts along this axis are necessary to compare events. The azimuth angle and projections onto the transverse plane, for instance the transverse momentum p_{T} fulfill this condition. These projections are denoted with the index "T" from here on. The polar angle on the other hand is not invariant. In order to evaluate the corresponding

information of a particle the *rapidity* y is introduced. It is defined as

$$y := \frac{1}{2} \ln \left(\frac{E + p_z}{E - p_z} \right), \tag{4.1}$$

where p_z denotes the z component of the particle's momentum. The rapidity itself is also not invariant under boosts along the z-axis, but rapidity differences Δy are. In order to simplify calculations the *pseudorapidity* η is introduced as

$$\eta := -\ln \tan \left(\frac{\theta}{2} \right). \tag{4.2}$$

For massless particles, η is equal to the rapidity, hence their differences are also invariant. This does not apply for non-negligible masses. The rapidity should be used instead in particular for massive bosons and jets at the usual energy scales. Another commonly used variable is the *angular distance* ΔR defined as

$$\Delta R := \sqrt{(\Delta\phi)^2 + (\Delta\eta)^2}, \tag{4.3}$$

where $\Delta\phi$ ($\Delta\eta$) denotes difference in the azimuthal angles (pseudorapidity).

The initial momentum of the hard process is not fully known. However, the transverse momenta of the initial state particles are negligible. Thus, momentum conservation dictates the transverse momenta of all particles of each single collision to balance each other. A possible imbalance, also called missing transverse momentum $p_{\mathrm{T}}^{\mathrm{miss}}$, can be caused by momentum mismeasurement or undetected particles. Candidates for undetected particles are neutrinos, which are not measurable by the ATLAS detector, or any particle leaving the detector outside its acceptance region.

4.2.2 Inner Detector

A precise track reconstruction is the foundation of a good measurement. It allows amongst others for pile-up rejection, momentum measurement, vertex reconstruction, charge identification, and b-tagging. At the ATLAS detector the track reconstruction is realized by the *Inner Detector* (ID). The ID is closest to the interaction point and only a few centimeters away from the beam line. The number of particles detected in each bunch crossing at design luminosity in the pseudorapidity region of $|\eta| < 2.5$ is in the order of 1000.

The ID (see Figure 4.3a) is axially symmetrical around the beam axis and interspersed with a 2 T magnetic field parallel to the beam axis. This bends the tracks of particles according to their charge. The curvature is used to calculate the charge and transverse momentum of the particle.

The innermost parts of the ID are the *Pixel Detector* and the *SemiConductor Tracker (SCT)*. They cover a region of $|\eta| < 2.5$ and are devoted to precision tracking. In the barrel region, they are built-up in cylindrical layers around the beam axis, and, in the end-cap of discs parallel to the transverse plane. The pixel tracker consists of silicon pixel layers segmented in the R-ϕ plane and z (R) in the barrel (end-cap) region. It reaches accuracies of 10 μm in the R-ϕ plane and 115 μm in the z direction. Each charged particle causes up to three hits in the pixel detector. In the SCT there are up to eight hits. The strips of the SCT are parallel to the beam direction and have an accuracy of 17 μm in the R-ϕ plane and 580 μm in the z direction.

The SCT is encased by the *Transition Radiation Tracker (TRT)*, which covers the region, where $|\eta| < 2.0$. The TRT provides only R-ϕ information with an accuracy of 130 μm. This inferior accuracy is compensated by a larger number of hits of up to 36 and longer track lengths. The TRT also contributes significantly to the track reconstruction.

4.2.3 Calorimeter System

The missing transverse momentum $p_{\mathrm{T}}^{\mathrm{miss}}$ as described in Section 4.2.1 is often interpreted as the signature of an escaping neutrino. This is not valid in all cases, since there are several other possible causes, for instance, imprecise momentum measurement or particles escaping outside the acceptance region of the detector. The calorimeter system of ATLAS was designed to minimize these influences, covering the whole azimuthal angle around the beam axis. Precise energy measurement is provided in a pseudorapidity region of $|\eta| < 4.9$ using different techniques. The calorimeter system also provides significant information for the identification of particles. A cut-away view can be seen in Figure 4.3b.

The innermost part of the calorimeter system is the liquid argon (LAr) based *Electromagnetic Calorimeter*. It covers a pseudorapidity region of $|\eta| < 1.475$ in the barrel region. The accordion geometry was used for its full ϕ coverage and high rotational symmetry in acceptance. Two coaxial wheels extend the acceptance to the end-cap region of $1.375 < |\eta| < 3.2$. The region with the highest accuracy dedicated to precision physics is $|\eta| < 2.5$. All electromagnetically interacting particles deposit all their energy in this calorimeter in the ideal case. This is not the case for heavy particles due to suppression of bremsstrahlung.

In the barrel region the Electromagnetic Calorimeter is surrounded by the *Hadronic Tile Calorimeter* which uses scintillating tiles as active material. The Hadronic Tile Calorimeter covers a region of $|\eta| < 1.7$ which is expanded by the LAr based *Hadronic End-cap Calorimeter*. This calorimeter is situated behind the end-cap Electromagnetic Calorimeter and provides energy measurements in a region of $1.5 < |\eta| < 3.2$.

To extend the acceptance region to even higher pseudorapidities the LAr-based *Forward Calorimeter (FCal)* was built. It consists of three additional segments per beam direction. The innermost segment is an electromagnetic calorimeter using copper as active medium, while the other two measure hadronic interactions using tungsten as active medium. The FCal covers pseudorapidities of $3.1 < |\eta| < 4.9$.

4.2.4 Muon System

Muons have a mass of 105.6 MeV, resulting in a strong suppression of bremsstrahlung compared to electrons. Combined with a long lifetime of $2.2\,\mu$s[1], these properties prevent effective measurement in the calorimeter system. The *Muon System* was designed especially for the measurement of muons. Since typically no other particle[2] escapes the calorimeter system the Muon System provides a clean signature leading to excellent reconstruction and identification rates close to 100 %. For the momentum measurement a region of $|\eta| < 2.7$ is covered, while information for triggering are available for $|\eta| < 2.4$. The Muon System is the outermost part of the ATLAS detector, filling in most of the total volume. A cut-away view can be seen in Figure 4.3c.

In the barrel region the *Monitored Drift Tubes* measure the tracks of muons and *Resistive Plate Chambers* provide trigger information. In high-η regions the *Cathode Strip Chambers* are used for tracking and *Thin Gap Chambers* for triggering. In order to bend the tracks of muons there is a toroidal magnetic field of 0.5 T in the barrel region and 1 T in the high-η region. For an accurate measurement the current field must be precisely known. Hundreds of sensors to monitor the fields enable a momentum accuracy of 10 % for transverse momenta of the muon up to $p_{\mathrm{T}} \approx 1$ TeV.

4.2.5 Trigger System

Saving information of every event ($\approx \mathcal{O}(1\,\mathrm{MB})$) at the collision rate at design luminosity of $\mathscr{L} = 40\,\mathrm{MHz}$ would result in an infeasible output-rate of several TB per second. Output and storage of this amount of data cannot be implemented due to technical

[1] In this case long means sufficient to allow muons with typical energies to escape the detector without decaying.

[2] The exception of this being the neutrino which escapes also the Muon System.

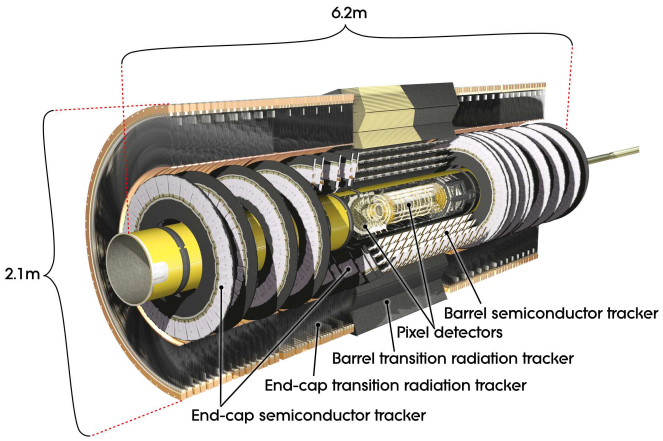

(a) Inner Detector

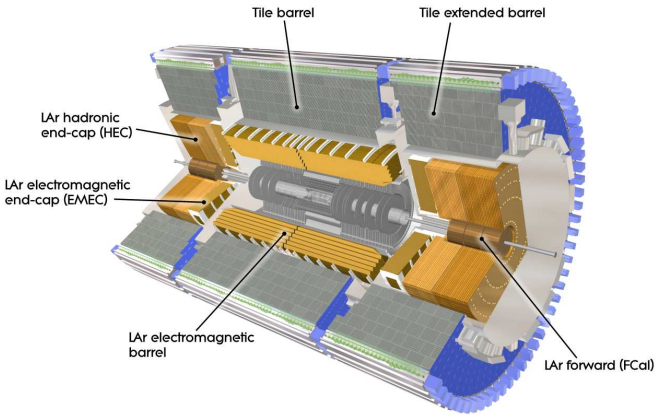

(b) Calorimeters

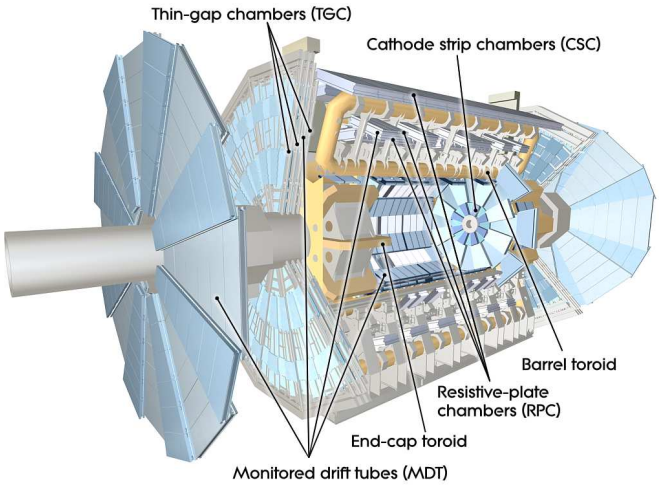

(c) Muon System

Figure 4.3: Cut-away views of different parts of the ATLAS detector [38].

and financial constraints. These constraints limit the recording rate to approximately 200 Hz. It is therefore necessary to reduce the output stream by an order of 10^5.

The *Trigger and Data Acquisition System (TDAS)* was designed to store only the most interesting events while meeting these financial constraints. It is a highly configurable system with multiple levels. Each of these levels imposes additional constrains on each event passing previous levels by utilizing increasingly complex event data. Inbetween the levels a buffering system is used to reduce the effective dead-time. Only the events passing all levels are stored and available for offline analyses.

The hardware-based *level-one trigger (L1)* evaluates the output over the full detector area. Trigger decisions are made using only information of the calorimeter and the MS at a reduced granularity. *Regions of interest* (RoI) are defined containing η and ϕ information of objects to be evaluated. L1 limits the maximum output rate of 75 kHz.

The *second level trigger (L2)* and *Event Filter (EF)* are software based and can be adjusted easily. L2 considers the full granularity in the RoI and more advanced algorithms to refine the decision of L1. The maximum output rate of L2 is 3.5 kHz. The EF uses full offline analysis algorithms and object reconstructions for its decisions. Current calibrations and magnetic field strengths are also available. Its decision completes the trigger chain and every event passing the EF is stored and distributed for later offline analyses. The final output is reduced to an event rate of 200 Hz which corresponds to an output of data of 300 MB per second.

Chapter 5

Data Processing

To test theories it is necessary to compare their predictions to experimental measurements. Theories whose predictions contradict measurements are ruled out. Since there may be other theories able to explain measurements a theory can never be proven to be true though. In order to test the SM and other theories in particle physics, events have to be simulated. Total cross sections and kinematic distributions of these simulated events are then assumed to be compatible with measurements, assuming the theory is valid. The following chapter summarizes the process of obtaining simulated events from theory.

5.1 Simulation of events

At first the events of the hard scattering are simulated. These correspond to a set of Feynman diagrams connecting an initial state with a given final state at matrix element level. Event generators calculate all allowed Feynman diagrams of a given order of pertubation theory, evaluate the phase space integral numerically and afterwards simulate events. The kinematics of the final state particles are chosen according to the probability functions obtained in the integration process. This level of simulation is often called *parton level* as all partons are allowed to be included regardless of their observability.

As the total phase space can easily have more than ten, for instance for the events simulated for this thesis up to 16[1] , dimensions Monte Carlo methods have to be used to evaluate the phase space integral. Thus, these programs are called Monte Carlo generators. In order to reduce calculation time it is possible to restrict the phase space, reducing the range of the phase space integral.

For hadronic beams, *parton density functions (PDFs)* are introduced to parametrize the probability for a given constituent to have a given fraction of the total momentum of the momentum. The PDFs cannot be calculated using available computing facilities and are obtained from fits to measurements.

To obtain physical final states, the next step of event simulation, called *parton shower*, is applied. Outgoing particles of the previous step are read in and several effects are simulated. Unstable particles decay and in addition to initial and final state radiation, also pertubative effects are taken into account. Subsequently, resulting partons are grouped to stable hadrons during hadronization. The level of simulation of events which have passed this step, is called on *particle level* since only stable particles are included.

In this step, no simulation of detector effects has taken place. Detector effects have to be considered, though, for a comparison with measured data. Several effects such

[1] Calculated for a process with 2 incoming and 6 outgoing particles. Each particle is assumed to be on-shell, the transverse momenta of the incoming particles are neglected, and energy and momentum conservation is applied. This leads to one dimension per incoming, three dimensions per outgoing particle, minus 4 for the conservation laws.

as multi-parton interactions, underlying event, or pile-up have to be simulated for a good modeling of the full collision. Subsequently, the response of the detector including digitization is modeled considering detector geometry and material properties. From this point on the same algorithms are used for measured and simulated data. These algorithms aim to reconstruct particles using their signatures in the detector and to distinguish between simultaneous interactions.

5.2 Narrow-width approximation

To reduce computing time it is possible to apply approximations. In the *narrow-width approximation* an intermediate resonance is required to be produced at its pole [48]. Thus, for the calculation of the matrix element the propagator can be replaced using

$$\frac{1}{q^2 - M^2 + iM\Gamma} = \delta(q^2 - M^2)\frac{\pi}{M\Gamma}\,. \tag{5.1}$$

This approximation is only valid for $\Gamma < M$ hence the nomenclature. Equation (5.1) implies that the matrix element can be factorized into the single matrix elements for the production and the decay of the intermediate resonance. This simplifies the necessary calculations, therewith reducing the computing time for the calculation of the matrix element. This approximation also effects the treatment of helicities of the intermediate particle during the calculation of the matrix element. In the full propagator one has to sum over all helicity combinations. Consequently, a separation of different helicity states of the intermediate resonance is not possible. However, in the narrow-width approximation in each matrix element the intermediate resonance has a defined helicity state. Thus, if the interferences between the helicity states are small a separation is a valid approximation.

Full spin correlations can be considered using the Collins-Richardson algorithm [49]. In summary the matrix element of the full process using the narrow-width approximation $\mathcal{M}_{\mathrm{NWA}}$ is given by the sum of the products of the production $\mathcal{M}_{\mathrm{P}}$ and decay $\mathcal{M}_{\mathrm{D}}$ subprocesses for all helicity states. $|\mathcal{M}_{\mathrm{NWA}}|^2$ can be written as follows

$$|\mathcal{M}_{\mathrm{NWA}}|^2 = \mathcal{M}_{\mathrm{P}}^{\kappa}\left(\mathcal{M}_{\mathrm{P}}^{\kappa}\right)^* \rho^{\lambda\lambda'} \mathcal{M}_{\mathrm{D}}^{\lambda}\left(\mathcal{M}_{\mathrm{D}}^{\lambda'}\right)^*\,, \tag{5.2}$$

using the spin density matrix of the intermediate states $\rho^{\lambda\lambda'}$. This matrix incorporates the full spin correlations according to the description in Subsection 2.2.2. By passing only the spin matrix from the production process to the decay the full spin correlations are considered while splitting the matrix element into subprocesses.

5.3 Monte Carlo generators

Several Monte Carlo generators are available to simulate $VVjj$ processes at leading order (LO). For this study, Whizard and MadGraph5_aMC@NLO have been used as they are able to write out helicity information for final state particles. This will be discussed in Section 5.4. Beforehand both programs are introduced briefly.

5.3.1 Whizard

Whizard [50,51] is a universal Monte Carlo event generator covering the whole process from calculation of matrix elements of LO Feynman diagrams to simulating and writing out parton or particle level events. Matrix elements are calculated dynamically using O'Mega allowing for usage in a broad range of physics processes. Several models are implemented, but only the SM was used in this thesis. While not written out by default, helicity event output to `hepmc` [52] can be switched on by hand for each final state particle. The angle between the spin and momentum of a particle is then explicitly written out.

WHIZARD is steered using a special-purpose language called SINDARIN. Its syntax was designed to meet the needs in event analyses. In contrast to other approaches this enables WHIZARD to use very sophisticated phase space definitions while steering scripts can remain short and clean in basic processes. Fundamental analyses and studies can be performed using SINDARIN on the output events. The final events can be processed using a parton shower in WHIZARD or via interfaces to external tools.

In addition to the calculation of the full set of allowed matrix elements, user-defined chains of decays can be applied. Using these decay chains, complex processes can be split into subprocesses allowing for faster integration and generation. Only the Feynman diagrams containing the chosen intermediate particles as s channel resonances are considered. In this case the full matrix element is calculated but only for a subset of all possible diagrams. This approximation is only valid for $\Gamma < M$ of the intermediate resonances.

In addition the narrow-width approximation is implemented in WHIZARD using the Collins-Richardson algorithm (see [53] for details of the implementation). WHIZARD also includes the possibility to use approximations of the introduced spin density matrix. This enables WHIZARD to use only a diagonal spin density matrix, neglecting interference effects or to neglect all spin correlations. However, a bug was found in the implementation of this approximation of the spin density matrix in version 2.2.3 used throughout this thesis. In version 2.2.4 this was corrected, but samples were not available in the time-frame of this thesis. Since this approximation of the spin density matrix was not used for any dataset simulated for this thesis, the used datasets are not effected by this bug.

5.3.2 MADGRAPH5_AMC@NLO

MADGRAPH5_AMC@NLO [54] (MG5_AMC) is a Monte Carlo event generator able to perform next-to-leading (NLO) order calculations. It is a universal generator like WHIZARD calculating the matrix element on-the-run and was developed as a combination of MADGRAPH5 and MC@NLO. Interfaces to several external programs are available to perform parton showering and the simulation of detector effects. In contrast to WHIZARD MADGRAPH5_AMC@NLO is steered using runcards. Also a pre-defined set of cuts is allowed and read-in from these runcards. Thus, abilities for sophisticated phase space cuts or direct analyses are rather limited.

Throughout this thesis, version 5.2.2.2 was used. In order to reduce computing time samples generated for this thesis are simulated at LO. This was necessary as the time for the calculation of matrix elements increased from several seconds or minutes at LO to several hours at NLO for the full VBS process.

By default the output file in the `lhef` [55] format also contains the helicity information of initial and final state particles. This is possible as different helicity combinations are treated as different diagrams and are thus calculated independently. All diagrams are written out after the calculation of all possible diagrams before the event generation is started. These files can be modified such that only a given helicity combination is generated (see [56]). The final sample contains then only the specified helicity combination.

Similar to WHIZARD, MADGRAPH5_AMC@NLO is able to separate the production and decay of particles while spin correlations are taken into account. In MADGRAPH5_AMC@NLO this is done via the program MADSPIN [57]. It simulates specified decays of final state particles contained in the output files written by MADGRAPH5_AMC@NLO. The used algorithm [58] ensures implementation of the full spin correlations and recovers off-shell effects. In the first step the undecayed matrix element $\mathcal{M}_{\text{undecayed}}$ is calculated using the information given in the header of the `lhef` file written by MADGRAPH5_AMC@NLO. $\mathcal{M}_{\text{undecayed}}$ multiplied by a known function is an upper bound for the full matrix element $\mathcal{M}_{\text{full}}$ including decay. This is used to reweight $\mathcal{M}_{\text{undecayed}}$ to $\mathcal{M}_{\text{full}}$ on an event-by-event basis. For each particle to be decayed a set of momenta for the decay products is chosen randomly and both matrix elements $\mathcal{M}_{\text{undecayed}}$ and $\mathcal{M}_{\text{full}}$ are evaluated at this phase space point. If a uniformly

distributed random number $r \in [0, 1]$ fulfills

$$r < \frac{\mathcal{M}_{\text{full}}}{\mathcal{M}_{\text{undecayed}}} \tag{5.3}$$

the momenta of the decay products are accepted. If it is larger than this fraction the set of random momenta for the decay products are rejected. New momenta are randomly chosen until an accepted pair of momenta is found. Thus, the matrix element of the subprocess is reweighted to the matrix element of the full process and the decay spin correlations are taken into account. Additionally, the δ peak for the on-shell resonance mass is reweighted to the full Breit-Wigner-Peak again.

5.4 Methodology for simulation of events with known boson polarization

For a study of boson polarization in VBS simulated events of known helicity of the bosons are necessary. Although the helicity of an intermediate particle is of interest this is not defined considering the full process[2]. In this section different approaches to obtain events with known polarization of the intermediate bosons using different approximations are presented.

5.4.1 Reweighting method

In former analyses [31, 59] such datasets are simulated using a reweighting approach. In order to obtain a sample of pure polarization the distribution of θ^*_V of a sample containing all helicity combinations is reweighted to the known analytical functions of pure polarization. As these analytical functions are distorted by phase space cuts it is necessary to apply the reweighting procedure in a phase space as inclusive as possible. The fitted helicity fractions are predicted by theory to depend on the rapidity and the transverse momentum of the boson V (see Eq. (2.41)). In order to take this into account the reweighting is usually done in bins of $y(V)$ and $p_{\text{T}}(V)$. This introduces unphysical steps at the boundaries of the bins in the corresponding differential distributions. These steps can only be smoothed by increasing the number of bins. This is limited by the available statistics of the input dataset. It is also intrinsically not possible to find other dependencies of the helicity fractions using this method.

For this thesis, the reweighting method was implemented using Rivet [60]. In the first step an analysis reads in the sample storing $y(V)$, $p_{\text{T}}(V)$ and θ^*_V information, which are calculated using the true momenta of the charged leptons and neutrinos, for W^+, W^- and Z in a three-dimensional histogram. Having read-in the whole sample the helicity fractions $f_i(V)$ with $i \in \{-1, 0, 1\}$ are fitted in each $p_{\text{T}}(V)$ and $y(V)$ bin according to the theoretical predictions from Equations (2.39) and (2.40). The transverse momentum of the boson was binned in $[0, 30\text{ GeV})$, $[30\text{ GeV}, 60\text{ GeV})$, $[60\text{ GeV}, 90\text{ GeV})$ and $[90\text{ GeV}, \infty)$ for all bosons and the absolute value of the rapidity in $[0, 1)$, $[1, 2)$, $[2, 3)$ and $[3, \infty)$. $\cos\theta^*_V$ was binned in 20 equidistant bins from minus one to one. In this way, all bins contained a sufficient number of events for the fit with reasonable uncertainties. The resulting helicity fractions for each bin are stored for later usage.

In the second step another Rivet analysis reads in the same sample again. This time the weight of each event is multiplied with the reweighting factor

$$\frac{\frac{1}{\sigma}\frac{\mathrm{d}\sigma}{\mathrm{d}\cos\theta^*_W}\Big|_{-1,0,+1}}{\frac{3}{8}\left(1 \mp \cos\theta^*_W\right)^2 f_{-1} + \frac{3}{8}\left(1 \pm \cos\theta^*_W\right)^2 f_{+1} + \frac{3}{4}\sin^2\theta^*_W f_0} \tag{5.4}$$

where

$$\frac{1}{\sigma}\frac{\mathrm{d}\sigma}{\mathrm{d}\cos\theta^*_W}\Big|_{-1,0,+1} = \begin{cases} \frac{3}{8}\left(1 \mp \cos\theta^*_W\right)^2 f_{-1} & \text{for } h = -1 \\ \frac{3}{4}\sin^2\theta^*_W f_0 & \text{for } h = 0 \\ \frac{3}{8}\left(1 \pm \cos\theta^*_W\right)^2 f_{+1} & \text{for } h = +1\,. \end{cases} \tag{5.5}$$

[2] Since one has to sum over the separate helicity states in the propagator.

In both equations the upper sign corresponds to W^+ and the lower to W^-. The corresponding equation for the Z boson can be deduced from Equation (2.40). Depending on the choice of h in Equation (5.5) the helicity of the corresponding boson can be changed. The helicity fractions are used from the previous fit results in the bin corresponding to the kinematics of the reconstructed boson. All helicity combinations are obtained from one sample using different choices for h to calculate the reweighting factor. The choice for the reweighting factor also ensures that the sum of the combinations follows again the original distribution.

As this procedure can be applied to both reconstructed bosons simultaneously arbitrary helicity combinations can be obtained in each run. In principle this is applicable on events simulated using also non-resonant diagrams. For these diagrams the reconstructed bosons from the lepton pair have not been present in the original sample. The used input samples were simulated including only resonant diagrams in order to avoid difficulties in the interpretation of the results. The intermediate bosons are also required to be on-shell. This restrictions correspond to the narrow-width approximation. The different helicity states are separable of each other in the narrow-width approximation if interferences are neglected. The input sample includes this interference effects. In this approach the effects caused by interferences are distributed to the output samples according to the corresponding weights. If the effects of these interferences are large, the fits to the $\cos\theta_V^*$ distributions are not expected to reproduce the distributions. However, if the fit is in good agreement with the observed distribution, these effects are small.

5.4.2 MadGraph5_aMC@NLO and MadSpin

The shortcoming of the reweighting procedure is its inability to describe dependencies of the helicity fraction on other variables. This is of special interest if selection criteria are applied. Consequently, other variables cannot be guaranteed to be modeled correctly.

To overcome this deficit another approach for the generation of samples of pure helicity can be used. As mentioned above MC generators write out the helicity only for final state particles. Thus, samples can be generated such that the bosons are in the final state to have defined helicities. In order to obtain samples with the final state of interest the bosons have to be decayed afterwards. This approach effectively employs the narrow-width approximation.

As explained in Subsection 5.3.2 MadGraph5_aMC@NLO can be modified to generate samples containing only user-defined helicity combinations. Combined with programs able to parse these helicity information and simulate the boson decay according to it, it would be possible to simulate events without the shortcomings of the reweighting method.

The decay of particles can for instance be simulated using Pythia [61]. Only isotropic decays of bosons are implemented in Pythia though. In [62] a private version of Pythia 6 was used containing the known angular distributions for the $W^\pm$ boson. This will bot be studied any further in this thesis due to technical issues.

However, as the used approach is more sophisticated compared to the reweighting method other programs for the simulation of the decay are studied. In Subsection 5.3.2 the tool MadSpin was introduced for this aim. MadSpin simulates for instance boson decays while taking the spin effects and its correlations into account. Samples were generated using this method for this thesis for all different helicity combinations of the bosons. The differential distributions for these are shown in Figure 5.1. As it can be seen the distributions are not consistent with the expectations from theory. This can be understood considering the behavior of the used tools. The modification of the intermediate output of MadGraph5_aMC@NLO allows only to delete certain diagrams from the matrix elements.

This modification is not directly reflected in the output sample. When MadSpin parses the sample it reconstructs the process definition using the header file. MadSpin is not influenced by the modifications described above and all samples with different helicity combinations are reweighted to the same full matrix element. The distinc-

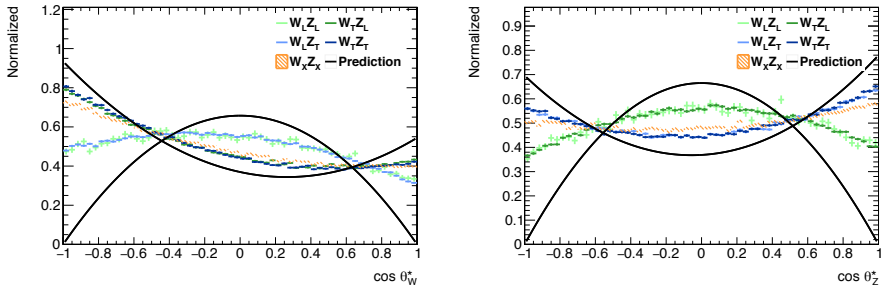

Figure 5.1: Comparison of helicity templates generated using MadSpin. Normalized distribution of the cosine of the decay angle of W $\cos\theta^*_W$ (left) and Z $\cos\theta^*_Z$ (right) in the total phase space. In addition to the templates with given helicity (blue and green), the distribution of a mixed sample (orange) and the theoretical predictions (black) are shown. The theoretical prediction for transverse polarization is a mixture of left- and right-handed helicity. The fractions of this mixture are obtained by fitting to the $W_\mathrm{T}Z_\mathrm{T}$ template.

tions between the samples are expected to arise mainly from the different phase space regions favored by each helicity. For instance the jet kinematics are not changed by MadSpin, while they are correlated with the helicity fractions. The authors of MadGraph5_aMC@NLO also advised against usage of these combinations as this has not been tested yet [63].

5.4.3 WZdecay

Since neither the official version of Pythia nor MadSpin are suited for a full analysis of the helicity fractions the tool WZdecay [64, 65] was developed in the course of this thesis. This tool was required to read samples with bosons of known helicity in the final state and simulate the decay according to the angular distributions. A visualization of the workflow of WZdecay is shown in Figure 5.2. As MadGraph5_aMC@NLO and Whizard are able to generate samples of known helicity in different file formats the tool is able to read both file formats to gain independence from a specific MC generator. The input samples are parsed and the decay of every final state boson is simulated. For these decays random angles are generated according to their predicted distributions using a hit-and-miss procedure. Momenta of the leptons originating in the decay are constructed using the generated mass of the boson and the aforementioned angles in the rest frame of the boson. The z-axis is chosen to correspond to the direction of the boson momentum in the laboratory frame as this is the frame in which the helicities of the bosons are defined. Having boosted these momenta into the laboratory frame, the leptons are added to the event and the bosons are marked as decayed. The decay channels of the bosons can be chosen and the cross section is adjusted according to the branching ratios. The values for the branching ratios are set to the values calculated by Whizard, given by

$$BR(W^\pm \to \ell^\pm + \nu_\ell) = 0.0344\,, \qquad BR(Z \to \ell^+ + \ell^-) = 0.111\,. \tag{5.6}$$

Subsequently, the final events are divided in different samples according to the boson's helicity. Thereby, separate samples for each combination of boson helicities are available. The final cross section of the output samples is determined using the sample's fraction of the total event weights. Samples can be written in the `hepmc` or the `lhef` format. This allows for subsequent showering using Pythia or direct analyses on parton level using Rivet.

Using this procedure it is not necessary to apply any cuts on the leptons. It also allows to produce samples with different generators for validation. However, some approximations are necessary for this procedure. As the input file has to contain the

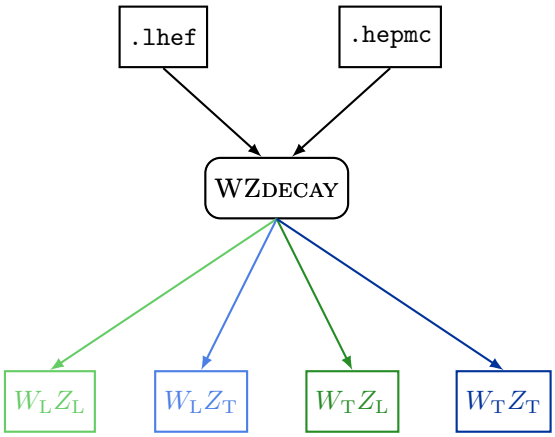

Figure 5.2: Visualization of the workflow of WZDECAY. It is able to read in and parse `lhef` or `hepmc` files, simulates the decay of every W and Z bosons in the final state and writes samples according to the found helicity combination.

bosons as final state particles only the resonant channels are considered as explained above. Furthermore, the bosons have to be on-shell. This corresponds to the narrow-width approximation. This approximation is a precondition for a valid interpretation of helicity fractions of intermediate particles. Consequently, its validity has to be tested for a study of the helicity fractions in a given phase space.

To take the full spin correlations into account the full spin density matrix can be used (see Subsection 5.3.1). However, no file format available supports storing the full density matrix but only the helicity eigenvalue for each particle. The rates for each helicity correspond to the different diagonal elements of the spin density matrix. Consequently, an additional approximation of a diagonal spin density matrix is dictated by these format limitations. Correlations between the helicity states are therefore not modeled.

5.5 Settings and simulated samples

For comparison and validation purposes several samples were generated using different combinations of generators and methods to obtain purely polarized samples. In order to avoid ambiguities reconstructing the W and Z bosons from the final state leptons the parton level final state was restricted to $e^+\nu_e\mu^+\mu^-jj$. In this way a unambiguous assignment of the leptons to the bosons is possible.

Note that the final state is also restricted to the W^+Zjj process to save computation time. For a full study and a measurement also samples of the W^-Zjj process have to be generated as the polarization fractions are expected to differ for the different charges of the W boson. Differences arise from the substructure of the proton. However, the main focus of this study is the validation of different methods to obtain purely polarized samples. This can safely be assumed to be independent of the W boson's charge.

To reduce the contribution of tZj diagrams to the signal process bottom quarks are not allowed in the final state as it was done in previous studies of vector boson scattering in the WZ channel [32]. A list of all used samples can be found in Table 5.1. The necessary parameters for the generation of the samples can be found in Table 5.2.

The resulting samples were analyzed using RIVET. An analysis was implemented able to obtain distributions of several observables in different phase spaces. The full list of selection criteria are listed for all used phase spaces can be found in Tables 5.3 and 5.4.

Table 5.1: List of all datasets generated for this thesis. Samples in the upper part are generated using MadGraph5_aMC@NLO, in lower part using Whizard. If the decay of the bosons is simulated using an external tool this is specified in the third column. For each sample the helicity combination, the number of events N_{events}, the cross section σ, and the process definition in the syntax of the used MC generator are listed. The different helicities are divided either in WZdecay or in MadGraph5_aMC@NLO using the modification described in Subsection 5.3.2. Note the reduced number of events for the purely longitudinal final state in MadGraph5_aMC@NLO (sample ID 5). This indicates a poor phase space integration e. g. caused by divergences. This was not studied further since statements concerning this approach can also be deduced using only samples 6 to 8.

ID	MC generator production	MC generator decay	helicity combination	N_{events}	σ in fb	process definition	comment
1	MG5_aMC		mixed	500000	0.8405	`p p > e+ ve mu+ mu- j j`	full process
2	MG5_aMC		mixed	500000	0.7300	`p p > W+ Z j j, W+ > e+ ve, Z > mu+ mu-`	restricted decay, off-shell effects included
3	MG5_aMC	MadSpin	mixed	500000	0.8376	`p p > W+ Z j j`	`bw_cutoff=1`
4	MG5_aMC	MadSpin	mixed	500000	0.8376	`p p > W+ Z j j`	`bw_cutoff=15`
5	MG5_aMC	MadSpin	$W_{\text{L}}Z_{\text{L}}$	58595	0.4332	`p p > W+ Z j j`	split via modification
6	MG5_aMC	MadSpin	$W_{\text{L}}Z_{\text{T}}$	500000	0.6289	`p p > W+ Z j j`	split via modification
7	MG5_aMC	MadSpin	$W_{\text{T}}Z_{\text{L}}$	500000	0.7298	`p p > W+ Z j j`	split via modification
8	MG5_aMC	MadSpin	$W_{\text{T}}Z_{\text{T}}$	500000	1.0977	`p p > W+ Z j j`	split via modification
9	MG5_aMC	WZdecay	$W_{\text{L}}Z_{\text{L}}$	28883	0.0483	`p p > W+ Z j j`	split in WZdecay
10	MG5_aMC	WZdecay	$W_{\text{L}}Z_{\text{T}}$	83392	0.1394	`p p > W+ Z j j`	split in WZdecay
11	MG5_aMC	WZdecay	$W_{\text{T}}Z_{\text{L}}$	96317	0.1610	`p p > W+ Z j j`	split in WZdecay
12	MG5_aMC	WZdecay	$W_{\text{T}}Z_{\text{T}}$	291408	0.4872	`p p > W+ Z j j`	split in WZdecay
13	Whizard		mixed	500000	1.3477	`qf, qf => j, j, Wp, Z; unstable Wp; unstable Z`	narrow-width approximation
14	Whizard		mixed	500000	1.6735	`qf, qf => j, j, E1, n1, e2, E2 {$restrictions="5+6~'W+'&&7+8~Z"}`	restricted decay, off-shell effects included
15	Whizard	WZdecay	$W_{\text{L}}Z_{\text{L}}$	32156	0.0845	`qf, qf => j, j, Wp, Z; polarized Wp; polarized Z`	split via WZdecay
16	Whizard	WZdecay	$W_{\text{L}}Z_{\text{T}}$	87105	0.2289	`qf, qf => j, j, Wp, Z; polarized Wp; polarized Z`	split via WZdecay
17	Whizard	WZdecay	$W_{\text{T}}Z_{\text{L}}$	101067	0.2656	`qf, qf => j, j, Wp, Z; polarized Wp; polarized Z`	split via WZdecay
18	Whizard	WZdecay	$W_{\text{T}}Z_{\text{T}}$	279672	0.7349	`qf, qf => j, j, Wp, Z; polarized Wp; polarized Z`	split via WZdecay

Table 5.2: List of parameters necessary for the event simulation and its values which are used in the simulation of events using the WHIZARD and MADGRAPH5_aMC@NLO Monte Carlo generators accordingly, including masses and widths of particles.

Parameter	Value	
	Whizard samples	MG5_aMC samples
center-of-mass energy $\sqrt{s}$	13 TeV	13 TeV
renormalization scale μ_r	200 GeV	200 GeV
factorization scale μ_f	200 GeV	200 GeV
parton distribution function	`CT10`	`CT10`
Fermi constant G_F	$1.1663787 \cdot 10^{-5}$ GeV^{-2}	$1.16639 \cdot 10^{-5}$ GeV^{-2}
electroweak coupling α_{EW}	132.3479^{-1}	132.5070^{-1}
strong coupling α_s	0	0
M_W	80.399 GeV	80.419 GeV
Γ_W	2.085 GeV	2.0476 GeV
M_Z	91.1876 GeV	91.188 GeV
Γ_Z	2.4952 GeV	2.441404 GeV
m_H	126 GeV	125 GeV
Γ_H	0.00418 GeV	0.006382339 GeV
m_{top}	172.5 GeV	173 GeV
m_b	0 GeV	4.7 GeV
m_s	0 GeV	0 GeV
m_c	0 GeV	0 GeV
m_τ	1.77705 GeV	1.77700 GeV
m_μ	0 GeV	0 GeV
m_e	0 GeV	0 GeV

Table 5.3: Selection criteria for all studied phase space regions implemented in RIVET and the phase space used for the integration in the Monte Carlo simulator for an object to be accepted as Z-lepton ℓ^Z, W-lepton ℓ^W, or jet j. Only objects fulfilling this criteria are accepted. The criteria which are marked with $*$ are only applied on two of the leptons, i. e. only two of the three charged leptons are required to have a transverse momentum larger than 5 GeV for the integration in WHIZARD.

Object	Variable	Generator cuts		RIVET selection			
		WHIZARD	MG5_aMC	total	detector	WZ	VBS
ℓ^Z	$p_{\text{T}\min}$ in GeV	5*	10	0	7.0	15.0	15.0
	$\lvert\eta\rvert_{\max}$	5	5	∞	2.5	2.5	2.5
ℓ^W	$p_{\text{T}\min}$ in GeV	5*	10	0	7.0	20.0	20.0
	$\lvert\eta\rvert_{\max}$	5	5	∞	2.5	2.5	2.5
jets	$p_{\text{T}\min}$ in GeV	15	15	0	5.0	5.0	30.0
	$\lvert\eta\rvert_{\max}$	5	5	∞	2.5	2.5	2.5

Table 5.4: Selection criteria for all studied phase space regions implemented in RIVET and the phase space used for the integration in the Monte Carlo simulator. If the objects, that pass the criteria listed in Table 5.3 of an event or phase space point fulfill these additional criteria, it is accepted.

Variable		Generator cuts		RIVET selection			
name	unit	WHIZARD	MG5_aMC	total	detector	WZ	VBS
$N_{\text{leptons}_{\text{min}}}$		3	3	3	3	3	3
$N_{\text{jets}_{\text{min}}}$		2	2	0	0	0	2
$m_{\text{T}}(W)_{\text{min}}$	GeV	0	0	0	7.0	30.0	30.0
$\lvert M_{\ell^z \ell^z} - M_Z \rvert_{\text{max}}$	GeV	∞	∞	∞	∞	10	10
$M_{\ell\ell_{\text{min}}}$	GeV	0	0	0	0	0.1	0.1
$M_{jj_{\text{min}}}$	GeV	0	150	0	0	0	500
$\Delta Y_{jj_{\text{min}}}$		0	0	0	0.4	0.4	1.5
$\Delta R_{jj_{\text{min}}}$		0.4	0.3	0	0.4	0.4	0.4
$\Delta R_{j\ell_{\text{min}}}$		0.0	0.0	0	0.1	0.1	0.1
$\Delta R_{\ell\ell_{\text{min}}}$		0.3	0.2	0	0.3	0.3	0.3

Chapter 6

Study of Templates

Three different approaches to obtain samples with intermediate bosons in a well-defined polarization state are introduced in Section 5.4. All of these methods were implemented for this thesis and events were simulated. The methods are compared to each other using the samples of simulated events in the following chapter.

6.1 Closure tests

6.1.1 Fits in reweighting method

For the reweighting method, the $\cos\theta_V^*$ distribution is fitted in bins of the transverse momentum and the rapidity of each boson using a χ^2-fit. In Figure 6.1 the observed number of events for each of these bins can be seen. The fit was executed using the `RooFit` package of the `ROOT` software framework [66]. The fit function was stated in Equation (2.39) and (2.40). The integral over $\cos\theta_W^*$ of these equations is one if the helicity fractions sum up to one. The fit parameters are used for the calculation of the new event weight. There are several constraints on these fit parameters which result from the interpretation of the fit parameters as helicity fractions f_i. Each of them has to be in the interval $[0, 1]$. Additionally, the sum of all helicity fractions has to be one:

$$f_i \in [0, 1]\,, \qquad \sum_{i=-1,0,+1} f_i = 1\,. \tag{6.1}$$

It is not possible to apply all four of these constraints on the fit parameters for technical reasons. Thus, two different fits were performed resulting in two sets of samples with pure polarization.

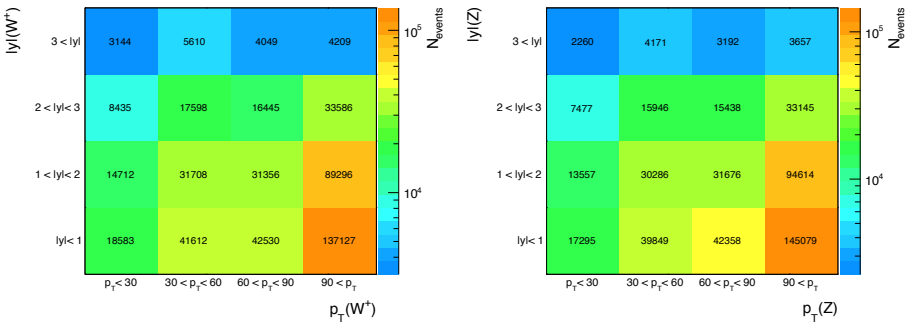

(a) $p_{\mathrm{T}}(W^+) - y(W^+)$-plane **(b)** $p_{\mathrm{T}}(Z) - y(Z)$-plane

Figure 6.1: Distribution of total number of events in the different $p_{\mathrm{T}}(V)$ and $y(V)$ bins used for the fits for the reweighting method is shown in (a) for the W^+ boson and in (b) for the Z boson. The total number of events is 500000.

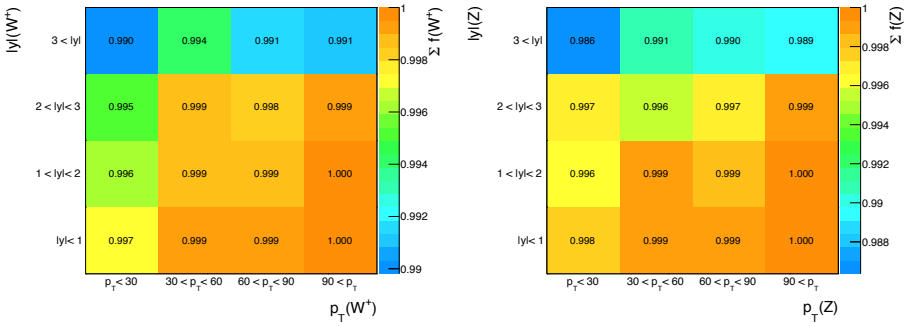

(a) $p_{\mathrm{T}}(W^+) - y(W^+)$-plane **(b)** $p_{\mathrm{T}}(Z) - y(Z)$-plane

Figure 6.2: Sum of the helicity fractions in each bin after the unconstrained fit to the predicted distribution of the $\cos\theta_V^*$ distribution of mixed sample generated with MadGraph5_aMC@NLO is shown in (a) for the W^+ boson and in (b) for the Z boson.

In the first approach, only the allowed intervals are set for each parameter, i. e. $f_i \in [0, 1]$ for $i \in \{-1, 0, 1\}$. This approach will be called unconstrained fit[1] in the following. The three helicity fractions are treated equally in this approach. The sum of the helicity fractions can deviate from one, though. However, if the number of entries in a bin in the transverse momentum and rapidity plane is large enough, these deviations from one are expected to be small provided the observed distribution is compatible with the prediction. Before applying the fit, the functions of the fits are scaled to the integral of the mixed sample such that the integrals of the fit function and the distribution are equal in each bin of the transverse momentum and rapidity of the boson.

The sum of the fitted helicity fractions is plotted in Figure 6.2 in the bins of the transverse momentum and rapidity of both bosons. It can be seen that the deviations of the sum from one are small in all bins. The largest deviations of about 2 % occur for large boson rapidities. These deviations are assumed to be caused by low statistics in these bins. The deviations may be minimized by optimizing the binning in the plane of the transverse momentum and rapidity of the bosons. Nevertheless, these deviations effect only a small number of events. The influence on the reweighted distributions is expected to be negligible. The general level of agreement is sufficient for the production of samples using this reweighting approach.

In order to quantify this influence, another fitting approach was applied in addition to the aforementioned one. In this additional approach the fraction of left-handed helicity f_{-1} is replaced by

$$f_{-1} = 1 - f_0 - f_{+1}\,. \tag{6.2}$$

Thereby the sum of the helicity fractions is fixed to one. As a trade-off the parameter f_{-1} cannot be constrained to the interval $[0, 1]$ anymore for technical reasons. This is called constrained fit from here on. The distributions of the left-handed helicity fraction for this fitting approach can be seen in Figure 6.3. The left-handed helicity fraction is in a physical range for all of the bins for the W^+ boson. For the Z boson, there are two bins with negative helicity fractions. This effect could again be suppressed by optimizing the binning in the plane of the transverse momentum and rapidity of the bosons.

An advantage of the constrained approach is a reduction of the number of free parameters. Consequently, the uncertainties on the fit parameters are smaller compared to the unconstrained approach. This uncertainties can be seen in Figure 6.4, in which the distribution of the right-handed helicity fraction f_{+1} for both fit approaches are compared. The differences in the uncertainties are rather small since the fit parameters are highly correlated.

[1] This name refers to the unconstrained sum of the helicity fractions.

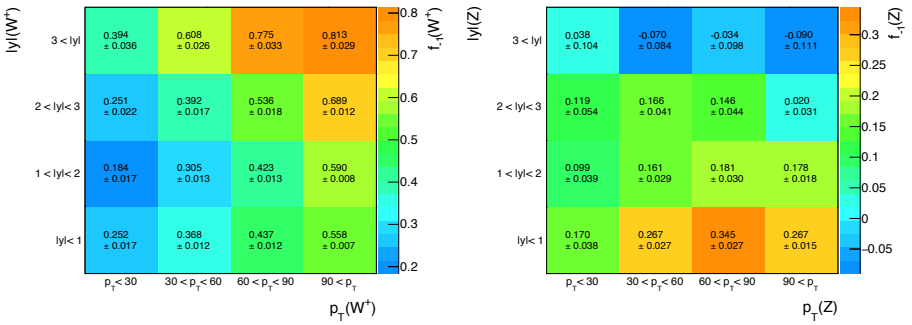

(a) $p_{\mathrm{T}}(W^+) - y(W^+)$-plane **(b)** $p_{\mathrm{T}}(Z) - y(Z)$-plane

Figure 6.3: The Left-handed helicity fraction f_{-1} after the constrained fit to the predicted distribution of the $\cos\theta^*_V$ distribution of a mixed sample generated with MadGraph5_aMC@NLO is shown in (a) for the W^+ boson and in (b) for the Z boson. In this fitting approach the parameter f_{-1} is not constrained to the interval $[0, 1]$.

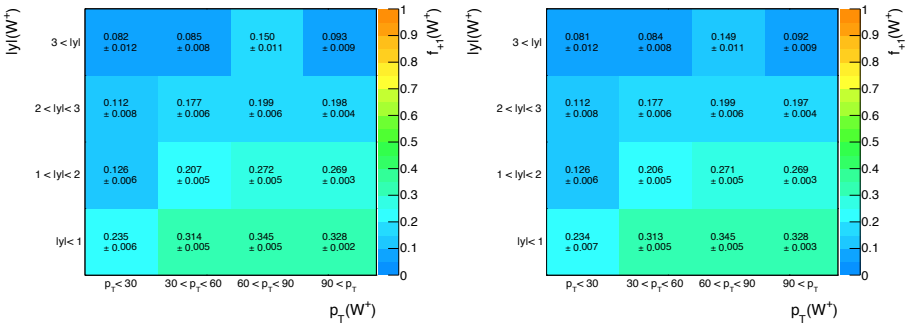

(a) constrained fit **(b)** unconstrained fit

Figure 6.4: Right-handed helicity fraction f_{+1} after the fit to the predicted distribution of the $\cos\theta^*_{W^+}$ distribution of a mixed sample generated with MadGraph5_aMC@NLO is shown in (a) using a constrained and in (b) an unconstrained fit.

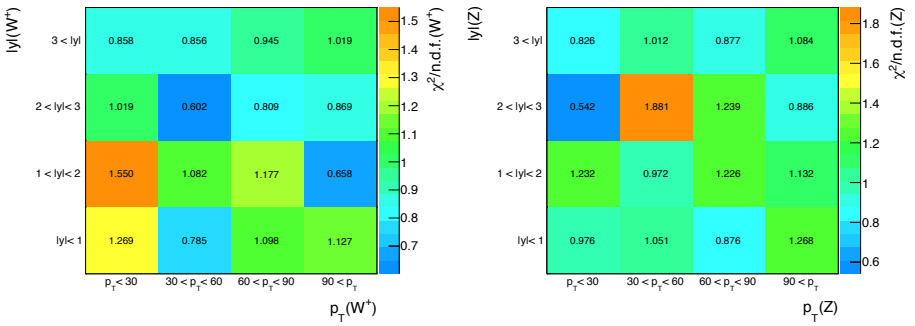

(a) $p_{\mathrm{T}}(W^+) - y(W^+)$-plane **(b)** $p_{\mathrm{T}}(Z) - y(Z)$-plane

Figure 6.5: Ratio χ^2/n.d.f. to quantify the goodness of the fits in bins of $p_{\mathrm{T}}(V)$ and $y(V)$ for the unconstrained fit applied on the mixed sample generated with MadGraph5_aMC@NLO. For each shown bin n.d.f. is 37. The distribution is shown in (a) for the fits of distributions of the W^+ boson and in (b) for the Z boson.

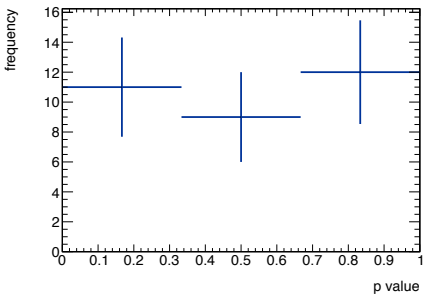

Figure 6.6: Distribution of the p-value for the unconstrained fit to a mixed sample generated using MadGraph5_aMC@NLO. The p-value corresponds to the probability of obtaining a larger χ^2 value for a given number of degrees of freedom assuming a χ^2-distribution.

Comparing these methods the unconstrained fit is favored to avoid negative helicity fractions since these would result in negative event weights. Nevertheless, the resulting reweighted samples are hardly distinguishable between the two fitting approaches since problems in both approaches influence only a small number of events.

As a validation of the fits the ratio of χ^2 over the number of degrees of freedom (n.d.f.) for all fit results are shown in Figure 6.5. The number of degrees of freedom equals the number of bins in the fitted distribution reduced by the number of fit parameters. A ratio close to one indicates a good agreement of the fit. The observed values fluctuate around this value.

The relatively large number of fits of 32 in total allows for an additional test. The χ^2 and the number of degrees of freedom can be used to calculate the p-value. This p-value represents the probability to obtain a larger χ^2 value for the given number of degrees of freedom assuming a χ^2-distribution. This value can also be interpreted as the probability of obtaining a fit result with inferior agreement. The resulting p-values should be uniformly distributed over the interval $[0, 1]$. A histogram of these p-values for the unconstrained fits is shown in Figure 6.6. The resulting p-values are compatible with a uniform distribution.

The full set of distributions and the fitted functions in the plane of the transverse momentum and rapidity of the bosons are shown in Section D.2 in the Appendix.

The full set of helicity fractions using the unconstrained fit can be seen in Figure 6.7. The longitudinal fractions show very similar behavior for both bosons. However, the distribution of the left-handed fraction of the Z boson, $f_{-1}(Z)$, is more similar to the right-handed fraction of the W^+ boson $f_{+1}(W^+)$.

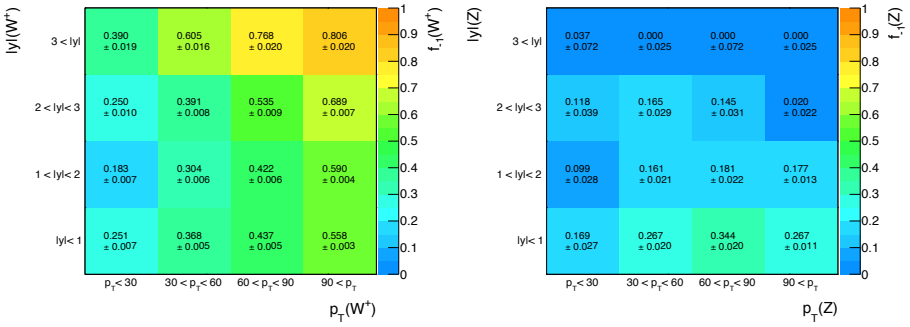

(a) $f_{-1}(W^+)$

(b) $f_{-1}(Z)$

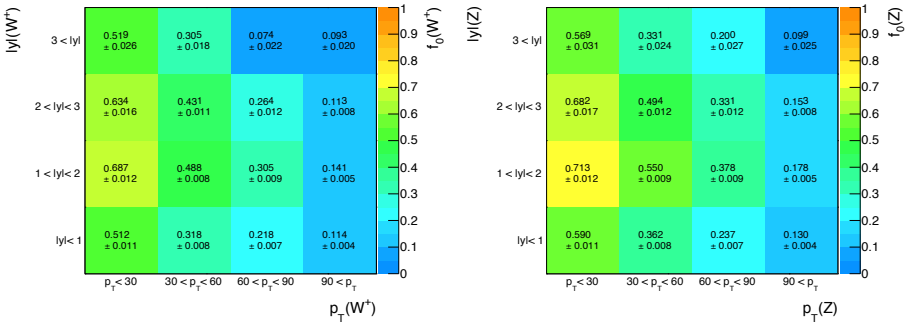

(c) $f_0(W^+)$

(d) $f_0(Z)$

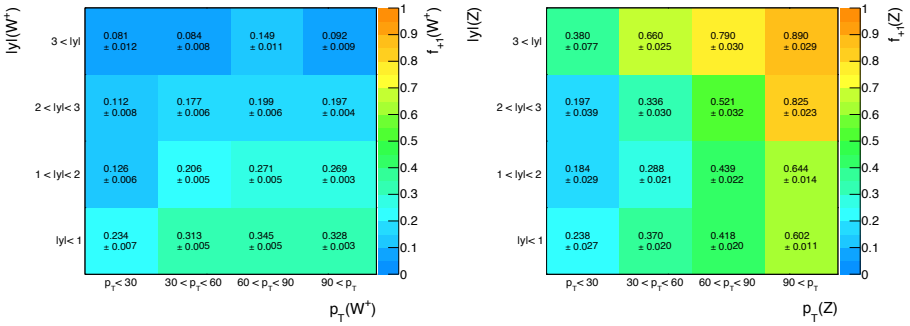

(e) $f_{+1}(W^+)$

(f) $f_{+1}(Z)$

Figure 6.7: Helicity fractions f_i after the unconstrained fit to the predicted distribution of the $\cos\theta^*_V$ distribution of a mixed sample generated with MadGraph5_aMC@NLO are shown in (a), (c), and (e) for the W^+ boson and in (b), (d), and (f) for the Z boson. (a) and (b) show the left-handed helicity fraction f_{-1}, (c), (d) show f_0 and (e) and (f) f_{+1}.

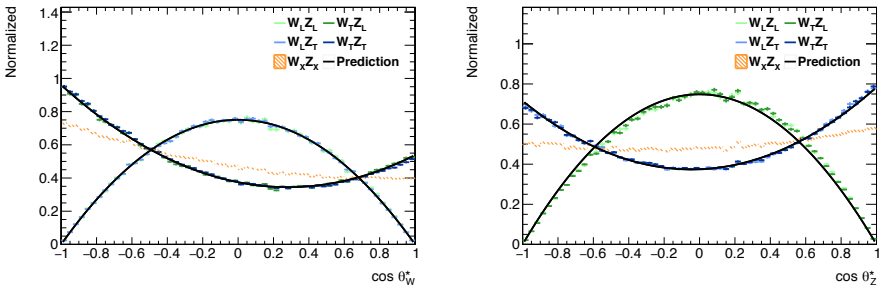

(a) $\cos\theta^*_{W+}$ **(b)** $\cos\theta^*_Z$

Figure 6.8: Comparison of the helicity templates generated reweighting a sample from MadGraph5_aMC@NLO. The normalized distribution of the cosine of decay angle of W $\cos\theta^*_W$ (left) and Z $\cos\theta^*_Z$ (right) in the total phase space are shown. In addition to the templates with given helicity (blue and green), the distribution of a mixed sample (orange) and the theoretical predictions for pure helicity states (black) are shown. The theoretical prediction for transverse polarization is a mixture of left- and right-handed helicity. The fractions of this mixture are obtained by fitting to the $W_\mathrm{T}Z_\mathrm{T}$ template.

In order to understand this feature the introduction of the predicted distributions of the bosons' decay angles has to be considered and transfered from the leptonic decay to the radiation of a boson by a quark. The decay angle peaks at the same values for W^+ and Z bosons of equal helicity. However, the definition of the decay angle differs. For the W^+ boson the decay angle is defined as the angle to the (positively) charged lepton. For the Z boson the angle to the negatively charged lepton is used. Applying this definition on hadronic decays, the angles to quarks resulting from W^+ or Z decays are expected have a maximum at different values for quarks of equal charge. The distributions of a given helicity for Z decays correspond to the opposite W^+ helicity. Applying the same argument on the radiation process rather than the hadronic decay, leads to the observed correspondence of the $f_{-1}(W^+)$ and $f_{+1}(Z)$ distributions.

Consequently, the distribution of the W^- boson's helicity fractions are expected to be similar to the distributions of the helicity of the Z boson.

The distributions are in good agreement with the expectations from Subsection 3.2.2. The longitudinal states were expected to dominate for high rapidities and low transverse momenta. However, for high energies the longitudinal states are suppressed as dictated by the equivalence theorem. The region dominated by longitudinal polarization contains only a small fraction of the total events though. Additionally, the region of low transverse boson momenta is expected to be influenced by the necessary phase space cuts. This is studied in Section 6.3.

As this study aims at an distinction between longitudinal and transverse polarization states, the helicities -1 and +1 are not distinguished from here on. The combination of both states with transverse polarization is studied and compared instead to the longitudinal polarization.

6.1.2 Angular distributions

The generated samples contain bosons of a given polarization. Consequently, they are expected to reproduce the predicted distribution of $\cos\theta^*_V$. The samples which are produced using MadSpin to simulate the decay of polarized bosons, do not show the expected behavior. This can be seen in Figure 5.1. As it is discussed in Section 5.4.2 the discrepancies originate from the reweighting procedure used in MadSpin. The matrix element of each sample is reweighted to the same full matrix element. Thus, these samples are closer to the mixed sample and differences between each other are suppressed.

The corresponding distributions for the samples from the reweighting method can be

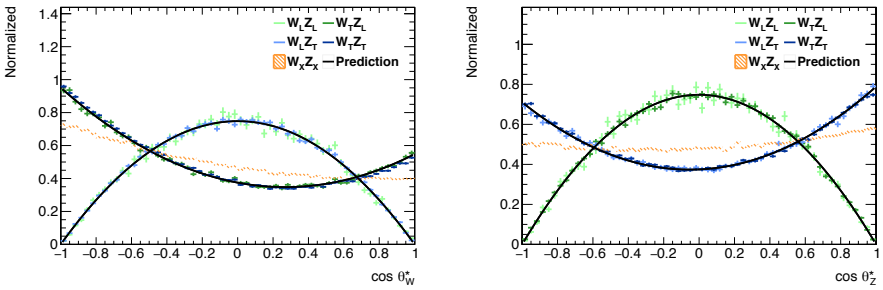

(a) $\cos\theta^*_{W+}$ **(b)** $\cos\theta^*_Z$

Figure 6.9: Comparison of the helicity templates generated using WZDECAY with a MADGRAPH5_aMC@NLO sample as input. The normalized distribution of the cosine of decay angle of W $\cos\theta^*_W$ (left) and Z $\cos\theta^*_Z$ (right) in the total phase space are shown. In addition to the templates with given helicity (blue and green), the distribution of a mixed sample (orange) and the theoretical predictions for pure helicity states (black) are shown. The theoretical prediction for transverse polarization is a mixture of left- and right-handed helicity. The fractions of this mixture are obtained by fitting to the $W_\mathrm{T}Z_\mathrm{T}$ template.

seen in Figure 6.8. The distributions of $\cos\theta^*_W$ are in good agreement with the predicted distributions. For the Z boson's decay angle $\cos\theta^*_Z$ small discrepancies can be observed. There discrepancies are assumed to be caused by the choice for the reweighting factor (see Eq. (5.4)). The denominator is chosen such that only the fit of the predicted distribution to the mixed sample is taken into account. In order to evaluate the correct statistical uncertainty non-trivial correlations between the samples, have to be considered. These correlations are introduced by the correlations of the fit parameters used for the reweighting.

The samples generated using WZDECAY also reproduce the predicted angular distribution. This can be seen in Figure 6.9. No systematic deviations from the predicted distribution can be seen.

Compared to the reweighting method the statistical uncertainty of the distributions especially for the longitudinal polarizations is larger. The numbers of input events are the same for both methods though. For the reweighting method every event is used for all helicity combinations with a reduced weight. In WZDECAY the mixed sample is divided according to the given helicity. Thus, each event is considered with full weight. The shown statistical uncertainties are calculated only from the number of entries in each bin.

The samples which are generated using the reweighting method and using WZDECAY reproduce the predicted distributions and are studied in more detail in the following. The approach using MADGRAPH5_aMC@NLO and MADSPIN will not be considered from here on due to the large deviations from the predicted distributions.

6.2 Influence of approximations

To obtain the samples of pure boson polarization several effects have to be neglected. The study of the influences of these effects is an important part of polarization studies as they lead to systematic uncertainties. The stronger the influences of these effects, the more problematic the interpretation of the results gets. For the reweighting approach a full sample is in principle allowed as input. However, again the interpretation in terms of helicity fractions is then questionable. Thus, applying restrictions on the diagrams is preferred although not necessary from a technical point of view.

The most basic approximation is the negligence of non-resonant channels. This summarizes the effects of Feynman diagrams contained in the signal where the final state leptons do not originate directly from an s channel resonance of a boson. This

approximation is dictated by technical reasons when using the WZDECAY approach. It is also reasonable to neglect these effects, though. In these diagrams the summed momentum of a lepton pair does not correspond to the boson. A measurement of the boson polarization is not reasonable, if the influence of these diagrams is large. These non-resonant diagrams are not gauge invariantly separable from the resonant diagrams. Nevertheless, the influence of the non-resonant diagrams can be suppressed using selection criteria. The s channel diagrams contain a Breit-Wigner resonance at the mass of the propagating particle. For invariant masses close to this mass the resonant diagrams dominate.

In order to estimate the influence, samples were generated including all diagramms or only resonant ones respectively using MADGRAPH5_AMC@NLO. Several kinematic distributions for these samples are compared for different phase spaces in Figure 6.10. In the more inclusive phase space there are some differences to be seen. The influence of the non-resonant diagrams cannot be neglected in this phase space. In Figure 6.10a it can be seen, that the influence is uniform in $\cos\theta^*_{W^+}$. The total cross section is increased by about 10 %. In Figure 6.10c it can be observed, that the impact is not uniform in $m(WZ)$. For $m(WZ)$ smaller than the sum of the masses of the bosons, the non-resonant diagrams dominate. Similar behavior occurs for other variables, which allows to suppress the non-resonant diagrams by choosing a tighter phase space.

This can also be seen in Figure 6.10. The plots shown in 6.10b, 6.10d, and 6.10f show the corresponding distributions in the vector boson scattering analysis phase space. The non-resonant diagrams are strongly suppressed in this phase space. Consequently, it is reasonable to neglect the effects of the non-resonant diagrams.

For the boson decay using WZDECAY an additional approximation is necessary. As the input sample is generated with the bosons in the final state the bosons have to be on-shell.

To estimate the influence of these approximations again kinematic distributions are shown in Figure 6.11 in different phase spaces. There WHIZARD samples simulated using only resonant diagrams are compared. In one of these samples the bosons are restricted to be on-shell.

The distributions of kinematic variables of jets differ. The rapidity difference of the tagging jets is smaller as it can be seen in Figure 6.11d. Furthermore, the leading jet tends to be more central and the transverse momenta of both tagging jets tend to larger values if off-shell effects are neglected. These deviations have to be studied and understood before jet-based observables can be used for a measurement of the boson polarization. The interpretation of results from these variables can only be valid once the effects on distributions of these deviations can be corrected for. Nevertheless, these effects have to be studied in more detail since additional difficulties arise by applying selection criteria in these variables.

The kinematics of the leptons show smaller deviations in the VBS phase space. If a global scaling factor is applied deviations only effect suppressed kinematic regions. Lepton-based variables are more appropriate for later polarization measurements.

An additional approximation is necessary that was not considered before. The negligence of correlations between the polarization states is an intrinsic approximation if the helicity fractions are measured. Although this is common to both methods for the production of templates the effects are treaded differently.

The reweighting method uses a mixed sample as input. In this sample the interferences are included. It is divided such that the sum of the different templates is equal to the input sample in each bin. Consequently, the interference effects are also divided and scattered in the templates. This comparison can be seen in Figure 6.12. The sample used as input is exactly divided into the different helicity fractions. There are no differences between the stacked templates and the input sample. However, it is not possible to estimate the fraction originating from interference effects using this implementation of the reweighting approach. One can also see the dominance of the template with pure transverse boson polarization $W^+_\mathrm{T} Z_\mathrm{T}$. The ratios between the different templates are obtained from the fit necessary for the reweighting method. The fractions as well as the cross sections in the total phase space can be found in Table 6.1.

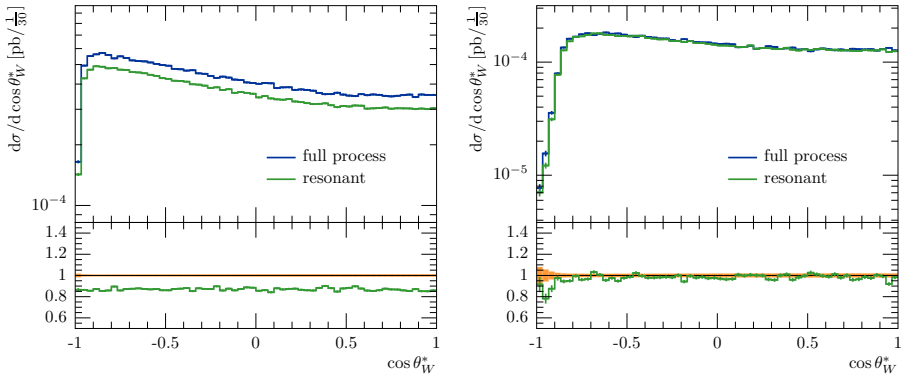

(a) $\cos\theta^*_{W^+}$, total phase space **(b)** $\cos\theta^*_{W^+}$, VBS phase space

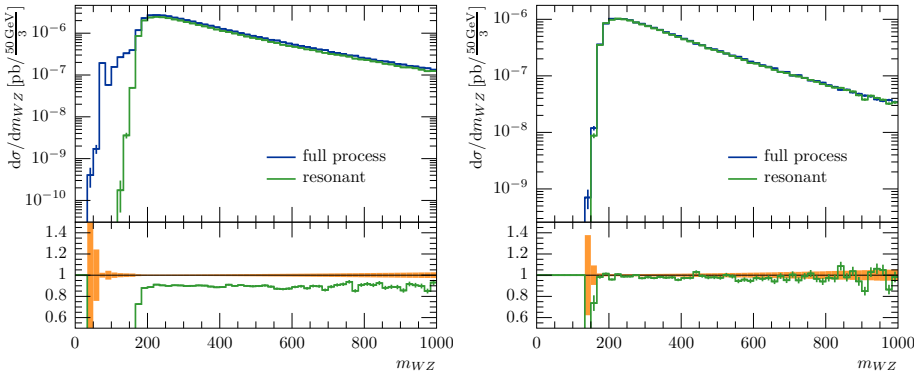

(c) $m(WZ)$, total phase space **(d)** $m(WZ)$, VBS phase space

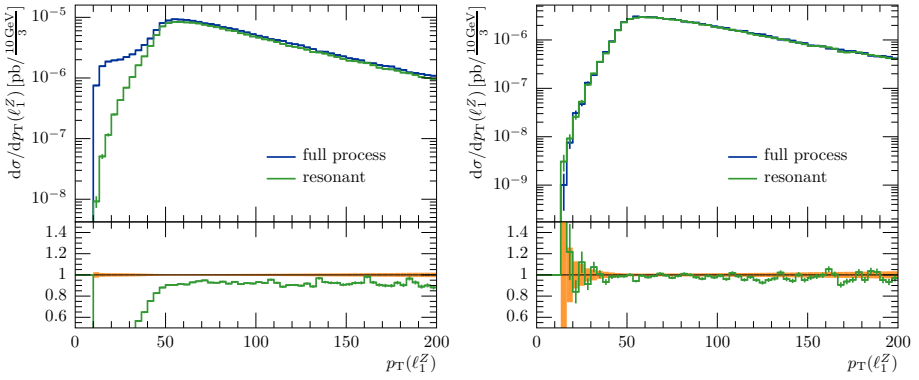

(e) $p_{\mathrm{T}}(\ell_1^Z)$, total phase space **(f)** $p_{\mathrm{T}}(\ell_1^Z)$, VBS phase space

Figure 6.10: Comparison of distributions for samples containing the full $WZjj - EW$ process (blue) and samples only containing resonant diagrams (green) in different phase spaces of samples generated using MadGraph5_aMC@NLO. On the left-hand side distributions in the total phase space and on the right-hand side for the VBS phase space are shown. In the upper row the W^+ decay angle θ^*_W, the middle row the di-boson invariant mass $m(WZ)$ and in the bottom row the transverse momentum of the leading Z-lepton $p_{\mathrm{T}}(\ell_1^Z)$ are shown.

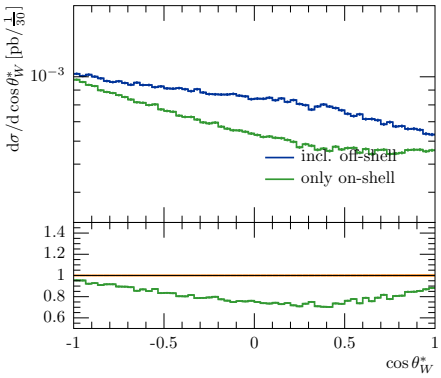

(a) $\cos\theta^*_{W^+}$, total phase space

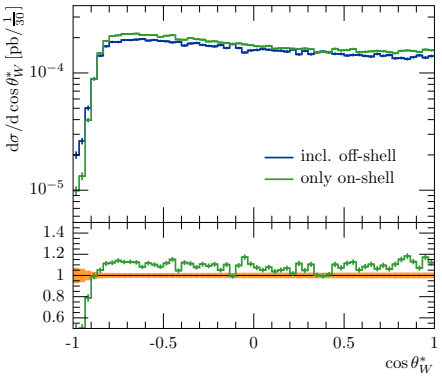

(b) $\cos\theta^*_{W^+}$, VBS phase space

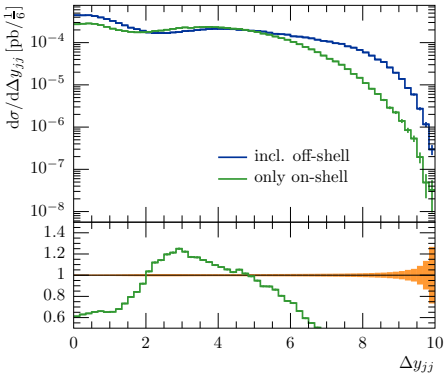

(c) $\Delta y(jj)$, total phase space

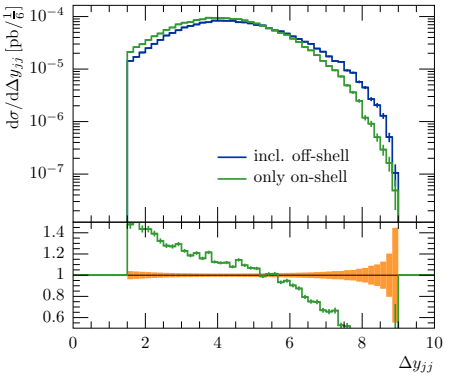

(d) $\Delta y(jj)$, VBS phase space

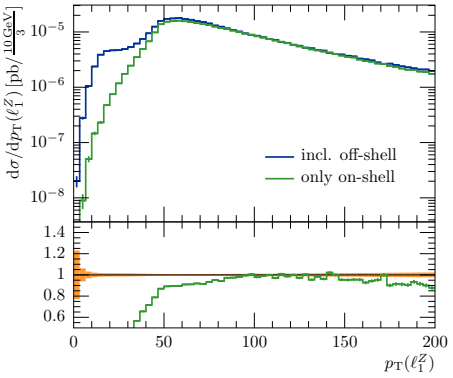

(e) $p_T(\ell_1^Z)$, total phase space

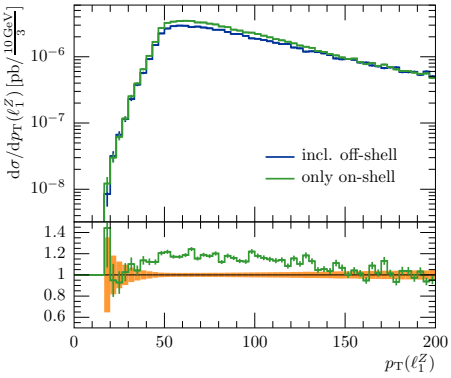

(f) $p_T(\ell_1^Z)$, VBS phase space

Figure 6.11: Comparison of distributions for samples only containing resonant diagrams of the $WZjj{-}EW$ process and simulated using WHIZARD. With additional constraint on the intermediate boson to be on-shell (green) or without constraint (blue). On the left-hand side distributions in the total phase space and on the right-hand side for the VBS phase space are shown. In the upper row the W^+ decay angle θ^*_W, the middle row the difference between the rapidities of the jets $\Delta y(jj)$, and in the bottom row the transverse momentum of the leading Z-lepton $p_T(\ell_1^Z)$ are shown.

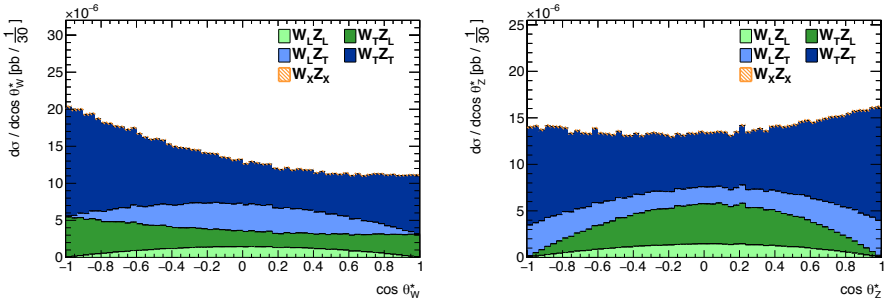

(a) $\cos\theta^*_{W+}$ **(b)** $\cos\theta^*_Z$

Figure 6.12: Comparison of stacked templates generated using the reweighting approach to the mixed sample (orange) used as input for the reweighting procedure in different variables in the total phase space. The stacked templates are scaled to the cross section of the mixed sample. Different colors represent the different helicity combinations. (a) shows the distribution in $\cos\theta^*_{W+}$ and (b) for $\cos\theta^*_Z$. Since each event is divided to the different templates the sum of the templates reproduces the input distribution.

Table 6.1: List of fractions for all helicity combinations obtained by different methods in the total phase space. Additionally, the cross sections for each sample of pure polarization in the total phase space in fb are listed. The cross section in the bottom row corresponds to the cross section of a sample with mixed helicities is shown. This sample was also used as input for the reweighting procedure. For the reweighting approach in (a) this cross section also corresponds to the sum of the cross sections of the splitted samples. This is not required in (b) since the samples are independently of each other in this case. For small interferences they should, however, be consistent. The fractions listed in the bottom row are the sums of the fractions of the splitted samples. This fraction also corresponds to the ratio of the sum of the cross sections of the splitted samples over the cross section of the mixed sample given in the bottom row.

(a) Reweighting method

	cross section in fb	fraction in %
$W^+_T Z_T$	0.4650 ± 0.0004	55.50 ± 0.07
$W^+_T Z_L$	0.1706 ± 0.0001	20.37 ± 0.02
$W^+_L Z_T$	0.1447 ± 0.0001	17.28 ± 0.02
$W^+_L Z_L$	0.0573 ± 0.0000	6.85 ± 0.01
$W^+_X Z_X$	0.8376 ± 0.0004	100.00

(b) WZDECAY

	cross section in fb	fraction in %
$W^+_T Z_T$	0.4872 ± 0.0006	58.17 ± 0.13
$W^+_T Z_L$	0.1610 ± 0.0005	19.22 ± 0.08
$W^+_L Z_T$	0.1394 ± 0.0004	16.64 ± 0.07
$W^+_L Z_L$	0.0483 ± 0.0003	5.77 ± 0.04
$W^+_X Z_X$	0.8376 ± 0.0003	99.80 ± 0.15

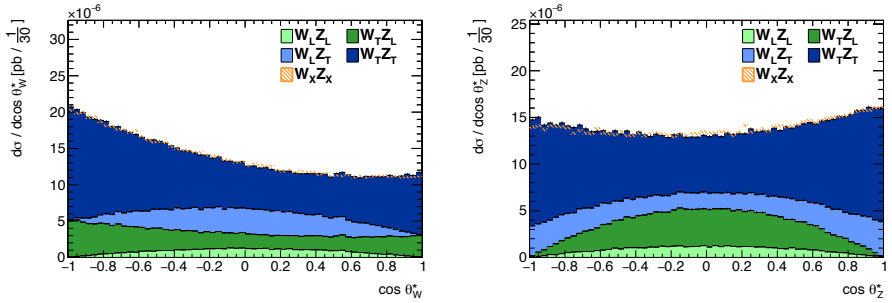

(a) $\cos\theta^*_{W+}$ **(b)** $\cos\theta^*_Z$

Figure 6.13: Comparison of stacked templates generated using WZDECAY to the mixed sample (orange) in different variables in the total phase space. Different colors represent the different helicity combinations. The stacked templates are scaled to the cross section of the mixed sample. (a) shows the distribution in $\cos\theta^*_{W+}$ and (b) for $\cos\theta^*_Z$. The mixed sample is the sample used as input for the reweighting method in which the decay of the bosons was simulated by MADGRAPH5_AMC@NLO.

The method using WZDECAY on the other hand uses a sample with stable bosons in the final state. In this way the helicity states of the bosons are defined and no interferences are included. The mixed sample with which the templates are compared is simulated using MADGRAPH5_AMC@NLO for the production and MADSPIN for the decay of the bosons. Thus, the interference effects are reconstructed as explained in Subsection 5.3.2. The sum of the templates is therefore allowed to deviate from the mixed sample. These deviations can be used as a rough estimate of the influence of the interference effects.

In Figure 6.13 the sum of the templates is compared to the mixed sample. Although small deviations can be seen, over all the agreement is very good. The dominance of the purely transversally polarized sample can again be seen. The fractions are obtained from the frequency of the helicity combination in the mixed sample with bosons in the final state. The fraction obtained after analyzing the samples obtained from MADGRAPH5_AMC@NLO are listed in Table 6.1b. Since no phase space cuts were applied after the generation the rates of the templates conform the frequencies from the MC generator listed in Table 5.1. The discrepancy of the sum of the fractions to one is small. In addition to the influence of the correlation between the helicity states, statistical uncertainties can contribute to this.

The fractions itself are in good agreement between the two methods. The sample with pure transverse polarization dominates and contributes with about 57 % to the total cross section. The pure longitudinal sample contributes only with 6 %. The samples with a longitudinally and a transversally polarized boson contribute approximately to the same amount. However, the $W^+_{\mathrm{T}}Z_{\mathrm{L}}$ samples have slightly larger fractions compared to the $W^+_{\mathrm{L}}Z_{\mathrm{T}}$ samples. In general the fraction for a transversally polarized boson is larger than the corresponding sample with longitudinal boson polarization by a factor of about three. This cannot be explained solely by combinatorics. The transverse polarization contains two helicity states. As a consequence a factor of two would be expected if helicity states where distributed uniformly. As explained in Subsection 3.2.2 the CP violation and other effects lead to deviations in the production mechanisms and kinematics for the different polarization states.

From these comparisons it can be concluded, that the approximations are reasonable. Consequently, it is valid to deduce the boson's polarization properties from the observed particles in a mixed sample in this phase space. The selection criteria suppress the influence of other diagrams strong enough to assume the leptons originate from bosons in the available samples. The effects, which are neglected, influence the kinematic of the leptons mostly uniformly. However, the jet kinematic seems more difficult. These distributions are not only scaled but also distorted by the approximations. Consequently, these jet-based variables seem not appropriate for polarization studies.

In order to use these variables anyway is only valid if all effects are well understood. This would allow for a correction of these effects.

A new version of the WHIZARD generator also allows for studies of the effects of these correlations in more detail. From version 2.2.4on it is possible to use a set of approximations of the spin density matrix used to take spin correlations into account. Using these approximations, mixed samples can be generated with the exact same approximations necessary for the generation of polarized samples, namely a diagonal spin density matrix. This sample should then be identical to the sum of the templates within statistical uncertainties. This allows to generate samples after each used approximation for a separate comparison of each step of these chain of approximations. This new version of WHIZARD was not available in time to generate these samples for this thesis though.

6.3 Influence of selection criteria

An important disadvantage of the reweighting method is its inability to ensure correct influence of selection criteria. If the reweighting is only applied in one variable other variables are not necessarily modeled correctly. Especially variables correlated to the variable in which the reweighting was applied are expected to behave incorrectly.

Since it is known from theory that the decay angle θ_V^* is correlated to the rapidity $y(V)$ and $p_{\mathrm{T}}(V)$ of the boson V the reweighting is applied independently in bins of these variables. Thereby, the dependence of θ_V^* on these variables can in principle be modeled.

The number of events necessary grows rapidly with the number of multidimensional bins for these variables though. The size of the bins has to be adjusted such that the number of events in each bin is sufficient for the fit to obtain the helicity fractions. However, large bins result in unphysical steps in the distributions of these variables. Consequently, adding another correlated variable would not be feasible as the necessary number of events would multiply. In Figure 6.14 the sample's distributions in $p_{\mathrm{T}}(W^+)$ and $y(W^+)$ can be seen. In the $p_{\mathrm{T}}(W^+)$ distribution these steps occur at 30 GeV, 60 GeV, and 90 GeV. Those values are the borders of the bins used for the reweighting. Also in the $y(W^+)$ distribution steps can be seen at the values corresponding to the bin's borders. These steps indicate that the distribution would not be modeled correctly without the correction using the fit in different $p_{\mathrm{T}}(W^+)$-$y(W^+)$ bins. The fits introduce a correction in each $p_{\mathrm{T}}(W^+)$-$y(W^+)$ bin. The shape of these distributions corresponds to the previously determined values for the helicity fraction of each bin. The jumps in the helicity fractions at the borders introduce incompatibilities in these shapes visible as steps in the distributions.

These corrections could also be necessary in other variables. However, fitting in a higher-dimensional space is infeasible due to the necessary large number of events. These effects are of special importance if selection criteria are introduced on one of the additional variables, since these possibly distort the angular distributions or distributions of other variables.

To quantify the influence on the distributions of the helicity samples the effects of cuts have to be studied and compared to samples generated using WZDECAY. For these samples the dependence is modeled correctly. In Figure 6.15 the distributions are shown for the different phase space definitions introduced in Section 5.5. In the total phase space only a cut on the number of leptons[2] is applied in the analysis. Since the samples are generated with three charged leptons in the final state and no parton shower was applied the found leptons are the three charged leptons originating of the hard process. In this phase space all events are reconstructed resulting in an acceptance of 100 %. However, some cuts have to be introduced for the simulation of the events to avoid divergences and to reduce computing time. In the definition of the detector phase space some additional cuts are included to model the reconstruction efficiency of the ATLAS detector on a very basic level. The WZ phase space is defined by additional criteria to

[2] All electrons and muons on truth level are considered.

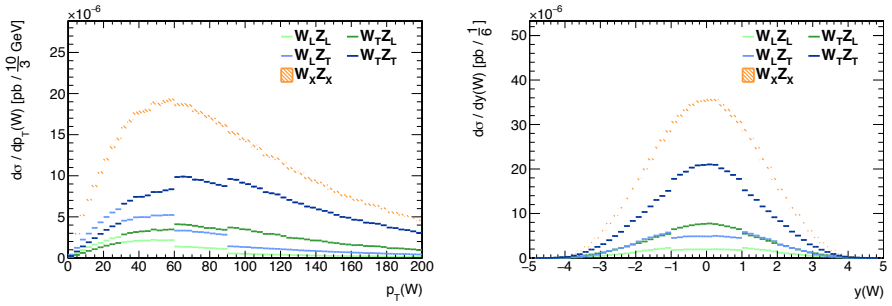

(a) $p_{\mathrm{T}}(W^+)$ **(b)** $y(W^+)$

Figure 6.14: Distributions of the helicity templates obtained using the reweighting approach in the total phase space. (a) shows the transverse momentum of the W^+ boson $p_{\mathrm{T}}(W^+)$ and (b) the rapidity $y(W^+)$ distribution. These are the variables in whose bins the reweighting was applied. The borders of the bins are clearly visible for both distributions. The orange distributions corresponds to the mixed sample used as input and the blue and green distributions to the different helicity templates.

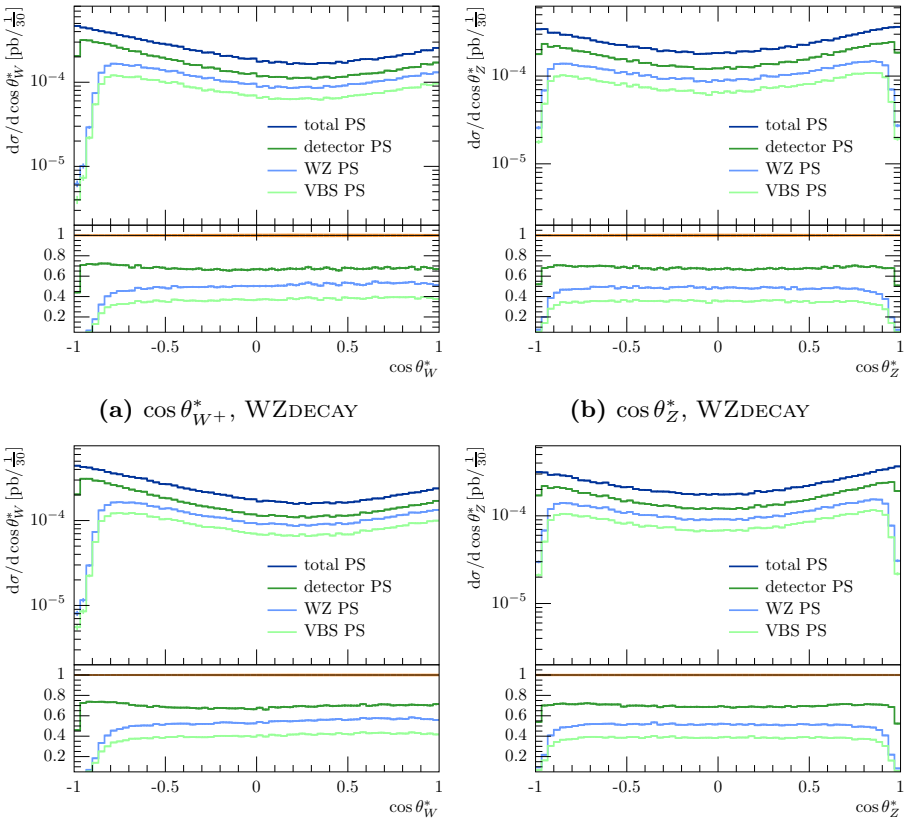

(a) $\cos\theta^*_{W^+}$, WZDECAY **(b)** $\cos\theta^*_Z$, WZDECAY

(c) $\cos\theta^*_{W^+}$, reweighting approach **(d)** $\cos\theta^*_Z$, reweighting approach

Figure 6.15: Distributions of the sample with purely transverse helicity $W_{\mathrm{T}}Z_{\mathrm{T}}$ in different phase spaces. On the left-hand side in (a) and (b) the distributions for $\cos\theta^*_{W^+}$ and on the right-hand side in (c) and (d) for $\cos\theta^*_Z$ are shown. The templates in the upper row are generated using WZDECAY and in the bottom row using the reweighting approach. The phase spaces are defined according to the Tables 5.3 and 5.4.

select WZ di-boson events such as tighter $p_{\mathrm{T}}(\ell)$ cuts and a cut on the invariant mass on the pair of leptons assigned to the Z boson. This assignment is unambiguous for the process definitions used throughout this thesis since only the channel with an electron, a muon, and an anti-muon is considered. In the VBS phase space additional cuts are applied on the jets to select the characteristic signature of two tagging jets of the vector boson scattering process.

The distributions of the different phase spaces are consistent between the two methods. Only for $|\theta_V^*|$ close to one distortions of the shape can be seen. In addition to these distortions, the influence of the cuts is distributed mainly uniformly in $\cos\theta_V^*$ resulting in a global scaling according to the total acceptance.

The $\cos\theta_Z^*$ distribution is symmetric around zero. This is expected since the angle $-\cos\theta_Z^*$ corresponds to the decay angle of the second decay product. As the decay products of the Z boson only differ in their charge the cuts influence the kinematics of both decay products equally.

In the W^+ boson case the decay products differ though. The neutrino is only accessible via the missing momentum. Therefore the neutrino's pseudorapidity cannot be reconstructed. Since no criteria on the missing momentum was applied in any phase space the kinematic of the neutrino is not restricted at all. This results in an asymmetry in $\cos\theta_{W^+}^*$ as it is observed in Figures 6.15a and 6.15b. The observed distortion is in the region of $\cos\theta_{W^+}^* \approx -1$. In this case the charged lepton's momentum is approximately anti-parallel to the boson's momentum. Consequently, the charged lepton is expected to have a small transverse momentum.

This distortion is expected to be caused for both bosons by the $p_{\mathrm{T}}(\ell)_{\mathrm{min}}$ cut. This is consistent with the behavior in the different phase spaces. In the detector phase space the effect is rather small. The $p_{\mathrm{T}}(\ell)_{\mathrm{min}}$ cut is rather small. The effect is much stronger in the WZ phase space where a harder cut of 30 GeV is applied. As the minimum transverse momentum is not changed in the VBS phase space compared to the WZ phase space both show similar shapes.

Another effect can be seen in the $\cos\theta_{W^+}^*$ distributions. The ratio between the distributions in the detector phase space and total phase space has a maximum at $\cos\theta_{W^+}^* \approx -0.9$. This indicates non-uniform influence of another selection criterion which suppresses $\cos\theta_{W^+}^* > -0.9$. Out of the variables in which selection criteria were applied, the pseudorapidity of the W^+-lepton or the transverse mass of the W^+ boson, which can is calculated as

$$m_{\mathrm{T}}(W^+) = \sqrt{2 \cdot p_{\mathrm{T}}(\ell^W) \cdot p_{\mathrm{T}}^{\mathrm{miss}} \cdot \left(1 - \cos\left(\Delta\phi\left(\vec{\ell}^W, \vec{p}_{\mathrm{T}}^{\mathrm{miss}}\right)\right)\right)}, \tag{6.3}$$

are assumed to cause this. The dependence of the decay angles θ_V^* on these variables are studied in order to distinguish between the effects of these variables and to validate the expected influence of the cut on large transverse momenta of the W^+-lepton.

Figure 6.16 shows the dependence of the decay angle θ_Z^* on the transverse momentum of the leading lepton $p_{\mathrm{T}}(\ell_1^Z)$ originating from the Z boson. A strong dependence of θ_Z^* on $p_{\mathrm{T}}(\ell_1^Z)$ can be seen, especially for $p_{\mathrm{T}}(\ell_1^Z) < 50$ GeV. Although not that strong also for larger $p_{\mathrm{T}}(\ell_1^Z)$ a dependence can be seen. For $p_{\mathrm{T}}(\ell_1^Z) < 50$ GeV large $|\theta_Z^*|$ dominate. This translates into a dominance of transverse fractions. Selecting only events with a minimal $p_{\mathrm{T}}(\ell_1^Z)$ suppresses $|\theta_Z^*| \approx 1$ as expected.

The corresponding distributions for the W^+ boson are shown in Figure 6.17. Again a clear dependence on the transverse momentum of the charged lepton can be seen. In contrast to $\cos\theta_Z^*$, $\cos\theta_{W^+}^*$ is not symmetrically distributed with respect to zero. For small transverse momenta of the W^+-lepton the $\cos\theta_{W^+}^*$ distribution peaks at -1. For higher transverse momenta of the charged lepton the maximum goes to higher $\cos\theta_{W^+}^*$. If events with a small transverse momentum of the W^+-lepton are vetoed $\cos\theta_{W^+}^* \approx -1$ are stronger suppressed. This confirms the assumptions deduced from the $\cos\theta_{W^+}^*$ distributions in different phase spaces.

As it can be seen in Figure 6.18 the $\cos\theta_{W^+}^*$ distribution does not depend at all on the transverse mass of the W^+ boson $m_{\mathrm{T}}(W^+)$. As a consequence a cut on $m_{\mathrm{T}}(W^+)$

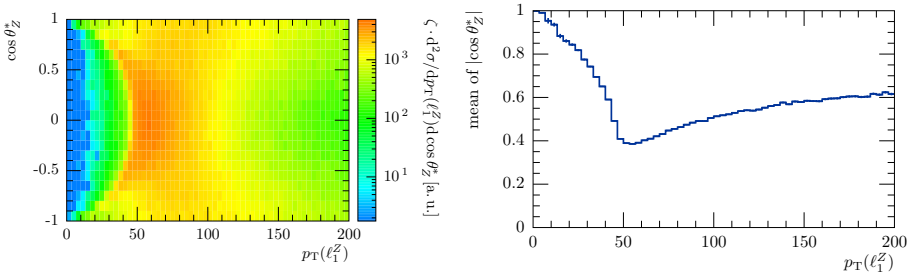

(a) $p_T(\ell^Z_1)$-$\cos\theta^*_Z$-plane **(b)** $p_T(\ell^Z_1)$, profile

Figure 6.16: Different visualizations of the dependency of the cosine of the decay angle $\cos\theta^*_Z$ on the transverse momentum of the leading Z-lepton $p_T(\ell^Z_1)$. (a) shows a 2-dimensional histogram of the distribution in the $\cos\theta^*_Z$-$p_T(\ell^Z_1)$ plane in arbitrary units (a. u.). (b) shows a profile plot of the $|\cos\theta^*_Z|$-$p_T(\ell^Z_1)$ dependency. This profile is calculated as the mean value of $|\cos\theta^*_Z|$ in each bin of $p_T(\ell^Z_1)$. For this the absolute value of $\cos\theta^*_Z$ has to be used. Otherwise the mean value would be around zero in each bin due to the symmetry of $\cos\theta^*_Z$ around zero.

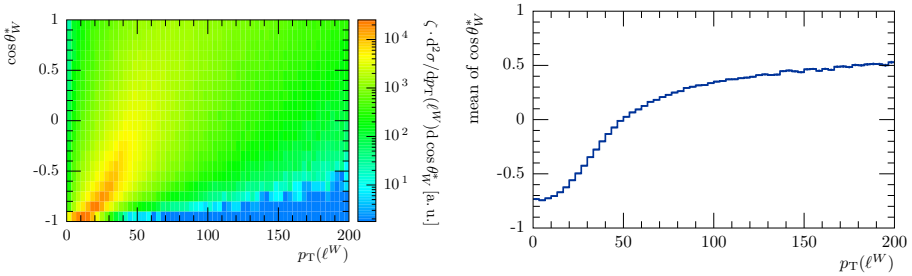

(a) $p_T(\ell^W)$-$\cos\theta^*_{W^+}$-plane **(b)** $p_T(\ell^W)$, profile

Figure 6.17: Different visualizations of the dependency of the cosine of the decay angle $\cos\theta^*_{W^+}$ on the transverse momentum of the charged W^+-lepton $p_T(\ell^W)$. (a) shows a 2-dimensional histogram of the distribution in the $\cos\theta^*_{W^+}$-$p_T(\ell^W)$ plane in arbitrary units (a. u.). (b) shows a profile plot of the $\cos\theta^*_{W^+}$-$p_T(\ell^W)$ dependency. This profile is calculated as the mean value of $\cos\theta^*_{W^+}$ in each bin of $p_T(\ell^W)$.

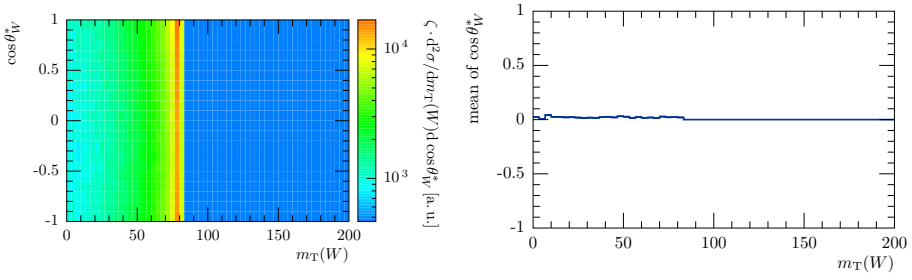

(a) $m_T(W^+)$-$\cos\theta^*_{W^+}$-plane **(b)** $m_T(W^+)$, profile

Figure 6.18: Different visualizations of the dependency of the cosine of the decay angle $\cos\theta^*_{W^+}$ on the transverse mass of the W^+ boson $m_T(W^+)$. (a) shows a 2-dimensional histogram of the distribution in the $\cos\theta^*_{W^+}$-$m_T(W^+)$ plane in arbitrary units (a. u.). (b) shows a profile plot of the $\cos\theta^*_{W^+}$-$m_T(W^+)$ dependency. This profile is calculated as the mean value of $\cos\theta^*_{W^+}$ in each bin of $m_T(W^+)$.

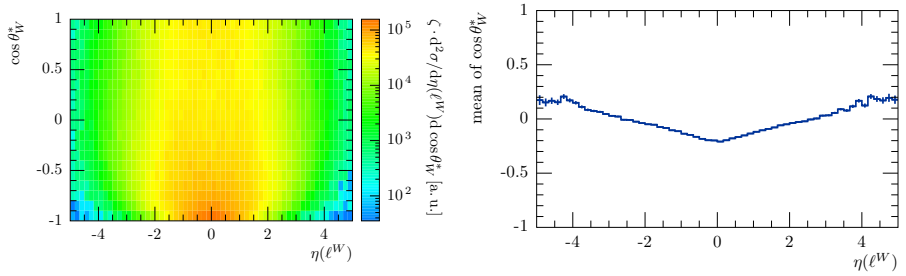

(a) $\eta(\ell^W)$-$\cos\theta^*_{W^+}$-plane **(b)** $\eta(\ell^W)$, profile

Figure 6.19: Different visualizations of the dependency of the cosine of the decay angle $\cos\theta^*_{W^+}$ on the pseudorapidity of the charged W^+-lepton $\eta(\ell^W)$. (a) shows a 2-dimensional histogram of the distribution in the $\cos\theta^*_{W^+}$-$\eta(\ell^W)$ plane in arbitrary units (a. u.). (b) shows a profile plot of the $\cos\theta^*_{W^+}$-$\eta(\ell^W)$ dependency. This profile is calculated as the mean value of $\cos\theta^*_{W^+}$ in each bin of $\eta(\ell^W)$.

cannot explain the observed maximum in the ratio between the distributions in different phase spaces in Figure 6.15.

The dependence of $\cos\theta^*_{W^+}$ on the pseudorapidity of the W^+-lepton is shown in Figure 6.19. It is again not symmetric with respect to $\cos\theta^*_{W^+} = 0$ but the dependence is not as pronounced as for the transverse momentum of the W^+-lepton. Nevertheless, for $|\eta(\ell)| > 2$ angles of $\cos\theta^*_{W^+} < -0.9$ are suppressed. This combination would require a very high boost and a high absolute value of the rapidity of the W^+ boson. Only for these kinematics a decay angle of $\cos\theta^*_{W^+} \approx -1$, for which the charged lepton's momentum partly cancels the boson's momentum, results in a high rapidity lepton. Selecting only events in which the absolute value of the pseudorapidity of the W^+-lepton is smaller than 2.5 results in the maximum in the ratio of the distributions in the detector phase space and total phase space.

Thus, the causes of the observed distortions can be explained and are well understood.

6.4 Phenomenology in VBS phase space

Having studied the influence of selection criteria for different phase spaces focus is set on the VBS phase space from here on. This is the phase space with the most sensitivity on the scattering process due to its strong background rejection.

The distributions of the decay angles $\cos\theta^*_V$ in this phase space are shown in Figure 6.20 for samples obtained using the reweighting approach and WZDECAY. The distributions of the samples with longitudinal polarization in the VBS phase space are still very similar to those in the total phase space. For the samples with transversally polarized bosons, the cut on the transverse momentum of the charged leptons caused a large deviation from the inclusive distribution for $|\cos\theta^*_V| \approx 1$.

A comparison of the sum of the helicity samples obtained from WZDECAY and a mixed sample is shown in Figure 6.21. The distributions are again in good agreement for both decay angles $\cos\theta^*_V$. As it was observed in the total phase space the sum of the reweighted templates accurately reproduces the input distribution. As this is dictated by the implementation of the reweighting method this is expected and the corresponding distributions are not shown here.

The resulting fractions of each helicity combination in the VBS phase space are listed in Table 6.2. The results are again compatible between the two methods. Taking into account only the distortions of the distributions caused by the cut on the transverse momentum of the charged leptons one would assume an enhancement of the fractions. This can, however, not be observed comparing to the fractions in Table 6.1. There is a small enhancement to be seen, the assumed effect should be around 5 % though. The cut on the pseudorapidity of the charged leptons mainly suppresses the leptons

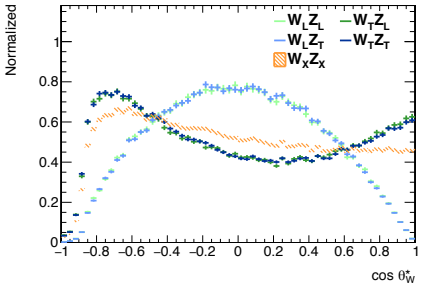

(a) $\cos\theta^*_{W+}$, reweighting approach

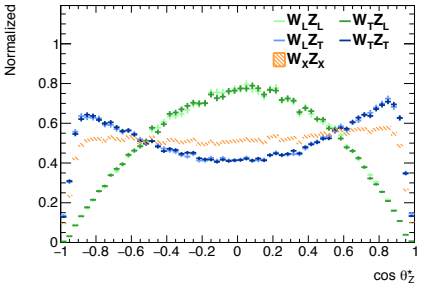

(b) $\cos\theta^*_Z$, reweighting approach

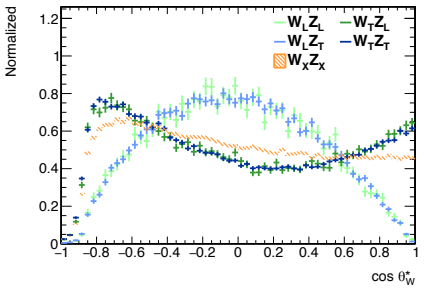

(c) $\cos\theta^*_{W+}$, WZDECAY

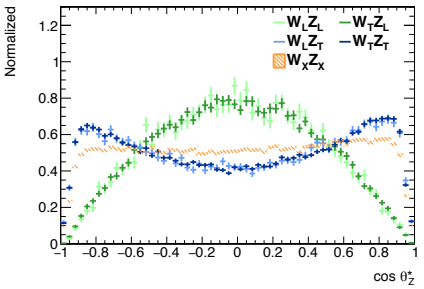

(d) $\cos\theta^*_Z$, WZDECAY

Figure 6.20: Comparison of helicity templates from different methods of obtaining purely polarized samples from input sample generated using MADGRAPH5_aMC@NLO. The samples for the distributions shown in (a) and (b) are obtained using the reweighting approach, whereas the sample shown in the bottom row in (c) and (d) are generated using WZDECAY. The normalized distributions of the cosine of the decay angle of W $\cos\theta^*_W$ (left) and Z $\cos\theta^*_Z$ (right) in the total phase space are shown. In addition to the templates with known helicity (blue and green), the distribution of a mixed sample (orange) is shown. This mixed sample was also used as input for the reweighting method.

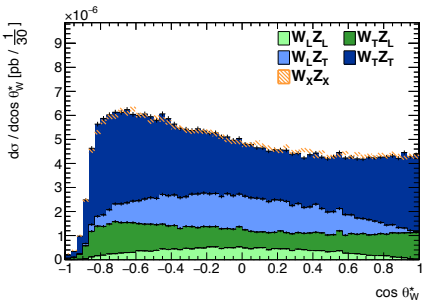

(a) $\cos\theta^*_{W+}$

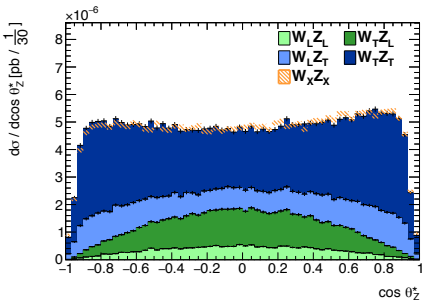

(b) $\cos\theta^*_Z$

Figure 6.21: Comparison of stacked templates generated using WZDECAY to the mixed sample (orange) used as input for the reweighting procedure in different variables in the VBS phase space. The stacked templates are scaled to the cross section of the mixed sample. Different colors represent the different helicity combinations. (a) shows the distribution in $\cos\theta^*_{W+}$ and (b) for $\cos\theta^*_Z$.

Table 6.2: List of fractions for all helicity combinations obtained by different methods in the VBS phase space. Additionally, the cross sections for each sample of pure polarization in the VBS phase space in fb are listed. The cross section in the bottom row corresponds to the cross section of a sample with mixed helicities is shown. This sample was also used as input for the reweighting procedure. For the reweighting approach in (a) this cross section also corresponds to the sum of the cross sections of the splitted samples. This is not required in (b) since the samples are independently of each other in this case. For small interferences they should, however, be consistent. The fractions listed in the bottom row are the sums of the fractions of the splitted samples. This fraction also corresponds to the ratio of the sum of the cross sections of the splitted samples over the cross section of the mixed sample given in the bottom row.

(a) Reweighting method

	cross section in fb	fraction in %
$W_{\mathrm{T}}^{+}Z_{\mathrm{T}}$	0.1639 ± 0.0001	53.83 ± 0.06
$W_{\mathrm{T}}^{+}Z_{\mathrm{L}}$	0.0604 ± 0.0000	19.83 ± 0.02
$W_{\mathrm{L}}^{+}Z_{\mathrm{T}}$	0.0578 ± 0.0000	18.97 ± 0.02
$W_{\mathrm{L}}^{+}Z_{\mathrm{L}}$	0.0224 ± 0.0000	7.37 ± 0.01
$W_{\mathrm{X}}^{+}Z_{\mathrm{X}}$	0.3044 ± 0.0001	100.00

(b) WZDECAY

	cross section in fb	fraction in %
$W_{\mathrm{T}}^{+}Z_{\mathrm{T}}$	0.1572 ± 0.0002	51.64 ± 0.14
$W_{\mathrm{T}}^{+}Z_{\mathrm{L}}$	0.0516 ± 0.0002	16.94 ± 0.08
$W_{\mathrm{L}}^{+}Z_{\mathrm{T}}$	0.0541 ± 0.0002	17.78 ± 0.09
$W_{\mathrm{L}}^{+}Z_{\mathrm{L}}$	0.0187 ± 0.0001	6.13 ± 0.05
$W_{\mathrm{X}}^{+}Z_{\mathrm{X}}$	0.3044 ± 0.0009	92.50 ± 0.40

originating from longitudinally polarized bosons. The combination of both cuts results in a slight increase of the longitudinal fraction over the transverse fraction.

As a final test of the reweighting method kinematic distributions in other variables are compared. For the reweighting approach the validity of these distributions cannot be assured. Discrepancies can arise from a mis-modeling of correlations between the transverse momentum, rapidity, or the decay angle of the bosons and other variables. If such correlations with other variables occur deviations from the real distributions are possible.

The samples simulated using WZDECAY are expected to reproduce the actual distributions in the limits of the used approximations. For these samples the narrow-width approximation is used and correlations between the helicity states are neglected. Since the narrow-width approximation was also used for the samples of the reweighting method only the neglected correlations are allowed causes of deviations between both methods. The effect of these correlations can also be estimated for instance from Figure 6.13. However, only effects smaller than 5 % have been observed there.

Any discrepancy that is not covered by this 5 % and statistical uncertainties therefore indicates additional effects. These are assumed to be caused by the wrong modeling of the reweighting method.

In Figure 6.22 a selection of kinematic variables is shown for the sample where both bosons are longitudinally polarized. A larger set of distributions for this and other helicity combinations are shown in Chapter B in the Appendix. Especially in the distribution of the transverse momentum of the W^+ boson in Figure 6.22a some large deviations occur. Again the borders of the bins used for the reweighting at 30 GeV, 60 GeV, and 90 GeV can be seen. The distribution of the sample generated using WZDECAY decreases more rapidly for higher p_{T}. The steps introduced in the reweighting also occur in the distribution of the W^+ boson rapidity shown in Figure 6.22b. These effects can be suppressed by optimizing the choice of the borders of the bins. In order to better describe the transverse momentum distribution a larger number of bins is necessary. This is not feasible with the available number of events.

In addition to the well known dependency on the bosons transverse momentum and rapidity, other variables show large deviations. This is shown for the transverse momenta of both leptons assigned to the Z boson (Fig. 6.22c and 6.22d), the transverse momentum of the leading jet (Fig. 6.22e), and the rapidity of the sub-leading jet

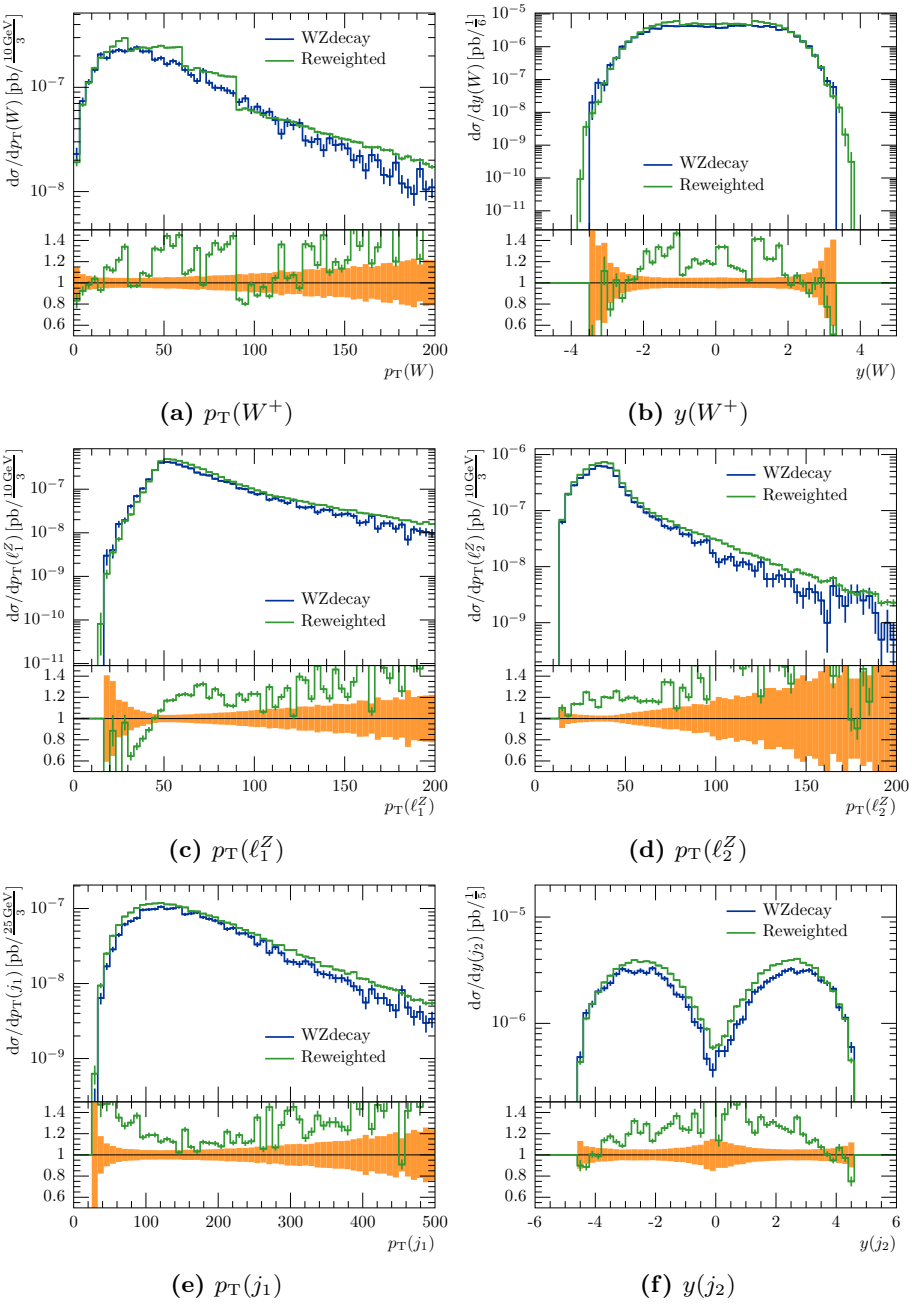

(a) $p_{\mathrm{T}}(W^+)$ **(b)** $y(W^+)$

(c) $p_{\mathrm{T}}(\ell_1^Z)$ **(d)** $p_{\mathrm{T}}(\ell_2^Z)$

(e) $p_{\mathrm{T}}(j_1)$ **(f)** $y(j_2)$

Figure 6.22: Comparison of kinematic distributions of samples of pure longitudinal polarization obtained with the different methods. Samples generated using the WZdecay approach are shown in blue and those generated by reweighting a mixed sample in green. The transverse momentum of the W^+ boson $p_{\mathrm{T}}(W^+)$ is shown in (a). (b) shows the rapidity of the W^+ boson $y(W^+)$. In (c) and (d) the transverse momenta of the leading Z-lepton $p_{\mathrm{T}}(\ell_1^Z)$ and sub-leading Z-lepton $p_{\mathrm{T}}(\ell_2^Z)$ respectively are shown. (e) shows the transverse momentum of the leading jet $p_{\mathrm{T}}(j_1)$ and (f) the rapidity of the sub-leading jet.

(Fig. 6.22f).

In all of the shown distributions deviations of more than 30 % can be seen. All of the transverse momentum distributions show deviations for high values of the transverse momentum. For these values the reweighting method overestimates the distribution for the sample with two longitudinally polarized bosons. In addition to this, the distributions of the transverse momenta of the leading jet and the leading lepton assigned to the Z boson are not well described for small values of the transverse momentum by the reweighting method. Also the rapidity of the sub-leading jet is not well described. This jet is simulated more central in the reweighting method.

The similar behavior in bins close to each other indicates systematic effects rather than statistical fluctuations. The effect of the correlations between different helicity states is estimated to be smaller than 5 %. Therefore at least a part of the deviations is assumed to arise from a mis-modeling in the reweighting method. As a consequence the reweighting method cannot be recommended for a study of the helicity fractions. Some of the discrepancies could be minimized by an optimization of the choice of bins. This would also require large amounts of statistics.

The approach of a separate boson decay using a narrow-width approximation using WZDECAY or a similar tool offers a more sophisticated method. If the narrow-width approximation is justified the only additional assumption is a small effect of correlations. This can be tested and quantified by comparing distributions to a mixed sample. The reweighting approach on the other hand relies on small dependencies of the variable which was used for the reweighting, on other variables. This can only be quantified by implementing an additional method for the simulation of the samples as it was done in this study.

To conclude the comparison of the different methods of obtaining samples with pure polarization the distribution of the helicity fractions in the $p_{\mathrm{T}}(V)$-$y(V)$ plane are shown in Figure 6.23. A similar plot is shown for the total phase space in Figure 6.7. The latter values are obtained from the template fit necessary for the reweighting. The values shown here were calculated from the distributions of the events in samples with pure polarization in the $p_{\mathrm{T}}(V)$-$y(V)$ plane. These distributions of events are shown in Figure D.2 in the Appendix. The fractions were calculated as the ratio of the sum of the event weights for a given helicity over the sum of weights for all helicity samples. Consequently, the fractions have to add up to one and correlations are neglected.

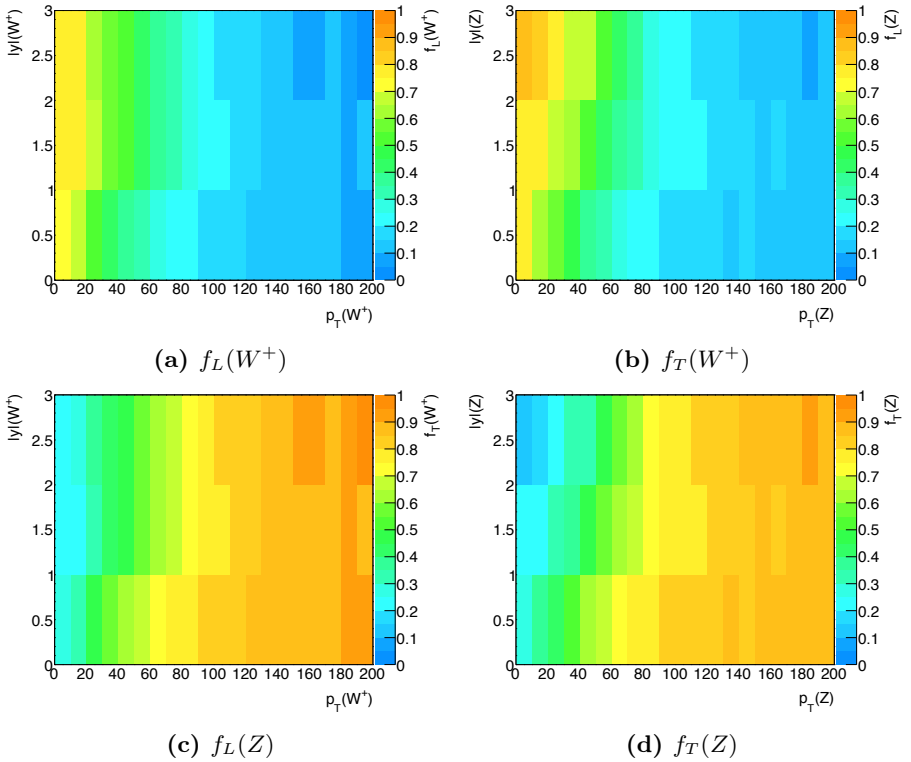

(a) $f_L(W^+)$ **(b)** $f_T(W^+)$

(c) $f_L(Z)$ **(d)** $f_T(Z)$

Figure 6.23: Helicity fractions in the $p_{\mathrm{T}}(V)$-$y(V)$ plane are shown on the left-hand side in (a) and (c) for the W^+ boson and on the right-hand side in (b) and (d) for the Z boson. The fractions are calculated as the ratio of the sum of weights for the samples with longitudinal boson over the sum of weights for the sum of all samples.

Chapter 7

Study of Observables

Most of the studies shown in Chapter 6 are performed on truth level. In particular the angle θ^*_V was calculated on truth level using the momentum information of both decay products. Since this reconstruction is not possible in an analysis this chapter is dedicated to study reconstructable observables sensitive to the boson's polarization.

7.1 Reconstruction of event kinematics

For the calculation of the decay angle θ^*_V the four-momenta of both decay products $p_\mu(\ell^V_1)$ and $p_\mu(\ell^V_2)$ have to be known. The sum of both momenta is identical to the four-momentum of the boson $p_\mu(V)$. The decay angle θ^*_V is then defined in the rest frame of the boson. Consequently, the boson's four-momentum $p_\mu(V)$ is needed for the calculation of the transformation to this frame.

In this study only the leptonic decays[1] of the bosons are considered offering more precise momentum measurement and better background suppression. Due to its short lifetime only the tau lepton's decay products can be measured. These consist of a tau-neutrino ν_τ and the decay products of a W boson. Thus, identification and reconstruction of tau leptons are more complicated and less accurate. Decays resulting in final states with tau leptons are not considered here.

7.1.1 The longitudinal momentum of the neutrino

The decay angle of the Z boson θ^*_Z can be calculated in analyses for examined decays into $e^\pm$ or $\mu^\pm$ pairs. It can therefore be used for a potential measurement of the Z boson's polarization fractions.

The leptonic decays of the $W^\pm$ bosons contain neutrinos in each channel. For this reason the decay angle $\theta^*_{W^\pm}$ cannot be fully reconstructed for any decay channel. Beside the neutrino originating from the $W^\pm$ boson every particle in the final state is assumed to be measurable. Following this assumption the missing transverse momentum $\vec{p}^{\,\text{miss}}_\text{T}$ can be identified as the transverse momentum of the neutrino $\vec{p}_\text{T}(\nu^W)$. For instance for additional neutrinos, other particles escaping the detector untracked or large mismeasurements of momenta this identification is not valid though. Neglecting these effects yields additional possibilities to reconstruct the boson's momentum. Neglecting the neutrino's mass (see Table 2.1) its four-momentum $p_\mu(\nu^W)$ can be reconstructed with only one degree of freedom.

Assuming the neutrino originates from a $W^\pm$ boson further restrictions are possible. In this case the $W^\pm$ boson's four-momentum $p_\mu(W^\pm)$ can be calculated as

$$p_\mu(W^\pm) = p_\mu(\ell^\pm) + p_\mu(\nu)\,. \tag{7.1}$$

[1] The decay of a Z boson to pairs of neutrinos are leptonic decays as well. However, these decays channels are not considered as both decay products are not measurable at the ATLAS detector.

The boson's invariant mass M_W is then given by

$$M_W^2 = p^\mu(W^\pm)p_\mu(W^\pm) = p^\mu(\ell^\pm)p_\mu(\ell^\pm) + p^\mu(\nu)p_\mu(\nu) + 2p^\mu(\ell^\pm)p_\mu(\nu) \tag{7.2}$$

$$= M_{\ell^\pm}^2 + M_\nu^2 + 2p^\mu(\ell^\pm)p_\mu(\nu)\,. \tag{7.3}$$

Subsequently, the masses of the leptons $M_{\ell^\pm}$ and M_ν are neglected which leads to

$$\frac{1}{2}M_W^2 = \left(E(\ell^\pm)E(\nu) - p_x(\ell^\pm)p_x(\nu) - p_y(\ell^\pm)p_y(\nu) - p_z(\ell^\pm)p_z(\nu)\right)\,. \tag{7.4}$$

Applying the identification of the neutrino's transverse momentum $\vec{p}_{\mathrm{T}}(\nu^W)$ with $\vec{p}_{\mathrm{T}}^{\,\mathrm{miss}}$ and demanding the W boson to be on-shell $p_z(\nu)$ is the only unknown variable in Equation (7.4). Solving this equation for $p_z(\nu)$ leads to the quadratic equation

$$0 = p_{\mathrm{T}}^2(\ell^\pm)p_z^2(\nu) - 2Cp_z(\ell^\pm)p_z(\nu) - C^2 + E^2(\ell^\pm)\left(p_{\mathrm{T}}^{\mathrm{miss}}\right)^2 \tag{7.5}$$

with

$$C = \frac{1}{2}M_W^2 + p_x(\ell^\pm)p_x(\nu) + p_y(\ell^\pm)p_y(\nu)\,. \tag{7.6}$$

Using the assumptions shown here there are up to two real solutions possible for $p_z(\nu)$

$$p_{z,\pm}(\nu) = \frac{1}{p_{\mathrm{T}}(\ell^\pm)}\left(\frac{Cp_z(\ell^\pm)}{p_{\mathrm{T}}(\ell^\pm)} \pm \sqrt{\frac{C^2p_z^2(\ell^\pm)}{p_{\mathrm{T}}^2(\ell^\pm)} + C^2 - E^2(\ell^\pm)\left(p_{\mathrm{T}}^{\mathrm{miss}}\right)^2}\right)\,. \tag{7.7}$$

A set of different algorithms is used to determine values for the longitudinal momentum of the neutrino:

$p_z^{\mathbf{min}}(\nu)$: This value represents the solution given in Equation (7.7) with the smaller absolute value. If no real solution exists the common real part of the complex solutions is chosen.

$p_z^{\mathbf{max}}(\nu)$: For this value the solution with the larger absolute value is chosen. If no real solution exists the common real part of the complex solutions is chosen. In some cases this value is unphysically large. A cut-off is introduced to avoid these cases. Instead of values larger than the total cross section 13 TeV no value is taken. As a result this value is not available for all events.

$p_z^{\mathbf{mean}}(\nu)$: In this reconstruction method the average of both solutions is chosen. This can be calculated directly as $p_z^{\mathrm{mean}}(\nu) = \frac{Cp_z(\ell^\pm)}{p_{\mathrm{T}}^2(\ell^\pm)}$. Similar to $p_z^{\mathrm{max}}(\nu)$ this value can become unphysical. This is prevented using the cut-off introduced above.

$p_z^{\mathbf{zero}}(\nu)$: This method uses only the missing transverse momentum for the momentum of the neutrino. The longitudinal component is always zero.

Based on these assumptions for $p_z(\nu)$ the corresponding decay angles θ_W^* and other variables can be calculated. Different versions of the decay angle $\theta_W^{*,\,\mathrm{min}}$, $\theta_W^{*,\,\mathrm{max}}$, $\theta_W^{*,\,\mathrm{mean}}$, and $\theta_W^{*,\,\mathrm{zero}}$, where the upper index denotes the used reconstruction method of $p_z(\nu)$, can be used as reconstructed observable.

In order to estimate the correlation to the decay angle reconstructed using the true neutrino momentum 2-dimensional histograms of the cosine of the decay angles are shown in Figure 7.1. It can be seen, that the reconstructed angles $\cos\theta_W^{*,\,\mathrm{min}}$ and $\cos\theta_W^{*,\,\mathrm{max}}$ are strongly correlated to the true $\cos\theta_W^*$. Although the distribution is much broader the angle $\cos\theta_W^{*,\,\mathrm{mean}}$ is also correlated to $\cos\theta_W^*$. The $\cos\theta_W^{*,\,\mathrm{zero}}$ is still correlated, however, it overestimates $\cos\theta_W^*$ very often. $\cos\theta_W^{*,\,\mathrm{min}}$ and $\cos\theta_W^{*,\,\mathrm{max}}$ are also biased to larger or smaller values respectively.

To quantify the validity of the reconstruction methods the fraction of correct reconstructions in bins of the true $\cos\theta_W^*$ is plotted in Figure 7.3. For this calculation a reconstruction is counted as correct if the bin containing the reconstructed value directly adjoins, or corresponds to the bin containing the true value. The integrated ratios are listed for all reconstructions in Table 7.1. It should be noted that these values are very sensitive to the acceptance for a correct reconstruction.

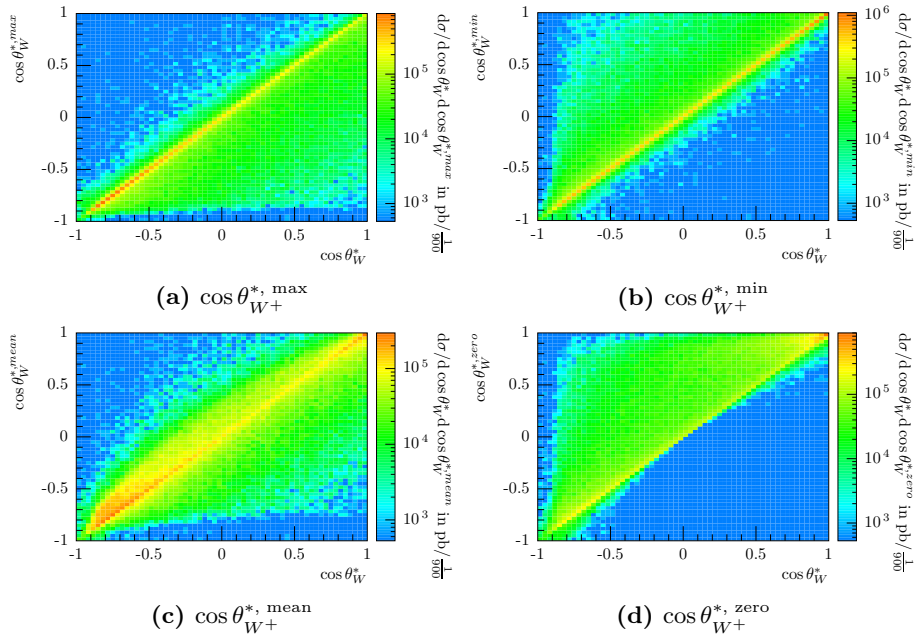

Figure 7.1: Comparison of the 2-dimensional distributions in arbitrary units (a. u.) of the different reconstructed $\cos\theta^*_{W+}$ and its value on truth level. (a) shows the distribution for the reconstruction using the $p_z^{\mathrm{max}}(\nu)$ and (b) for $p_z^{\mathrm{min}}(\nu)$. (c) shows the dependency for $\cos\theta^{*,\,\mathrm{mean}}_{W+}$ and (d) for $\cos\theta^{*,\,\mathrm{zero}}_{W+}$.

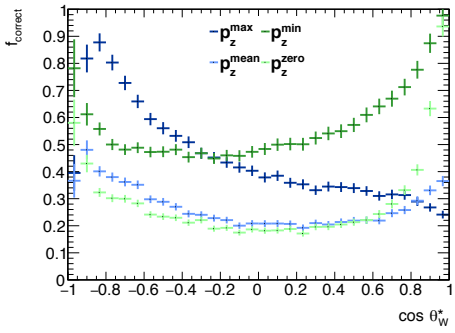

Figure 7.3: Fractions of correct reconstructions f_{correct} for the different reconstruction methods of the longitudinal momentum of the neutrino over the true $\cos\theta^*_{W+}$. A reconstruction is evaluated as correct is its value corresponds to the correct or an adjacent bin of the histogram shown in Figure 7.1.

Table 7.1: List of total fractions of correct reconstructed events for different reconstruction methods of $p_z(\nu)$. These values correspond to the mean of the entries in the distributions shown in Figure 7.3.

Method of reconstruction	Fraction of correct reconstructions
Min	0.555 ± 0.025
Max	0.461 ± 0.022
Mean	0.274 ± 0.015
Zero	0.308 ± 0.015

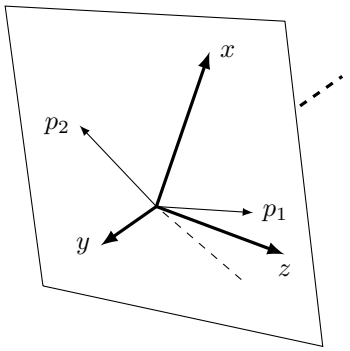

Figure 7.4: Schematic representation of the definition of the axes in the Collins-Soper frame. The y-axis is defined to be perpendicular to the event plane which is spanned by the directions of the proton momenta in the rest frame of the boson. The z-axis bisects the direction of the momentum of one of the protons, denoted with p_1, and the direction of the negative momentum of the other proton, shown as dashed line. The x-axis is also in the event plane and is perpendicular to the z-axis.

7.1.2 Decay angle in Collins-Soper frame

An alternative approach is offered by a special choice of the reference frame introduced by Collins and Soper [67]. This frame is defined such that the resulting decay angles in this frame denoted by $\theta_V^{*;\,\mathrm{CS}}$ and $\phi_V^{*;\,\mathrm{CS}}$ are largely independent of the choice of a solution of Equation (7.7) for the neutrino's longitudinal momentum in the laboratory frame.

This is achieved in a special rest frame of the boson. The x-z plane is spanned by the beam directions in this frame. The z axis is chosen to bisect the angle between the positive momentum of the first and the negative momentum of the second beam. The y axis is perpendicular to the bosons momentum in the laboratory frame. Its positive direction is given by the cross product of the z axis of the laboratory frame and the direction of the boson's transverse momentum $\vec{p}_{\mathrm{T}}(W)$. The definitions of the axes are shown in Figure 7.4.

Constraining the invariant mass of the lepton-neutrino system to the mass of the W boson M_W the lepton's momentum in this frame $\vec{p}^{\,\mathrm{CS}}(\ell)$ is given by [30]

$$p_x^{\mathrm{CS}}(\ell) = \frac{1}{2}\frac{M_W}{\sqrt{M_W^2 + p_{\mathrm{T}}(W)}}(2p_{\mathrm{T},\,||}(\ell) - p_{\mathrm{T}}(W))\,, \tag{7.8}$$

$$p_y^{\mathrm{CS}}(\ell) = p_{\mathrm{T},\,\perp}(\ell)\,, \tag{7.9}$$

$$p_z^{\mathrm{CS}}(\ell) = \pm\frac{M_W}{2}\sqrt{1 - \frac{\left(p_x^{\mathrm{CS}}(\ell)\right)^2 + \left(p_y^{\mathrm{CS}}(\ell)\right)^2}{M_W^2/4}}\,. \tag{7.10}$$

Here $p_{\mathrm{T}}(W)$ denotes the absolute value of the W boson's transverse momentum in the laboratory frame. $p_{\mathrm{T},\,||}(\ell)$ is the projection of the lepton's transverse momentum $\vec{p}_{\mathrm{T}}(\ell)$ on $\vec{p}_{\mathrm{T}}(W)$ and $p_{\mathrm{T},\,\perp}(\ell)$ denotes the part of $\vec{p}_{\mathrm{T}}(\ell)$ perpendicular to $\vec{p}_{\mathrm{T}}(W)$.

In this frame the leptons transverse momentum is independent of the neutrino's longitudinal momentum. The ambiguity of $p_z(\nu)$ in the laboratory frame is mapped in an ambiguity of the sign of $p_z^{\mathrm{CS}}(\ell)$. Using the usual definition of $\theta_W^{*,\,\mathrm{CS}}$ of this momentum $\vec{p}^{\,\mathrm{CS}}(\ell)$

$$\theta_W^{*,\,\mathrm{CS}} = \arctan\frac{\sqrt{\left(p_x^{\mathrm{CS}}(\ell)\right)^2 + \left(p_y^{\mathrm{CS}}(\ell)\right)^2}}{p_z^{\mathrm{CS}}(\ell)} \tag{7.11}$$

this ambiguity translates directly in an ambiguity of the sign of $\cos\theta_W^{*;\,\mathrm{CS}}$. Consequently, the variable $\left|\cos\theta_W^{*;\,\mathrm{CS}}\right|$ is independent of the chosen solution in Equation (7.7). If the assumptions made for the derivation of Equation (7.7) are fulfilled, the variable

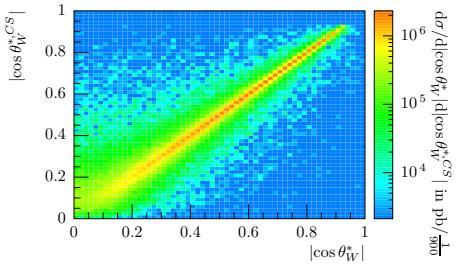

Figure 7.5: Distribution of a sample of the full process in arbitrary units (a. u.) in plane spanned by the decay angle in the Collins-Soper frame calculated using the true momentum of the neutrino and the observable $\cos\theta^{*,\,\mathrm{CS}}_{W^+}$. For this reconstruction the assumption of on-shell W^+ bosons is applied.

$\left|\cos\theta^{*,\,\mathrm{CS}}_{W}\right|$ takes the same value as if it would be calculated[2] using the true neutrino momentum. Figure 7.5 shows the distribution of a sample of the full process in a plane spanned by the cosine of the decay angle in the Collins-Soper frame calculated using the true neutrino momentum and using the reconstruction.

The distributions of samples with pure helicity which is defined in the laboratory frame in this thesis, in $\left|\cos\theta^{*,\,\mathrm{CS}}_{W}\right|$ differ from the predictions in Equation (2.39) due to the differently defined z axis. Nevertheless, this observable is assumed to be sensitive on the W boson's polarization.

7.1.3 Observables in transverse plane

In previous measurements of the helicity fractions variables in the transverse plane were used often. For this the longitudinal momenta of all particles are omitted. For small $p_{\mathrm{T}}(V)$ these variables are less sensitive. Often a high selection criterium for the transverse momentum of the W boson is applied to improve the correlation to the true decay angle θ^*_V. An increased cut is not expected to be applicable due to the low statistics in the VBS phase space. Nevertheless, some of these variables are introduced here for a study of their sensitivity.

Lepton projection L_P: This variable was introduced by the CMS Collaboration for polarization measurements of a W boson [59]. It is defined as the projection of the scaled transverse momentum of the lepton onto the normalized transverse momentum of the W boson

$$L_P = \frac{\vec{p}_{\mathrm{T}}(\ell)}{|\vec{p}_{\mathrm{T}}(W)|} \cdot \frac{\vec{p}_{\mathrm{T}}(W)}{|\vec{p}_{\mathrm{T}}(W)|}\,. \tag{7.12}$$

"Transverse helicity" angle $\theta^{*,\,\mathrm{2D}}_W$: The "transverse helicity" angle $\theta^{*,\,\mathrm{2D}}_W$ was introduced by the ATLAS Collaboration according to the full decay angle θ^*_W in the transverse plane [31]. It is defined as

$$\cos\theta^{*,\,\mathrm{2D}}_W = \frac{\vec{p}^{\,*}_{\mathrm{T}}(\ell)\cdot\vec{p}_{\mathrm{T}}(W)}{|\vec{p}^{\,*}_{\mathrm{T}}(\ell)|\,|\vec{p}_{\mathrm{T}}(W)|}\,, \tag{7.13}$$

where $\vec{p}^{\,*}_{\mathrm{T}}(\ell)$ is the transverse momentum of the lepton in the rest frame of a hypothetical W boson reconstructed using only the transverse momenta of decay products.

Ratio of transverse momenta $R_{p_{\mathrm{T}}}$: This variable was introduced by Doroba et al. in a study of beyond standard model physics models in the scattering of longitudinally polarized W bosons in the $\ell\nu\ell\nu jj$ final state [62]. It is defined as the

[2] The decay angle in this frame can also be calculated without using Equations (7.8) to (7.10), but reconstructed by applying the boost and the corresponding rotations.

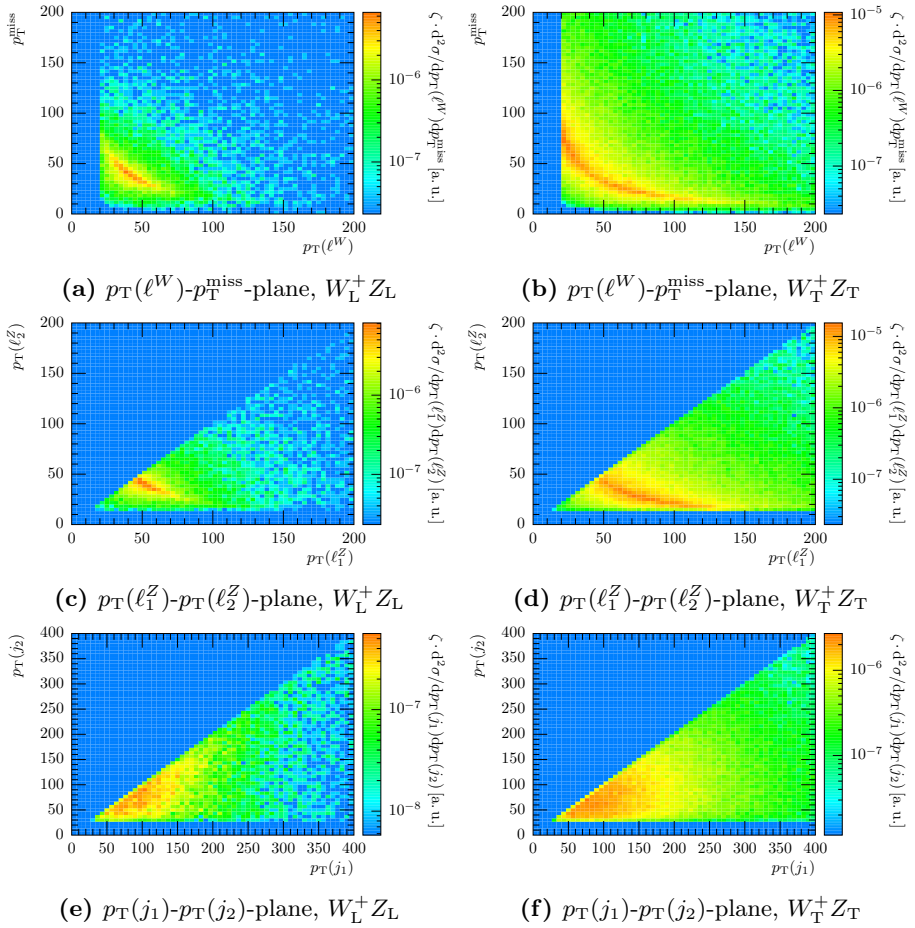

(a) $p_{\mathrm{T}}(\ell^W)$-$p_{\mathrm{T}}^{\mathrm{miss}}$-plane, $W_{\mathrm{L}}^+ Z_{\mathrm{L}}$ **(b)** $p_{\mathrm{T}}(\ell^W)$-$p_{\mathrm{T}}^{\mathrm{miss}}$-plane, $W_{\mathrm{T}}^+ Z_{\mathrm{T}}$

(c) $p_{\mathrm{T}}(\ell_1^Z)$-$p_{\mathrm{T}}(\ell_2^Z)$-plane, $W_{\mathrm{L}}^+ Z_{\mathrm{L}}$ **(d)** $p_{\mathrm{T}}(\ell_1^Z)$-$p_{\mathrm{T}}(\ell_2^Z)$-plane, $W_{\mathrm{T}}^+ Z_{\mathrm{T}}$

(e) $p_{\mathrm{T}}(j_1)$-$p_{\mathrm{T}}(j_2)$-plane, $W_{\mathrm{L}}^+ Z_{\mathrm{L}}$ **(f)** $p_{\mathrm{T}}(j_1)$-$p_{\mathrm{T}}(j_2)$-plane, $W_{\mathrm{T}}^+ Z_{\mathrm{T}}$

Figure 7.6: Two-dimensional distributions in arbitrary units (a. u.) for different combinations of observables of the purely longitudinally polarized sample compared to the purely transversely polarized samples. The plots on the left-hand side show the distributions of the sample with two longitudinal bosons and on the right-hand side of the sample with two transverse bosons. The upper row shows the distribution in the plane of the transverse momenta of the charged lepton assigned to the W^+ boson and the neutrino. The plots in the middle row show the plane of the transverse momenta of the leptons assigned to the Z boson with the leading Z-lepton on the x-axis and the plots in the bottom row show the distribution in the plan of the transverse momenta of the jets.

ratio of the product of the charged leptons' transverse momenta over the product of the jets' transverse momenta

$$R_{p_{\mathrm{T}}} = \frac{p_{\mathrm{T}}(\ell_1) \cdot p_{\mathrm{T}}(\ell_2)}{p_{\mathrm{T}}(j_1) \cdot p_{\mathrm{T}}(j_2)} \,. \tag{7.14}$$

This variable needs to be adjusted to the WZ scattering as the choice of the used leptons is not unambiguous. In this study the lepton of negative charge assigned to the Z boson was used in combination to the lepton assigned to the W boson since these leptons are also used for the definition of the decay angles θ_W^* and θ_Z^*.

Other combination of transverse momenta: In order to study whether other combinations of transverse momenta are sensitive to the bosons' helicities the distribution in a two-dimensional histogram of transverse momenta are shown and compared for different helicities in Figure 7.6.

In the distribution for the transverse momenta of the jets no significant differences are to be seen. However, the distributions of the transverse momenta of leptons,

which are assigned to a common boson, differ with the helicity of the boson. For the longitudinal helicities the distribution is quite narrow around a diagonal described by $p_{\mathrm{T}1}+p_{\mathrm{T}2} \approx 100$ GeV. The samples with transverse polarization have a broader distribution around this diagonal though. In order to quantify these combinations of the leptons' transverse momenta are introduced. The *scalar sum* S_V is given by

$$S_W = p_{\mathrm{T}}(\ell^W) + p_{\mathrm{T}}^{\mathrm{miss}}\,, \qquad S_Z = p_{\mathrm{T}}(\ell_1^Z) + p_{\mathrm{T}}(\ell_2^Z)\,, \tag{7.15}$$

where ℓ_1^V and ℓ_2^V denotes the leptons assigned to the boson V. Additionally, the transverse momentum of the bosons can be reconstructed using

$$p_{\mathrm{T}}(W) = \left|\vec{p}_{\mathrm{T}}(\ell^W) + \vec{p}_{\mathrm{T}}^{\mathrm{miss}}\right|\,, \qquad p_{\mathrm{T}}(Z) = \left|\vec{p}_{\mathrm{T}}(\ell_1^Z) + \vec{p}_{\mathrm{T}}(\ell_2^Z)\right|\,. \tag{7.16}$$

7.2 Quantification of sensitivity to boson polarization

To compare the sensitivity of the introduced variables template fits are performed. Using Rivet the distributions in these observables in the VBS phase space are determined for different samples. Subsequently, these distributions of the samples with known boson helicity are used as templates. The sum of these templates is fitted to the distribution originating from a mixed sample using an extended maximum likelihood fit (see [68]). Therefor the statistical uncertainties of the MC sample are used, i. e. the uncertainty is calculated as the square root of the number of MC events per bin. The applied fitting method does not constraint the integral of the sum to the corresponding value of the mixed sample. Nevertheless, the fractions are listed with respect to the full mixed sample. Consequently, the sum of the fractions is allowed to differ from one.

In addition to the observables introduced in Section 7.1, the transverse momentum and the (pseudo-)rapidity of the jets and leptons, and the decay angles reconstructed on truth level are studied.

In the first step a sum of the four samples generated with WZdecay and Whizard is fitted to mixed sample generated using Whizard containing only the resonant channels. Discrepancies between the sum and the mixed sample are assumed to originate only from statistical uncertainties and from neglecting correlation effects between the helicity states. Latter is assumed to be small as discussed in Section 6.4. The sum using the fitted fractions is expected to be in good agreement with the mixed sample. The results of these fits are listed in Table 7.2.

The number of events for the different helicity fractions is dictated by the MC generator used for the simulation of the bosons' production process. The resulting fractions are used as an estimate for the fractions in the mixed sample. The fit in a observable sensitive to the helicity of both bosons is thus expected to reproduce these fractions. These values are also listed in Table 7.2.

If a variable is only sensitive to the helicity of one of the bosons, the fit is only expected to reproduce the sum of the fractions with a given helicity of this boson. For instance the decay angle of the Z boson θ_Z^* is not expected to be sensitive to the helicity of the W boson. The distributions of samples with same Z helicity but different W helicity are expected to be very similar. The fit will therefore not be able to determine the helicity fractions of the W boson. However, $f(W_{\mathrm{L}}Z_{\mathrm{T}}) + f(W_{\mathrm{T}}Z_{\mathrm{T}})$ should be determined correctly. Again these values are listed in Table 7.2.

To get more accurate results for the sensitivity on the helicity of a single boson additional fits are done. For each boson the templates only differing in the helicity of the other boson are combined using the fractions dictated by the MC generator. This results in smaller statistical uncertainties of the templates and a decreased number of free parameters. Consequently, this is expected to decrease the uncertainties of the determined fractions. The results are listed in Table 7.3. The fractions itself are in good agreement to the sum of the corresponding fractions listed in Table 7.2.

As additional test the same set of fits was applied to a sample with known helicity rather then a mixed sample. Therefor the sum of the templates was fitted to one of

the templates itself. In order to exclude influence of statistical fluctuations the sample was divided using RIVET. This results in two samples whose distributions are identical besides statistical fluctuations. These fluctuations are independent from each other by construction. Due to the dominance of MC statistics the sample with transversally polarized W and Z is chosen to be divided. The results of these fits are listed in Table 7.4 for the fit of all four templates and in Table 7.5 for the fits with combined templates. Plots for all of the aforementioned fits are shown in Chapter C in the Appendix.

For a variable to be considered sensitive to the polarization of both bosons the fits with the full set of templates should reproduce the expected fractions. This should be reproducible for the fit to the mixed sample and to the sample with pure transverse polarization.

None of the studied observables fulfills these requirements. Following the argumentation in Subsection 3.2.2 the kinematics of jets was assumed to be sensitive on both bosons. This is not confirmed by the results of these fits for the studied variables. The results shown here indicate that these variables are insensitive to the bosons' helicity contradicting the assumption.

Since most of the variables introduced in Section 7.1 are assumed to be sensitive to the helicity of a single boson this sensitivity is studied in more detail below. Sensitive variables are expected to reproduce the expected fractions in the fits using combined templates (see Tab. 7.3 and 7.4). In order to compare the sensitivity of different variables fulfilling these requirements the uncertainties of the fractions obtained in the fit to the mixed sample can be used. For variables in which the distributions of the different helicity templates are well distinguishable the uncertainties are expected to be small.

Z helicity The results listed in Table 7.3b indicate a sensitivity to the Z boson's helicity of the observables $\cos\theta_W^{*,\,\mathrm{min}}$, $\cos\theta_W^{*,\,\mathrm{zero}}$, $\cos\theta_Z^*$, S_Z, $p_\mathrm{T}(\ell^W)$, $p_\mathrm{T}(\ell_1^Z)$, and $\eta(\ell_2^Z)$. The obtained fractions for fits in these variables differ from the expected values by less than 0.01.

This is not expected for the variables based on the W boson's kinematics $\cos\theta_W^{*,\,\mathrm{min}}$, $\cos\theta_W^{*,\,\mathrm{zero}}$, and $p_\mathrm{T}(\ell^W)$. The fit results of these observables are reproduced by neither of the other fits (see Tab. 7.2, 7.4, and 7.5b). This is interpreted as fluctuation and the observables are not considered as sensitive to the helicity of the Z boson.

The observables based on the leptons assigned to the Z boson $\cos\theta_Z^*$, S_Z, $p_\mathrm{T}(\ell_1^Z)$, and $\eta(\ell_2^Z)$ fulfill the requirements in the other fits though. The uncertainties for all of this observables are about 0.005. The obtained fractions differ between the observables. Nevertheless, they are compatible with the expected value within the uncertainties. Since the expected value is also an estimation based on the frequencies with which the different helicities are simulated in the boson's production process the variables have to be considered equally sensitive at this level. Comparisons of the normalized distributions of the helicity templates and the mixed sample for all of these observables are shown in Figure 7.7.

The fractions obtained from the fit of the full set of templates to the distribution with pure transverse polarization in the $\cos\theta_Z^*$ observable have very large uncertainties. This fit did not converge due to uncertainties during the optimization. This can be fixed by decreasing the number of bins suppressing the influence of statistical fluctuations. The results with a smaller number of bins are listed in Table 7.6. The resulting fractions result in a good agreement of the sum and the template of transverse polarization for both numbers of bins. This is shown in Figure 7.8. This is considered a technical issue rather than a disadvantage of this observable.

***W* helicity** Due to the large number of proposed observables and the lack of ability to reconstruct the true decay angle θ_W^* these observables are studies in more detail.

Reconstructed $\boldsymbol{\theta_W^*}$ using different $\boldsymbol{p_z(\nu)}$: The different methods of reconstruction for $p_z(\nu)$ result in fractions in the order of the expected value. The total range of the fractions for the different methods is 0.03. Interestingly also the fit in $\cos\theta_W^*$ on truth level is hardly compatible with the expected value.

Table 7.2: List of the fractions and their uncertainties for each template obtained from the fit of the full set of templates to a mixed sample in the distributions of all studied observables. In addition to the fit results the expectation for the fractions are given. The expected values are calculated as the ratio of the cross section of a given sample over the sum of the cross sections of all templates. Furthermore the sum of fractions corresponding to the same polarization state of a boson are listed.

Observable	$f(W_L Z_L)$	$f(W_T Z_L)$	$f(W_L Z_T)$	$f(W_T Z_T)$	$\sum f(W_L)$	$\sum f(W_T)$	$\sum f(Z_L)$	$\sum f(Z_T)$
exp. value	0.070	0.192	0.193	0.545	0.263	0.737	0.262	0.738
$\cos\theta^*_W$	0.045 ± 0.097	0.445 ± 0.289	0.229 ± 0.101	0.281 ± 0.291	0.274	0.726	0.490	0.510
$\cos\theta^*_Z$	0.023 ± 0.042	0.234 ± 0.043	0.131 ± 0.026	0.611 ± 0.027	0.154	0.846	0.257	0.743
$p_{\mathrm{T}}(\ell_1^Z)$	0.000 ± 0.003	0.243 ± 0.011	0.590 ± 0.131	0.167 ± 0.127	0.590	0.410	0.243	0.757
$\eta(\ell_1^Z)$	0.332 ± 0.156	0.028 ± 0.137	0.243 ± 0.351	0.397 ± 0.318	0.575	0.425	0.360	0.640
$p_{\mathrm{T}}(\ell_2^Z)$	0.163 ± 0.224	0.127 ± 0.223	0.141 ± 0.163	0.569 ± 0.158	0.304	0.696	0.290	0.710
$\eta(\ell_2^Z)$	0.042 ± 0.183	0.211 ± 0.218	0.543 ± 0.952	0.204 ± 0.908	0.584	0.416	0.253	0.747
$p_{\mathrm{T}}(\ell^W)$	0.155 ± 0.031	0.573 ± 0.052	0.059 ± 0.032	0.214 ± 0.047	0.213	0.787	0.728	0.272
$\eta(\ell^W)$	0.117 ± 0.238	0.364 ± 0.246	0.128 ± 0.231	0.391 ± 0.224	0.244	0.756	0.481	0.519
$p_{\mathrm{T}}(j_1)$	0.356 ± 0.010	0.000 ± 0.002	0.000 ± 0.002	0.644 ± 0.012	0.356	0.644	0.356	0.644
$y(j_1)$	0.215 ± 0.036	0.000 ± 0.002	0.672 ± 0.124	0.113 ± 0.090	0.887	0.113	0.215	0.785
$p_{\mathrm{T}}(j_2)$	0.281 ± 0.054	0.403 ± 0.125	0.000 ± 0.002	0.316 ± 0.097	0.281	0.719	0.684	0.316
$y(j_2)$	0.000 ± 0.001	0.000 ± 0.002	0.000 ± 0.002	1.000 ± 0.020	0.000	1.000	0.000	1.000
Δy_{jj}	0.631 ± 0.038	0.243 ± 0.084	0.127 ± 0.064	0.000 ± 0.026	0.757	0.243	0.873	0.127
$p_{\mathrm{T}}^{\mathrm{miss}}$	0.071 ± 0.097	0.436 ± 0.104	0.202 ± 0.097	0.291 ± 0.099	0.274	0.726	0.507	0.493
$\cos\theta^{*,\,\mathrm{min}}_W$	0.107 ± 0.027	0.108 ± 0.074	0.166 ± 0.027	0.619 ± 0.074	0.273	0.728	0.215	0.785
$\cos\theta^{*,\,\mathrm{max}}_W$	0.204 ± 0.052	0.000 ± 0.001	0.055 ± 0.051	0.742 ± 0.007	0.258	0.742	0.204	0.796
$\cos\theta^{*,\,\mathrm{mean}}_W$	0.035 ± 0.083	0.212 ± 0.188	0.215 ± 0.082	0.538 ± 0.184	0.250	0.750	0.247	0.753
$\cos\theta^{*,\,\mathrm{zero}}_W$	0.115 ± 0.092	0.323 ± 0.198	0.116 ± 0.089	0.445 ± 0.190	0.232	0.768	0.438	0.562
$\cos\theta^{*,\,\mathrm{CS}}_W$	0.521 ± 0.069	0.000 ± 0.001	0.479 ± 0.069	0.000 ± 0.001	1.000	0.000	0.521	0.479
$\cos\theta^{*,\,\mathrm{2D}}_W$	0.092 ± 0.034	0.171 ± 0.178	0.198 ± 0.042	0.539 ± 0.166	0.291	0.709	0.263	0.737
L_P	0.199 ± 0.036	0.359 ± 0.028	0.000 ± 0.028	0.442 ± 0.027	0.199	0.801	0.558	0.442
$R_{p_{\mathrm{T}}}$	0.000 ± 0.067	0.099 ± 0.052	0.026 ± 0.075	0.874 ± 0.027	0.026	0.974	0.099	0.901
S_W	0.201 ± 0.049	0.788 ± 0.023	0.011 ± 0.049	0.000 ± 0.120	0.212	0.788	0.989	0.011
S_Z	0.000 ± 0.001	0.256 ± 0.009	0.386 ± 0.115	0.357 ± 0.110	0.386	0.614	0.256	0.744
$p_{\mathrm{T}}(W)$	0.092 ± 0.031	0.449 ± 0.056	0.178 ± 0.032	0.282 ± 0.053	0.270	0.730	0.540	0.460
$p_{\mathrm{T}}(Z)$	0.000 ± 0.002	0.302 ± 0.009	0.166 ± 0.061	0.532 ± 0.059	0.166	0.834	0.302	0.698

Table 7.3: List of the fractions and their uncertainties for each template obtained from the fit of the combined templates for the polarization of each boson to a mixed sample in the distributions of all studied observables. In addition to the fit results the expectation for the fractions are given. The expected values are calculated as the ratio of the cross section of a given sample over the sum of the cross sections of all templates. Values are listed for the set of combined templates for the W^+ boson polarization in 7.3a and for the set of combined templates for the Z boson polarization in 7.3b

(a) W fit

Observable	$f(W_L Z_X)$	$f(W_T Z_X)$
exp. value	0.263	0.737
$\cos\theta^*_W$	0.272 ± 0.005	0.728 ± 0.006
$\cos\theta^*_Z$	0.174 ± 0.046	0.826 ± 0.046
$p_{\mathrm{T}}(\ell_1^Z)$	0.000 ± 0.011	1.000 ± 0.010
$\eta(\ell_1^Z)$	0.917 ± 0.041	0.083 ± 0.041
$p_{\mathrm{T}}(\ell_2^Z)$	0.398 ± 0.058	0.602 ± 0.058
$\eta(\ell_2^Z)$	0.320 ± 0.079	0.680 ± 0.079
$p_{\mathrm{T}}(\ell^W)$	0.246 ± 0.006	0.754 ± 0.007
$\eta(\ell^W)$	0.259 ± 0.009	0.741 ± 0.009
$p_{\mathrm{T}}(j_1)$	0.545 ± 0.020	0.455 ± 0.020
$y(j_1)$	0.824 ± 0.027	0.176 ± 0.026
$p_{\mathrm{T}}(j_2)$	0.000 ± 0.028	1.000 ± 0.026
$y(j_2)$	0.000 ± 0.001	1.000 ± 0.001
Δy_{jj}	1.000 ± 0.001	0.000 ± 0.001
$p_{\mathrm{T}}^{\mathrm{miss}}$	0.287 ± 0.005	0.713 ± 0.005
$\cos\theta^{*,\,\mathrm{min}}_W$	0.271 ± 0.006	0.729 ± 0.006
$\cos\theta^{*,\,\mathrm{max}}_W$	0.257 ± 0.006	0.743 ± 0.006
$\cos\theta^{*,\,\mathrm{mean}}_W$	0.251 ± 0.006	0.749 ± 0.006
$\cos\theta^{*,\,\mathrm{zero}}_W$	0.237 ± 0.006	0.763 ± 0.006
$\cos\theta^{*,\,\mathrm{CS}}_W$	1.000 ± 0.001	0.000 ± 0.001
$\cos\theta^{*,\,\mathrm{2D}}_W$	0.289 ± 0.009	0.711 ± 0.010
L_P	0.210 ± 0.011	0.790 ± 0.011
$R_{p_{\mathrm{T}}}$	0.000 ± 0.003	1.000 ± 0.003
S_W	0.257 ± 0.004	0.743 ± 0.005
S_Z	0.000 ± 0.017	1.000 ± 0.016
$p_{\mathrm{T}}(W)$	0.285 ± 0.004	0.715 ± 0.004
$p_{\mathrm{T}}(Z)$	0.281 ± 0.051	0.719 ± 0.051

(b) Z fit

Observable	$f(W_X Z_L)$	$f(W_X Z_T)$
exp. value	0.262	0.738
$\cos\theta^*_W$	0.488 ± 0.080	0.512 ± 0.080
$\cos\theta^*_Z$	0.258 ± 0.005	0.742 ± 0.006
$p_{\mathrm{T}}(\ell_1^Z)$	0.252 ± 0.004	0.748 ± 0.005
$\eta(\ell_1^Z)$	0.410 ± 0.015	0.590 ± 0.015
$p_{\mathrm{T}}(\ell_2^Z)$	0.289 ± 0.006	0.711 ± 0.007
$\eta(\ell_2^Z)$	0.263 ± 0.006	0.737 ± 0.007
$p_{\mathrm{T}}(\ell^W)$	0.261 ± 0.058	0.739 ± 0.058
$\eta(\ell^W)$	0.372 ± 0.065	0.628 ± 0.065
$p_{\mathrm{T}}(j_1)$	0.519 ± 0.016	0.481 ± 0.016
$y(j_1)$	0.637 ± 0.020	0.363 ± 0.020
$p_{\mathrm{T}}(j_2)$	0.768 ± 0.044	0.232 ± 0.044
$y(j_2)$	0.000 ± 0.002	1.000 ± 0.002
Δy_{jj}	1.000 ± 0.020	0.000 ± 0.002
$p_{\mathrm{T}}^{\mathrm{miss}}$	0.494 ± 0.050	0.506 ± 0.050
$\cos\theta^{*,\,\mathrm{min}}_W$	0.254 ± 0.061	0.746 ± 0.061
$\cos\theta^{*,\,\mathrm{max}}_W$	0.241 ± 0.066	0.759 ± 0.066
$\cos\theta^{*,\,\mathrm{mean}}_W$	0.223 ± 0.066	0.777 ± 0.066
$\cos\theta^{*,\,\mathrm{zero}}_W$	0.252 ± 0.064	0.748 ± 0.064
$\cos\theta^{*,\,\mathrm{CS}}_W$	0.000 ± 0.003	1.000 ± 0.003
$\cos\theta^{*,\,\mathrm{2D}}_W$	0.379 ± 0.063	0.621 ± 0.063
L_P	0.500 ± 0.071	0.500 ± 0.071
$R_{p_{\mathrm{T}}}$	0.000 ± 0.004	1.000 ± 0.004
S_W	0.406 ± 0.045	0.594 ± 0.045
S_Z	0.262 ± 0.005	0.738 ± 0.005
$p_{\mathrm{T}}(W)$	0.468 ± 0.040	0.532 ± 0.040
$p_{\mathrm{T}}(Z)$	0.297 ± 0.004	0.703 ± 0.005

Table 7.4: List of the fractions and their uncertainties for each template obtained from the fit of the full set of templates to a sample of pure transverse boson polarization in the distributions of all studied observables. In addition to the fit results the expectation for the fractions are given. Furthermore the sum of fractions corresponding to the same polarization state of a boson are listed.

Observable	$f(W_L Z_L)$	$f(W_T Z_L)$	$f(W_L Z_T)$	$f(W_T Z_T)$	$\sum f(W_L)$	$\sum f(W_T)$	$\sum f(Z_L)$	$\sum f(Z_T)$
exp. value	0.000	0.000	0.000	1.000	0.000	1.000	0.000	1.000
$\cos\theta^*_W$	0.000 ± 0.001	0.504 ± 0.326	0.006 ± 0.009	0.491 ± 0.326	0.006	0.994	0.504	0.497
$\cos\theta^*_Z$	0.001 ± 205.116	0.000 ± 677.922	0.475 ± 1.795	0.524 ± 1.775	0.476	0.524	0.001	0.999
$p_{\mathrm{T}}(\ell_1^Z)$	0.000 ± 0.005	0.000 ± 0.005	0.388 ± 0.224	0.612 ± 0.224	0.388	0.612	0.000	1.000
$\eta(\ell_1^Z)$	0.000 ± 0.005	0.000 ± 0.008	0.372 ± 0.297	0.628 ± 0.261	0.372	0.628	0.000	1.000
$p_{\mathrm{T}}(\ell_2^Z)$	0.000 ± 0.002	0.000 ± 0.003	0.000 ± 0.002	1.000 ± 0.002	0.000	1.000	0.000	1.000
$\eta(\ell_2^Z)$	0.000 ± 0.008	0.000 ± 0.003	0.549 ± 0.480	0.451 ± 0.480	0.549	0.451	0.000	1.000
$p_{\mathrm{T}}(\ell^W)$	0.000 ± 0.005	0.288 ± 0.173	0.000 ± 0.003	0.712 ± 0.164	0.000	1.000	0.288	0.712
$\eta(\ell^W)$	0.000 ± 0.015	0.000 ± 0.083	0.000 ± 0.018	1.000 ± 0.106	0.000	1.000	0.000	1.000
$p_{\mathrm{T}}(j_1)$	0.000 ± 0.041	0.036 ± 0.194	0.025 ± 0.162	0.939 ± 0.128	0.025	0.975	0.036	0.964
$y(j_1)$	0.000 ± 0.004	0.000 ± 0.012	0.089 ± 0.088	0.911 ± 0.052	0.089	0.911	0.000	1.000
$p_{\mathrm{T}}(j_2)$	0.000 ± 0.008	0.274 ± 0.189	0.276 ± 0.254	0.450 ± 0.398	0.276	0.724	0.274	0.726
$y(j_2)$	0.000 ± 1.012	0.186 ± 0.646	0.000 ± 1.251	0.814 ± 0.108	0.000	1.000	0.186	0.814
Δy_{jj}	0.000 ± 0.039	0.047 ± 0.144	0.383 ± 0.122	0.570 ± 0.113	0.383	0.617	0.047	0.953
$p_{\mathrm{T}}^{\mathrm{miss}}$	0.000 ± 0.005	0.064 ± 0.099	0.000 ± 0.004	0.936 ± 0.100	0.000	1.000	0.064	0.936
$\cos\theta^{*,\,\mathrm{min}}_W$	0.000 ± 0.002	0.195 ± 0.241	0.000 ± 0.002	0.805 ± 0.238	0.000	1.000	0.195	0.805
$\cos\theta^{*,\,\mathrm{max}}_W$	0.000 ± 0.588	0.571 ± 0.166	0.000 ± 0.134	0.429 ± 0.172	0.000	1.000	0.571	0.429
$\cos\theta^{*,\,\mathrm{mean}}_W$	0.000 ± 0.002	0.404 ± 0.226	0.000 ± 0.002	0.596 ± 0.222	0.000	1.000	0.404	0.596
$\cos\theta^{*,\,\mathrm{zero}}_W$	0.000 ± 0.005	0.255 ± 0.104	0.000 ± 0.005	0.745 ± 0.104	0.000	1.000	0.255	0.745
$\cos\theta^{*,\,\mathrm{CS}}_W$	0.000 ± 0.010	0.247 ± 0.258	0.082 ± 0.051	0.671 ± 0.276	0.082	0.918	0.247	0.753
$\cos\theta^{*,\,\mathrm{2D}}_W$	0.000 ± 0.002	0.334 ± 0.241	0.000 ± 0.002	0.666 ± 0.233	0.000	1.000	0.334	0.666
L_P	0.000 ± 0.003	0.370 ± 0.191	0.000 ± 0.003	0.630 ± 0.192	0.000	1.000	0.370	0.630
$R_{p_{\mathrm{T}}}$	0.011 ± 0.051	0.060 ± 0.228	0.000 ± 0.287	0.929 ± 0.134	0.011	0.989	0.071	0.929
S_W	0.005 ± 0.013	0.000 ± 0.020	0.000 ± 0.002	0.995 ± 0.083	0.005	0.995	0.005	0.995
S_Z	0.000 ± 0.004	0.000 ± 0.004	0.280 ± 0.161	0.720 ± 0.162	0.280	0.720	0.000	1.000
$p_{\mathrm{T}}(W)$	0.000 ± 0.094	0.002 ± 0.047	0.000 ± 0.113	0.999 ± 0.050	0.000	1.001	0.002	0.999
$p_{\mathrm{T}}(Z)$	0.000 ± 0.011	0.000 ± 0.011	0.280 ± 0.125	0.720 ± 0.126	0.280	0.720	0.000	1.000

Table 7.5: List of the fractions and their uncertainties for each template obtained from the fit of the combined templates for the polarization of each boson to a sample of pure transverse boson polarization in the distributions of all studied observables. In addition to the fit results the expectation for the fractions are given. Values are listed for the set of combined templates for the W^+ boson polarization in 7.5a and for the set of combined templates for the Z boson polarization in 7.5b

(a) W fit

Observable	$f(W_L Z_X)$	$f(W_T Z_X)$
exp. value	0.000	1.000
$\cos\theta^*_W$	0.006 ± 0.006	0.994 ± 0.007
$\cos\theta^*_Z$	1.000 ± 0.000	0.000 ± 0.000
$p_{\mathrm{T}}(\ell_1^Z)$	1.000 ± 0.000	0.000 ± 0.000
$\eta(\ell_1^Z)$	0.000 ± 0.025	1.000 ± 0.023
$p_{\mathrm{T}}(\ell_2^Z)$	1.000 ± 0.000	0.000 ± 0.001
$\eta(\ell_2^Z)$	1.000 ± 0.000	0.000 ± 0.001
$p_{\mathrm{T}}(\ell^W)$	0.000 ± 0.001	1.000 ± 0.000
$\eta(\ell^W)$	0.000 ± 0.001	1.000 ± 0.000
$p_{\mathrm{T}}(j_1)$	0.000 ± 0.001	1.000 ± 0.000
$y(j_1)$	0.000 ± 0.001	1.000 ± 0.002
$p_{\mathrm{T}}(j_2)$	0.330 ± 0.069	0.670 ± 0.069
$y(j_2)$	0.000 ± 0.087	1.000 ± 0.049
Δy_{jj}	0.000 ± 0.008	1.000 ± 0.007
$p_{\mathrm{T}}^{\mathrm{miss}}$	0.000 ± 0.000	1.000 ± 0.000
$\cos\theta^{*,\,\mathrm{min}}_W$	0.000 ± 0.001	1.000 ± 0.001
$\cos\theta^{*,\,\mathrm{max}}_W$	0.000 ± 0.001	1.000 ± 0.001
$\cos\theta^{*,\,\mathrm{mean}}_W$	0.000 ± 0.001	1.000 ± 0.001
$\cos\theta^{*,\,\mathrm{zero}}_W$	0.000 ± 0.001	1.000 ± 0.000
$\cos\theta^{*,\,\mathrm{CS}}_W$	0.063 ± 0.031	0.937 ± 0.031
$\cos\theta^{*,\,\mathrm{2D}}_W$	0.000 ± 0.001	1.000 ± 0.000
L_P	0.000 ± 0.001	1.000 ± 0.000
$R_{p_{\mathrm{T}}}$	0.000 ± 0.001	1.000 ± 0.001
S_W	0.000 ± 0.000	1.000 ± 0.000
S_Z	1.000 ± 0.000	0.000 ± 0.000
$p_{\mathrm{T}}(W)$	0.000 ± 0.000	1.000 ± 0.000
$p_{\mathrm{T}}(Z)$	1.000 ± 0.000	0.000 ± 0.000

(b) Z fit

Observable	$f(W_X Z_L)$	$f(W_X Z_T)$
exp. value	0.000	1.000
$\cos\theta^*_W$	1.000 ± 0.000	0.000 ± 0.001
$\cos\theta^*_Z$	0.000 ± 0.001	1.000 ± 0.001
$p_{\mathrm{T}}(\ell_1^Z)$	0.000 ± 0.001	1.000 ± 0.000
$\eta(\ell_1^Z)$	0.000 ± 0.003	1.000 ± 0.003
$p_{\mathrm{T}}(\ell_2^Z)$	0.000 ± 0.001	1.000 ± 0.000
$\eta(\ell_2^Z)$	0.000 ± 0.001	1.000 ± 0.000
$p_{\mathrm{T}}(\ell^W)$	1.000 ± 0.000	0.000 ± 0.001
$\eta(\ell^W)$	1.000 ± 0.002	0.000 ± 0.002
$p_{\mathrm{T}}(j_1)$	0.000 ± 0.001	1.000 ± 0.000
$y(j_1)$	0.000 ± 0.001	1.000 ± 0.002
$p_{\mathrm{T}}(j_2)$	0.260 ± 0.047	0.740 ± 0.047
$y(j_2)$	0.069 ± 0.064	0.932 ± 0.064
Δy_{jj}	0.000 ± 0.150	1.000 ± 0.141
$p_{\mathrm{T}}^{\mathrm{miss}}$	1.000 ± 0.000	0.000 ± 0.000
$\cos\theta^{*,\,\mathrm{min}}_W$	1.000 ± 0.000	0.000 ± 0.001
$\cos\theta^{*,\,\mathrm{max}}_W$	1.000 ± 0.000	0.000 ± 0.001
$\cos\theta^{*,\,\mathrm{mean}}_W$	1.000 ± 0.005	0.000 ± 0.001
$\cos\theta^{*,\,\mathrm{zero}}_W$	1.000 ± 0.003	0.000 ± 0.001
$\cos\theta^{*,\,\mathrm{CS}}_W$	0.500 ± 0.101	0.500 ± 0.101
$\cos\theta^{*,\,\mathrm{2D}}_W$	1.000 ± 0.002	0.000 ± 0.002
L_P	1.000 ± 0.005	0.000 ± 0.005
$R_{p_{\mathrm{T}}}$	0.000 ± 0.002	1.000 ± 0.002
S_W	1.000 ± 0.010	0.000 ± 0.000
S_Z	0.000 ± 0.001	1.000 ± 0.000
$p_{\mathrm{T}}(W)$	1.000 ± 0.000	0.000 ± 0.000
$p_{\mathrm{T}}(Z)$	0.000 ± 0.001	1.000 ± 0.000

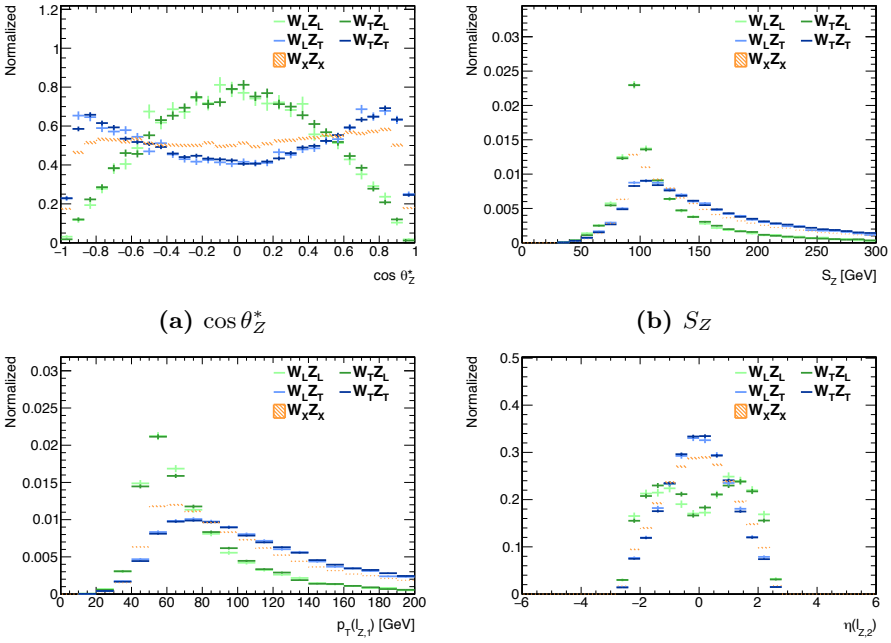

(a) $\cos\theta^*_Z$ **(b)** S_Z

(c) $p_{\mathrm{T}}(\ell_1^Z)$ **(d)** $\eta(\ell_2^Z)$

Figure 7.7: Normalized distributions of the samples of different helicity combinations (blue and green) and a mixed sample (orange) in different observables sensitive to the Z boson's polarization. (a) shows the cosine of the decay angle of the Z boson $\cos\theta^*_Z$, (b) the scalar sum of the transverse momenta of the leptons assigned to the Z boson S_Z, (c) the transverse momentum of the leading Z-lepton $p_{\mathrm{T}}(\ell_1^Z)$ and (d) the pseudorapidity of the sub-leading Z-lepton $\eta(\ell_2^Z)$.

Table 7.6: Fit result of the fit of the full set of templates to the distribution with pure transverse polarization of both bosons in the $\cos\theta^*_Z$ observable with decreased number of bins.

	fraction
$W_L Z_L$	0.006 ± 0.032
$W_T Z_L$	0.000 ± 0.004
$W_L Z_T$	0.298 ± 0.946
$W_T Z_T$	0.697 ± 0.966

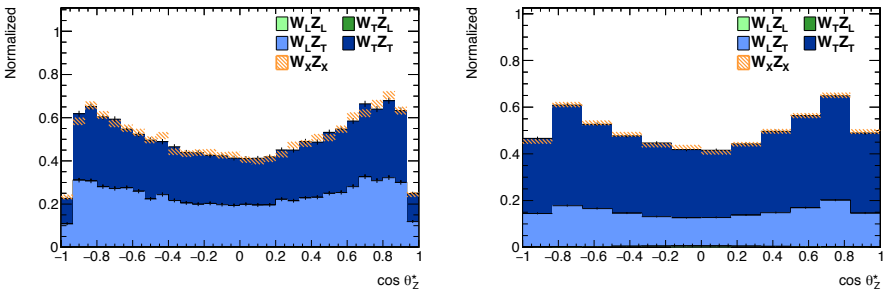

(a) $N_{\mathrm{bins}} = 30$ **(b)** $N_{\mathrm{bins}} = 12$

Figure 7.8: Stacked templates according to the fitted fractions compared to the distribution of the sample with transverse polarization (orange) in the $\cos\theta^*_Z$ for different numbers of bins.

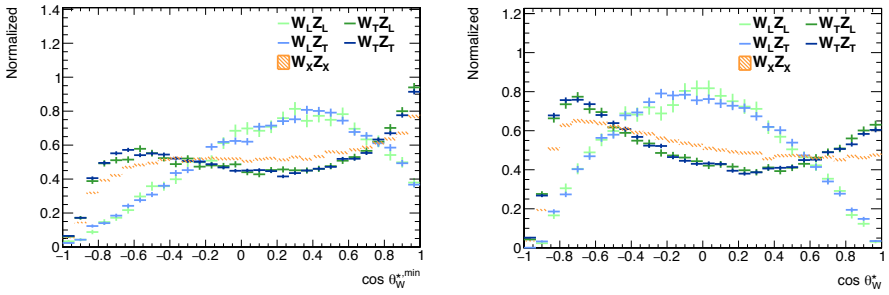

(a) $\cos\theta^{*,\,\mathrm{min}}_W$ **(b)** $\cos\theta^{*}_W$

Figure 7.9: Normalized distributions of the samples of different helicity combinations (blue and green) and a mixed sample (orange) in the reconstructed decay angle $\cos\theta^{*,\,\mathrm{min}}_{W^+}$ in (a) and the true decay angle $\cos\theta^{*,\,\mathrm{min}}_{W^+}$ in (b) are shown.

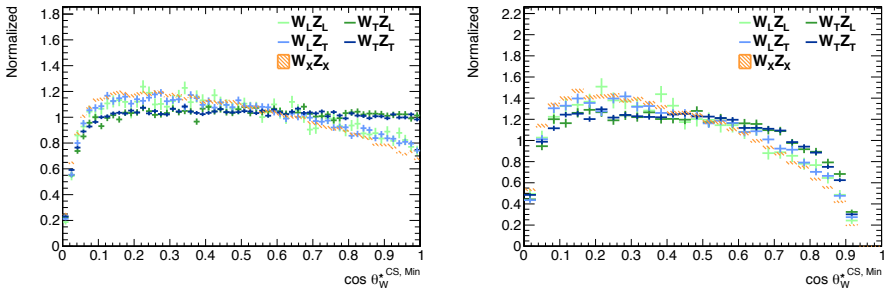

(a) total phase space **(b)** VBS phase space

Figure 7.10: Normalized distributions of the samples of different helicity combinations (blue and green) and a mixed sample (orange) in the decay angle in the Collins-Soper frame $\cos\theta^{*,\,\mathrm{CS}}_{W^+}$ in different phase spaces. In (a) the distribution in the total phase space and in (b) in the VBS phase space are shown.

A comparison of the deviations of the resulting fractions from the value obtained from the $\cos\theta^*_W$ distribution on truth level with the fractions of correct reconstructed events shows similar behavior. The $p^{\mathrm{min}}_Z(\nu)$ reconstruction is closest to the true distribution. The $p^{\mathrm{zero}}_z(\nu)$ reconstruction results in rather large deviations from the expected value and from the value obtained from $\cos\theta^*_W$. This method cannot be recommended for measurements. Distinguishing between the other methods is complicated by the observed deviations between the fraction obtained from the $\cos\theta^*_W$ distributions and the expected value. This should be studied in more detail in later studies.

As an example for these reconstruction methods the normalized distributions for different polarization templates and the mixed sample are shown for $\cos\theta^{*,\,\mathrm{min}}_W$ in comparison to $\cos\theta^*_W$ in Figure 7.9. The distributions of all variables are shown in Chapter C in the Appendix.

Decay angle in Collins-Soper frame $\theta^{*,\,\mathrm{CS}}_W$: The observable $\cos\theta^{*,\,\mathrm{CS}}_W$ is not sensitive to the bosons polarization in the analysis phase space. The resulting fractions are not compatible to the expected values in the fits to a mixed sample. This can also be seen in the distributions of the polarization templates in Figure 7.10. In addition to the distributions in the VBS phase space, the corresponding distributions in the total phase space are shown. It can be seen, that the values for $\cos\theta^{*,\,\mathrm{CS}}_W$ where the polarizations differ are suppressed by the applied phase space cuts. The distributions in the VBS phase space are hardly distinguishable from each other.

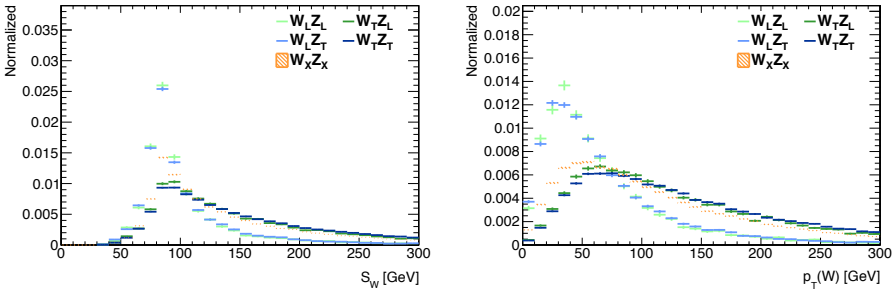

(a) S_W **(b)** $p_{\mathrm{T}}(W)$

Figure 7.11: Normalized distributions of the samples of different helicity combinations (blue and green) and a mixed sample (orange) in different observables in the transverse plane sensitive to the W^+ boson's helicity. (a) shows the distribution of the scalar sum of the transverse momenta of the charged lepton assigned to the W^+ boson and the missing momentum S_W. (b) shows the distribution of the transverse momentum of the W^+ boson $p_{\mathrm{T}}(W^+)$.

Observables in transverse plane: The lepton projection variable L_P and the cosine of the transverse helicity angle $\cos\theta^{*,\,\mathrm{2D}}_W$ are sensitive to the polarization of the W boson. The fractions for both variables show deviations from the expected value though. The ratio of transverse momenta $R_{p_{\mathrm{T}}}$ does not meet the requirements for sensitive observables. It is not considered suited for a later measurement.

The scalar sum of the transverse momenta S_W on the other hand provides a good framework. The fits in these observable reproduce the expected values. Also the uncertainties are compelling to the reconstructions of the decay angle and even to the full decay angle in the Z boson case. This indicates a good discrimination between the different templates in this observable. The distributions for S_V are shown in Figure 7.11a for both bosons.

The templates corresponding to longitudinally polarized bosons show a significant peak around the boson mass and high S_V are suppressed. The templates with transverse bosons tend to have larger S_V and the peak is much broader.

The transverse momentum of the W boson results in similar uncertainties on the fitted fractions. The obtained fractions are not in good agreement with the expected values. The distributions are shown in Figure 7.11b.

Momenta of single reconstructed objects: The transverse momenta of the jets as well as their rapidities do not show the assumed behaviour. The fitted fractions for these observables do not agree with the expected values. The assumed effect on the p_{T} of the jets seems to be suppressed by other effects. For instance polarization changes of the boson during their interactions (see Subsection 3.2.1) could cause such a suppression. The distributions of the transverse momenta of both jets are shown in Figure 7.12.

The kinematic observables of the charged lepton and the missing transverse momentum $p_{\mathrm{T}}^{\mathrm{miss}}$ are again sensitive to the boson polarization. Similar to other observables discussed above the uncertainty is very small while the resulting fractions deviate from the expected value for the transverse momenta. The pseudorapidity of the charged lepton is in good agreement to the expectations. Both variables for the charged lepton are shown in Figure 7.13.

As already mentioned in the discussion of the uncertainties in the fit to the purely transverse sample in the $\cos\theta^*_Z$ the quality of the fit depends on the choice of the binning. In order to study this the fits are redone with different number of bins N_{bins}. The histograms written in Rivet have $N_{\mathrm{bins}} = 60$. Bins cannot be divided but only completely merged by rebinning. Consequently, the available numbers of bins are divisors of the

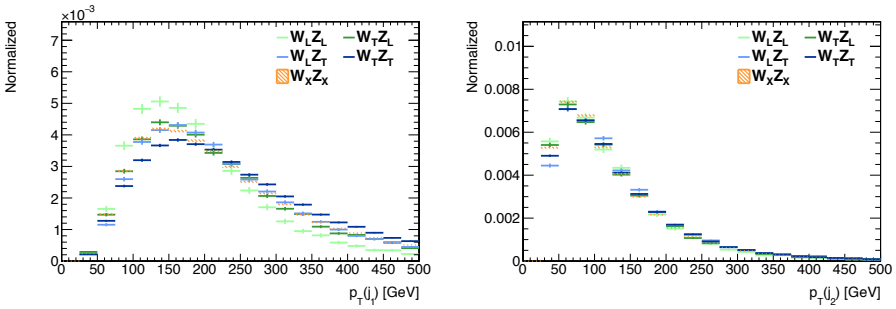

(a) $p_{\mathrm{T}}(j_1)$ **(b)** $p_{\mathrm{T}}(j_2)$

Figure 7.12: Normalized distributions of the samples of different helicity combinations (blue and green) and a mixed sample (orange) of the transverse momenta of the different jets. In (a) the distribution of the transverse momentum of the leading jet $p_{\mathrm{T}}(j_1)$ and in (b) the transverse momentum of the sub-leading jet $p_{\mathrm{T}}(j_2)$ are shown.

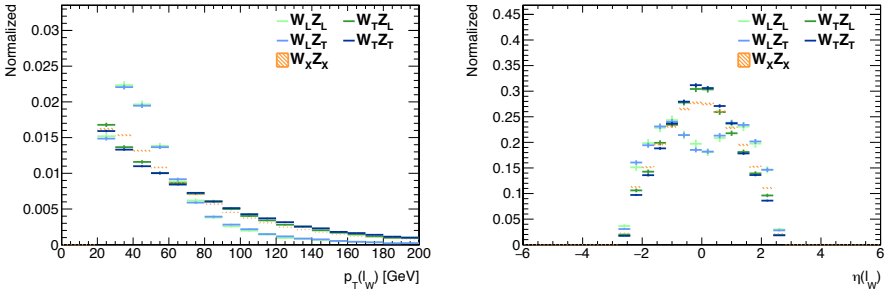

(a) $p_{\mathrm{T}}(\ell^W)$ **(b)** $\eta(\ell^W)$

Figure 7.13: Normalized distributions of the samples of different helicity combinations (blue and green) and a mixed sample (orange) of the kinematic variables of the charged lepton assigned to the W^+ boson. In (a) the distribution of the transverse momentum $p_{\mathrm{T}}(\ell^W)$ and in (b) of the pseudorapidity $\eta(\ell^W)$ are shown.

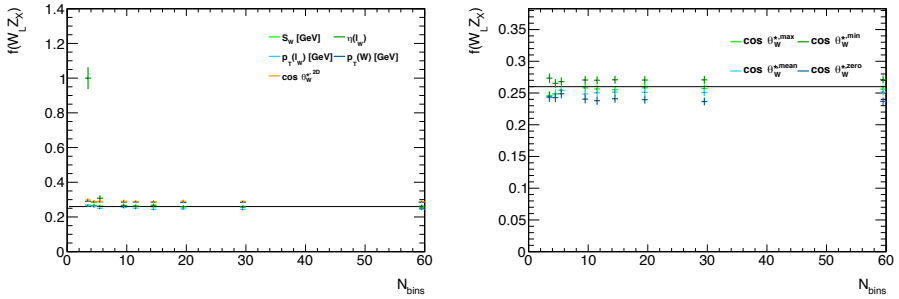

(a) W^+ observables, first set

(b) W^+ observables, second set

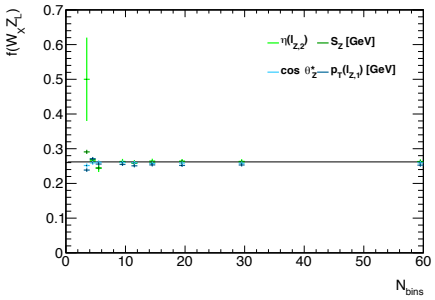

(c) Z observables

Figure 7.14: Distribution of the resulting fraction of the combined sample for the longitudinal boson polarization for fits using different numbers of bins. The upper row shows different sets of observables sensitive to the W^+ boson's polarization whereas the bottom row shows a set of observables sensitive to the Z boson's polarization. The black lines correspond to the expected value.

input N_{bin}. In Figure 7.14 the dependency of a resulting fraction on the number of bins is shown for fits in different observables. It can be seen that the values as well as the uncertainties are fairly constant for more than 15 bins. However, many of the studied observables show significant changes if less than about five bins are used. The choice for the number of bins used for the above fits of 20 or 30 is well justified.

All in all for both bosons a set of observables seems to be sensitive on the helicity. For the Z boson the decay angle $\cos\theta^*_Z$ is reconstructible and offers a possibility for a later measurement. Nevertheless, other observables also offer a good sensitivity to the helicity. For instance the transverse momenta and pseudorapidities of the leptonic decay products are very sensitive to the boson helicity.

Especially the scalar sum of the transverse momenta of both decay products S_V look promising for a later measurement. Since S_V is calculated only using the absolute values of the transverse momenta of both leptonic decay products it is also expected to be less distorted by detector effects. However, for the reconstruction of the boson's transverse momentum $p_{\text{T}}(V)$ or decay angles θ^*_V also a correct measurement of the direction of the leptons' momenta is essential.

For several observables the resulting fractions deviated from the expected value despite a very small uncertainty. This could be studied in further analyses using an additional set of samples of known boson helicity generated using the same set of parameters. These samples could be mixed to samples of varying, well-known helicity fractions. By redoing the above fits to these samples one would obtain more reliable conclusions about the sensitivity of the different observables.

7.3 Outlook for Run-2 of the LHC

To conclude a rough estimate for the uncertainties of a measurement of the polarization fractions in the $WZjj - EW$ process using data collected during the second run of

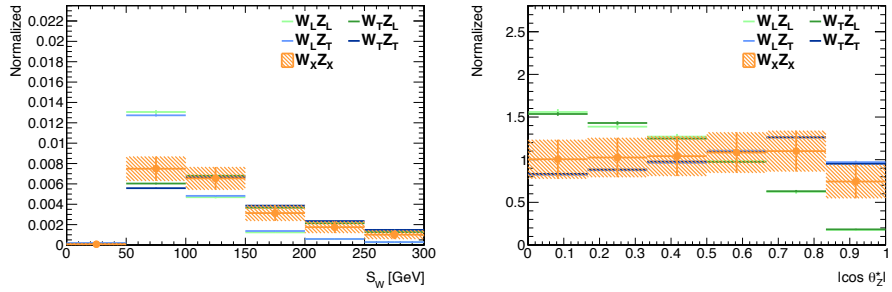

(a) S_W, normalized **(b)** $|\cos\theta^*_Z|$, normalized

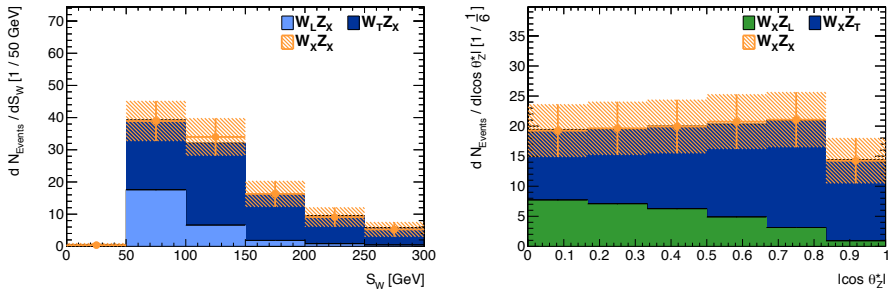

(c) S_W, fitted **(d)** $|\cos\theta^*_Z|$, fitted

Figure 7.15: Plots in the upper row show the normalized distributions of the samples of different helicity combinations (blue and green) and a mixed sample (orange). In (a) the distribution in the scalar sum of the W-leptons' transverse momenta S_W and in (b) in the absolute value of the cosine of the Z decay angle $|\cos\theta^*_Z|$ is shown. The uncertainty of the mixed sample is calculated from the statistical uncertainty of the expected number of events for $100\,\mathrm{fb}^{-1}$.
The bottom row shows a comparison of the stacked templates according to the fitted fractions and the distribution of a mixed sample scaled to the integrated luminosity of $\mathscr{L}_{\mathrm{int}} = 100\,\mathrm{fb}^{-1}$. (c) shows the comparison in the scalar sum of the W-leptons' transverse momenta S_W and (d) for $|\cos\theta^*_Z|$.

the LHC scheduled from 2015 to 2018 is given below using the obtained information. The integrated luminosity is currently estimated to be about $\mathscr{L}_{\mathrm{int}} \approx 100\,\mathrm{fb}^{-1}$. For this study the MC sample is scaled to this integrated luminosity. The used sample does only include the $e^+\nu_e\mu^\pm\mu^\pm jj$ final state. The sample is additionally scaled by a factor of four to factor the other allowed lepton combinations in. However, no scale factor was introduced for the influences of the W^- boson. The ratio of W^+/W^- depends on the phase space and the exact behavior of the templates corresponding to W^- has not been studied here.

The statistical uncertainties for the mixed sample are set to the statistical uncertainties of the corresponding event numbers assuming a Poisson distribution. The statistical uncertainties of the templates remain those of the MC sample. Systematic uncertainties have not been considered here. In a measurement, however, backgrounds have to be subtracted first leading to even larger uncertainties. For the measurement the distributions of the templates will also be distorted for instance by detector effects. Consequently, the results shown here have to be treated carefully. They should be interpreted as a lower limit on the uncertainties rather than an actual estimate. If these uncertainties are already too large a measurement would be futile.

The fits are applied in the distributions of S_W and $|\cos\theta^*_Z|$ for the set of combined templates to estimate the helicity of the bosons separately. In order to account for the large statistical uncertainties the number of bins is decreased. The symmetry of $\cos\theta^*_Z$ is exploited by using $|\cos\theta^*_Z|$ instead. The resulting distributions are shown in Figure 7.15 and the fitted fractions are listed in Table 7.7.

At this level the templates are still well distinguishable. In both observables the

Table 7.7: List of resulting fractions for a fit on the polarization of a single boson considering only the statistical uncertainty of the number of expected events for $100\,\mathrm{fb}^{-1}$. (a) lists the results for a fit to the W^+ polarization in the observable S_W and (b) lists the result for a fit of the Z boson's polarization for a fit in $|\cos\theta^*_Z|$.

(a)

	fraction
$W_L Z_X$	0.263 ± 0.128
$W_T Z_X$	0.737 ± 0.144

(b)

	fraction
$W_X Z_L$	0.260 ± 0.159
$W_X Z_T$	0.739 ± 0.170

longitudinal template differs significantly from the mixed sample despite the large statistical uncertainties. As a result the fit still converges. The uncertainties of the fractions are larger by a factor of 30 compared to the MC statistics. Nevertheless, the uncertainties are still acceptable.

Chapter 8

Summary

This thesis presents a precursory study of the polarization in the scattering of massive gauge bosons. A measurement of this polarization poses an important test of the Standard Model. The scattering process including the four-boson vertex is a prediction of the Standard Model gauge symmetry. In addition, the longitudinally polarized states of the massive gauge bosons $W^{\pm}$ and Z can be identified as the Goldstone bosons introduced by electroweak symmetry breaking. Consequently, a study of the behavior of the scattering of longitudinally polarized gauge bosons allows conclusions regarding the gauge structure of the Standard Model and the mechanism of electroweak symmetry breaking. Provided the expected integrated luminosity of $\mathscr{L}_{\text{int}} = 100\,\text{fb}^{-1}$ is achieved, these studies might be possible with the data collected during the second run of the LHC.

In this thesis, a set of tools necessary for such studies has been prepared and tested. In the first part, different approaches to obtain samples of events with known boson polarization have been introduced. The majority of previous studies of polarization has reweighted the inclusive reconstructed distribution of the decay angle of the boson to its prediction for a given polarization. An alternative approach utilizes the narrow-width approximation, which allows for the interpretation of separate polarization states of intermediate particles in the first place. Using this approximation, the full matrix element can be factorized. If in addition spin correlations are neglected, the simulation of the production and decay of the bosons can be done independently from each other. In oder to simulate the boson decays according to their helicity state the tool WZDECAY has been implemented in this thesis. Having studied the effect of the applied approximations in different phase spaces, both approaches have been validated and compared for the $e^+\nu_e\mu^+\mu^- jj - EW$ final state at a center-of-mass energy of $\sqrt{s} = 13$ TeV. Since the reweighting approach cannot ensure correct behavior of the samples in kinematic distributions, the approach using WZDECAY is favored.

In addition, the sensitivities of different observables have been studied at a center-of-mass energy of 13 TeV. The superior reconstruction ability of the event kinematics lead to a choice of the $e^+\nu_e\mu^+\mu^- jj - EW$ final state rather than the like-sign $\ell^{\pm}\nu_\ell\ell'^{\pm}\nu_\ell jj - EW$ final state despite the lower signal-to-background ratio. In order to study the sensitivity, template fits have been employed for distributions of these variables in the analysis phase space. The templates for the different helicity combinations have been obtained from samples generated using WZDECAY at parton level. The comparison of the resulting fractions and their uncertainties have been used to quantify the sensitivities of each observable on the polarization of the boson in question. The transverse momentum as well as the pseudorapidity of the charged lepton assigned to the W^+ boson and the scalar sum of the transverse momentum of the charged lepton assigned to the W^+ boson and the missing transverse momentum, S_W, show the highest sensitivity to the polarization of the W^+ boson. For the Z boson, the cosine of the decay angle $\cos\theta^*_Z$ and the scalar sum of the transverse momenta of the lepton pair assigned to the Z boson, S_Z, prove to be most sensitive. The distributions scaled to the integrated luminosity of $\mathscr{L}_{\text{int}} = 100\,\text{fb}^{-1}$ for two of these observables are shown in

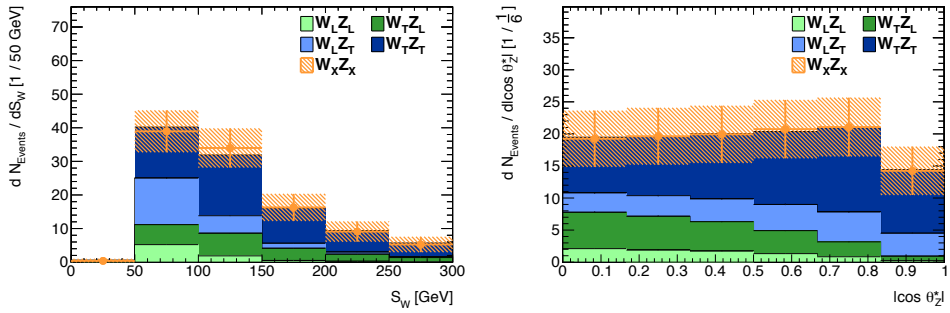

(a) S_W, fitted **(b)** $|\cos\theta_Z^*|$, fitted

Figure 8.1: Comparison of stacked templates generated using WZDECAY according to the fractions obtained from generation in WHIZARD (blue and green) to a mixed sample (orange) scaled to $100\,\mathrm{fb}^{-1}$. In (a) the distribution of the scalar sum of the W-leptons' transverse momenta S_W and in (b) of the absolute value of the cosine of the Z decay angle $|\cos\theta_Z^*|$ are shown.

Figure 8.1. Even for the small number of events, the templates deviate significantly from the mixed sample allowing for a possible measurement of the fractions for each template.

For such a measurement, additional effects are to be considered. Subsequent studies will have to evaluate systematic uncertainties. These arise for instance from subtraction of backgrounds, theory uncertainties, and detector effects. In addition to this, the full $\ell^\pm\nu_\ell\ell'^\pm\ell'^\mp jj{-}EW$ final state rather than just the $e^+\nu_e\mu^+\mu^- jj{-}EW$ final state studied in this thesis will have to be considered.

The presented results build the groundwork for a future measurement of polarizations of bosons in the $VVjj-EW$ process. A measurement of the cross section in a phase space enriched with longitudinally polarized bosons or even a measurement of the helicity fractions in this process will be a powerfull test of the Standard Model.

Appendix A

Mathematical definitions

Pauli spin matrices:

$$\sigma_1 = \begin{pmatrix} 0 & 1 \\ 1 & 0 \end{pmatrix}, \qquad \sigma_2 = \begin{pmatrix} 0 & -i \\ i & 0 \end{pmatrix}, \qquad \sigma_3 = \begin{pmatrix} 1 & 0 \\ 0 & -1 \end{pmatrix}. \tag{A.1}$$

γ-matrices (Dirac-Pauli representation):

$$\gamma^0 = \begin{pmatrix} 1 & 0 & 0 & 0 \\ 0 & 1 & 0 & 0 \\ 0 & 0 & -1 & 0 \\ 0 & 0 & 0 & -1 \end{pmatrix}, \qquad \gamma^1 = \begin{pmatrix} 0 & 0 & 0 & 1 \\ 0 & 0 & 1 & 0 \\ 0 & -1 & 0 & 0 \\ -1 & 0 & 0 & 0 \end{pmatrix}, \tag{A.2}$$

$$\gamma^2 = \begin{pmatrix} 0 & 0 & 0 & -i \\ 0 & 0 & i & 0 \\ 0 & i & 0 & 0 \\ -i & 0 & 0 & 0 \end{pmatrix}, \qquad \gamma^3 = \begin{pmatrix} 0 & 0 & 1 & 0 \\ 0 & 0 & 0 & -1 \\ -1 & 0 & 0 & 0 \\ 0 & 1 & 0 & 0 \end{pmatrix}. \tag{A.3}$$

with

$$\left(\gamma^0\right)^2 = \mathbb{1}\,, \quad \left(\gamma^k\right)^2 = -\mathbb{1}\,, \quad \gamma^{0\dagger} = \gamma^0\,, \quad \gamma^{k\dagger} = -\gamma^k\,, \quad \gamma^\mu\gamma^\nu + \gamma^\nu\gamma^\mu = 2g^{\mu\nu}\,. \tag{A.4}$$

$$\gamma^5 = i\gamma^0\gamma^1\gamma^2\gamma^3 = \begin{pmatrix} 0 & 0 & 1 & 0 \\ 0 & 0 & 0 & 1 \\ 1 & 0 & 0 & 0 \\ 0 & 1 & 0 & 0 \end{pmatrix}. \tag{A.5}$$

with

$$\left(\gamma^5\right)^2 = \mathbb{1}\,, \qquad \gamma^{5\dagger} = \gamma^5\,, \qquad \gamma^5\gamma^\mu = \gamma^\mu\gamma^5\,. \tag{A.6}$$

Appendix B

Comparison of Templates obtained using Different Methods

The following figures show kinematic distributions of samples of pure longitudinal polarization obtained with different methods in the VBS phase space. Samples generated using the WZDECAY approach are shown in blue and those generated by reweighting a mixed sample in green. In each section shows a given combination of boson polarizations.

B.1 Events with purely longitudinal boson polarization

The figures in this section show the distributions of the samples of events with purely longitudinal boson polarization.

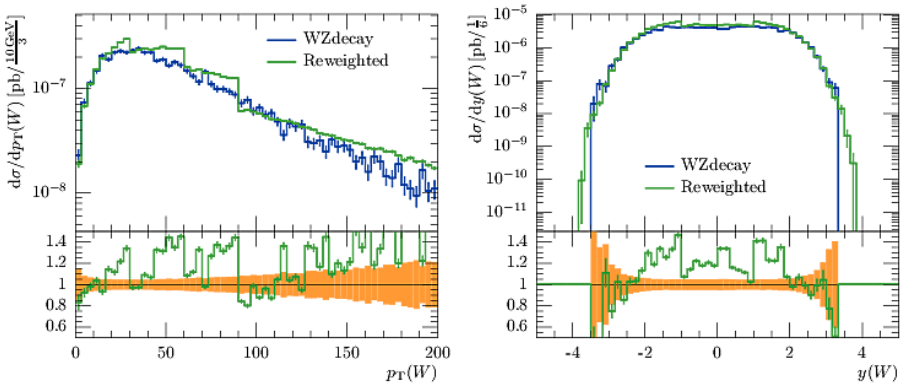

(a) $p_T(W^+)$ **(b)** $y(W^+)$

For further information see beginning of Chapter B

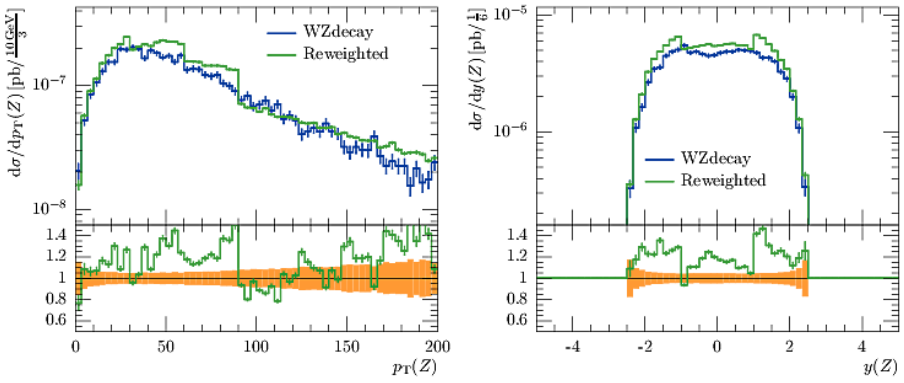

(a) $p_T(Z)$ **(b)** $y(Z)$

For further information see beginning of Chapter B

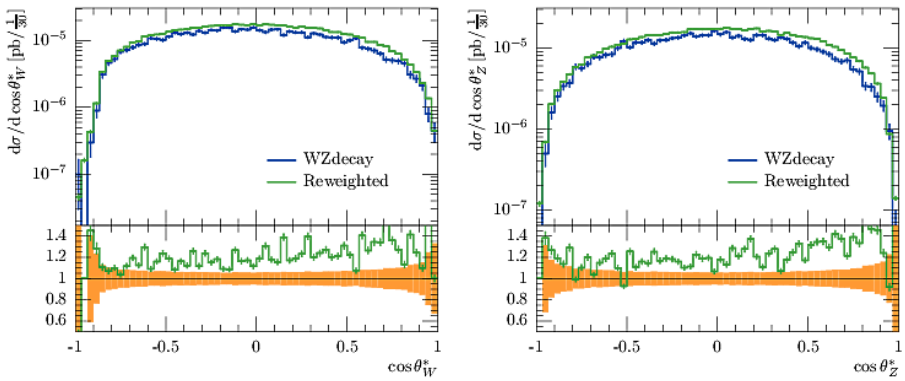

(a) $\cos\theta^*_W$ **(b)** $\cos\theta^*_Z$

For further information see beginning of Chapter B

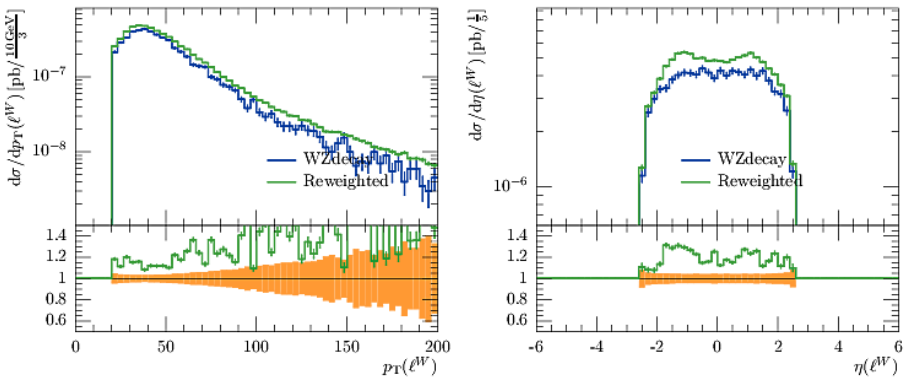

(a) $p_T(\ell^W)$ **(b)** $\eta(\ell^W)$

For further information see beginning of Chapter B

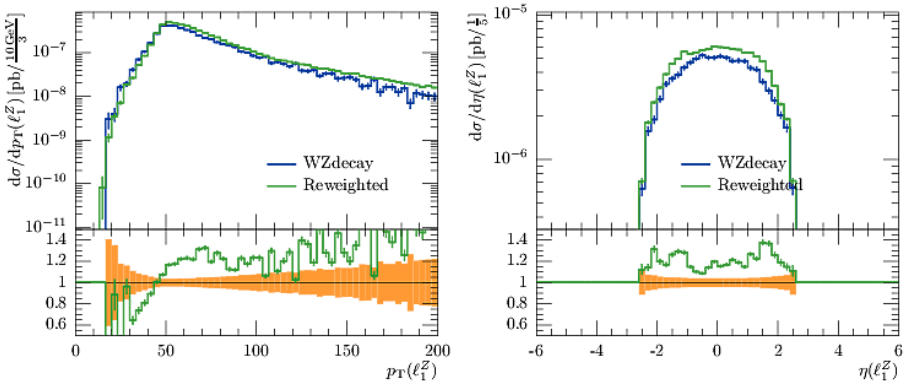

(a) $p_T(\ell_1^Z)$ **(b)** $\eta(\ell_1^Z)$

For further information see beginning of Chapter B

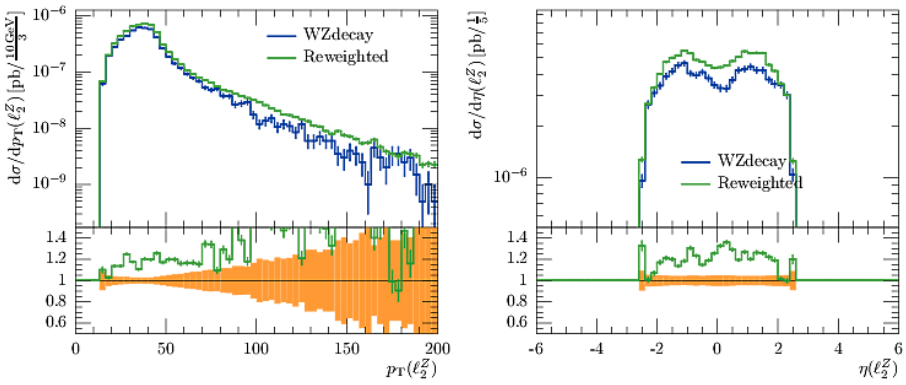

(a) $p_T(\ell_2^Z)$ **(b)** $\eta(\ell_2^Z)$

For further information see beginning of Chapter B

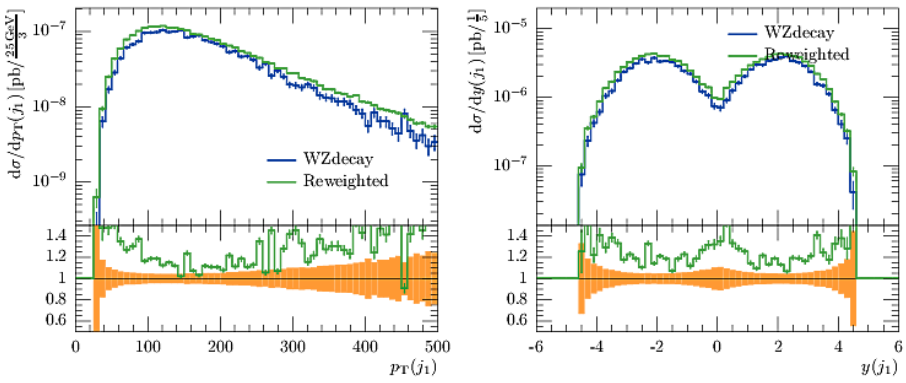

(a) $p_T(j_1)$ **(b)** $y(j_1)$

For further information see beginning of Chapter B

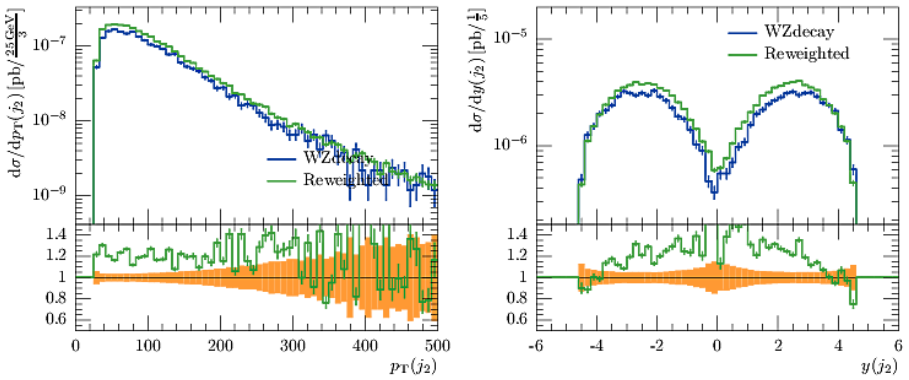

(a) $p_T(j_2)$ **(b)** $y(j_2)$

For further information see beginning of Chapter B

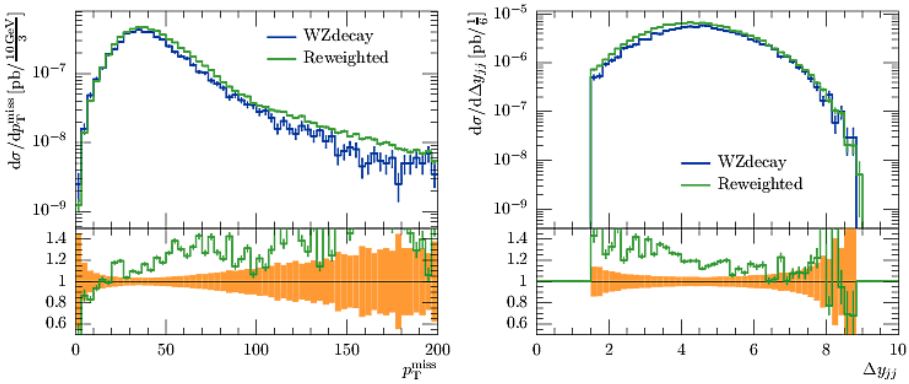

(a) p_T^{miss} **(b)** $\Delta y(jj)$

For further information see beginning of Chapter B

B.2 Events with purely transverse boson polarization

The figures in this section show the distributions of the samples of events with purely transverse boson polarization.

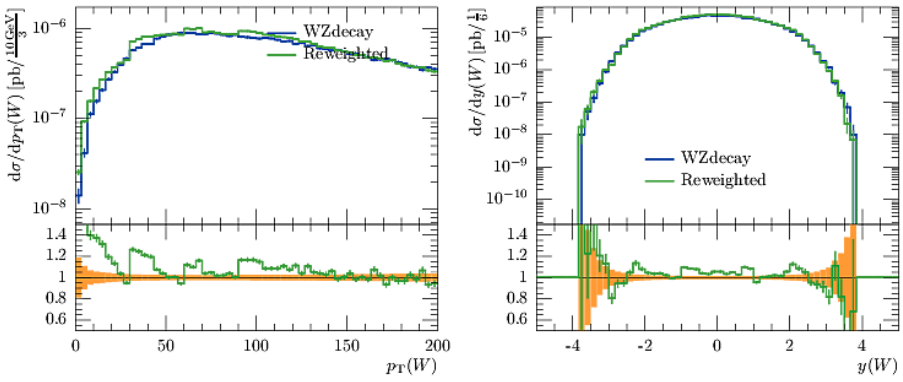

(a) $p_T(W^+)$ **(b)** $y(W^+)$

For further information see beginning of Chapter B

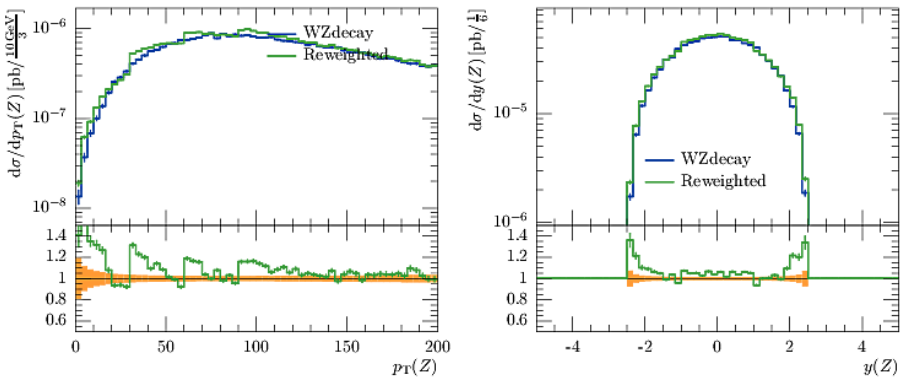

(a) $p_T(Z)$ **(b)** $y(Z)$

For further information see beginning of Chapter B

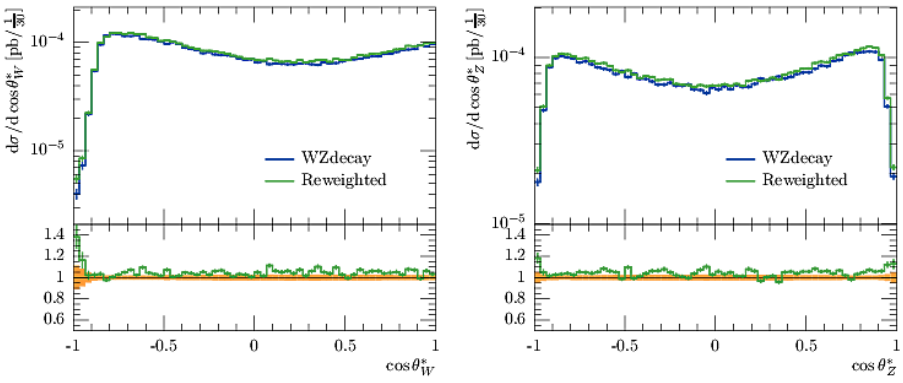

(a) $\cos\theta^*_W$ **(b)** $\cos\theta^*_Z$

For further information see beginning of Chapter B

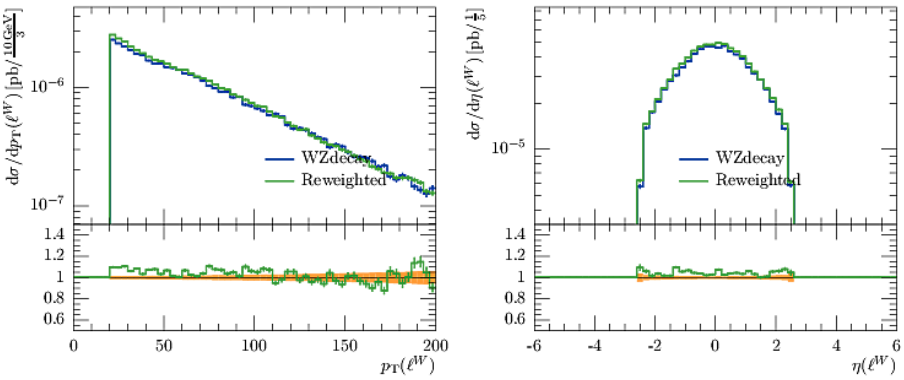

(a) $p_T(\ell^W)$ **(b)** $\eta(\ell^W)$

For further information see beginning of Chapter B

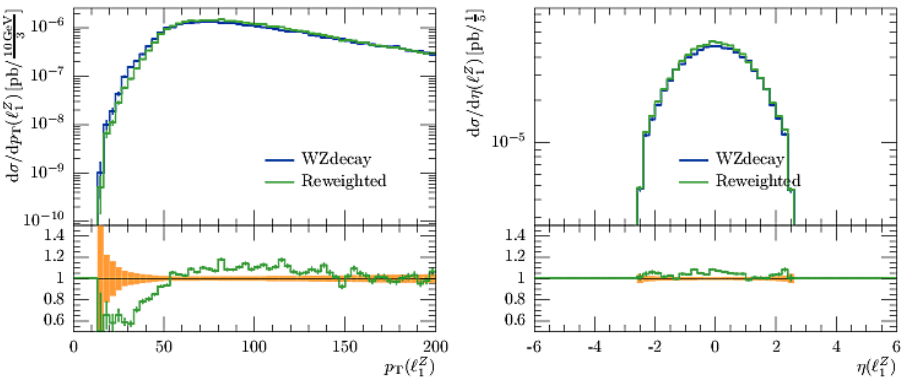

(a) $p_T(\ell^Z_1)$ **(b)** $\eta(\ell^Z_1)$

For further information see beginning of Chapter B

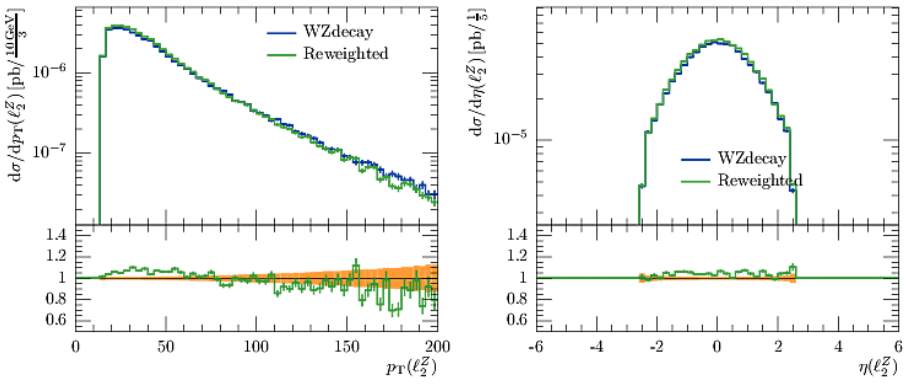

(a) $p_T(\ell_2^Z)$ **(b)** $\eta(\ell_2^Z)$

For further information see beginning of Chapter B

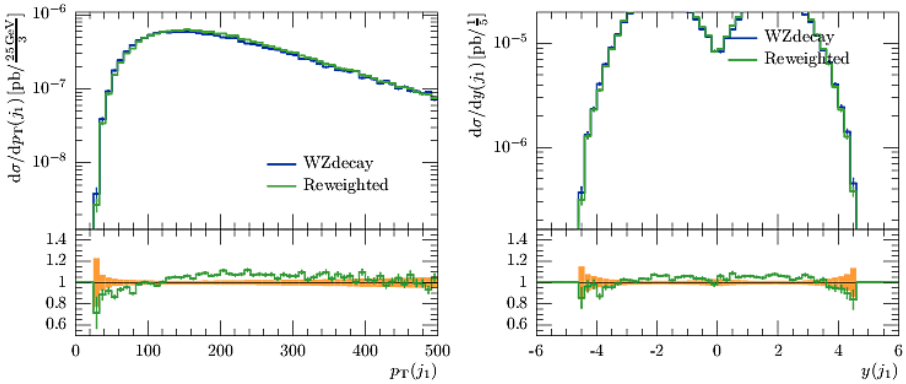

(a) $p_T(j_1)$ **(b)** $y(j_1)$

For further information see beginning of Chapter B

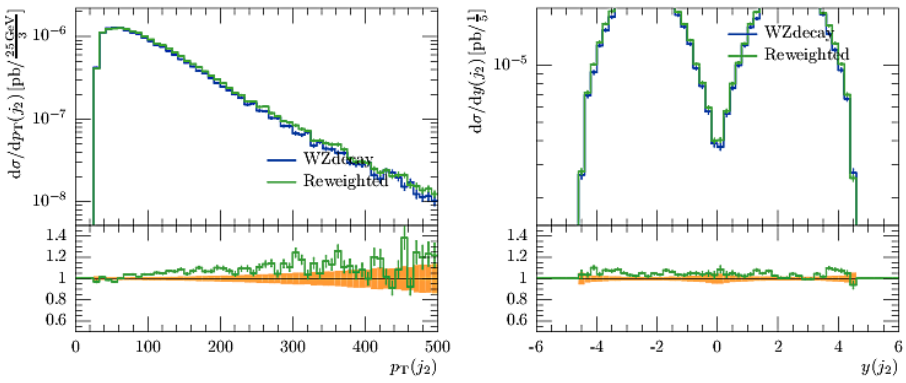

(a) $p_T(j_2)$ **(b)** $y(j_2)$

For further information see beginning of Chapter B

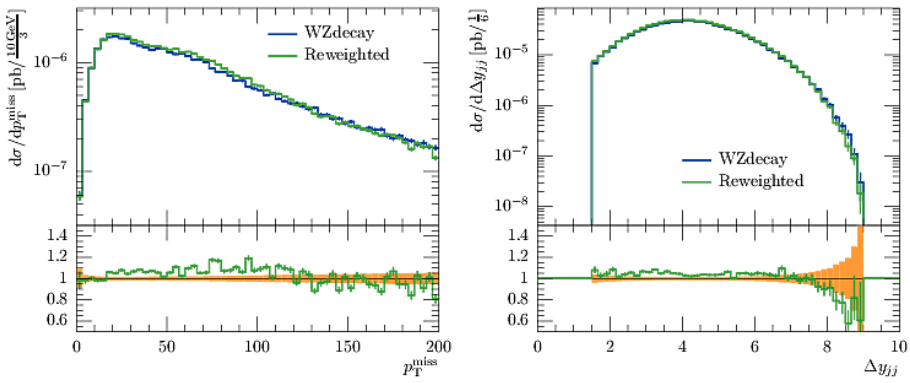

(a) $p_{\mathrm{T}}^{\mathrm{miss}}$ **(b)** $\Delta y(jj)$

For further information see beginning of Chapter B

Appendix C

Fit results

In this chapter figures of the fit results are shown. For each of the studied observables the corresponding figure shows four plots. Each plot contains the four templates (green and blue) and the distribution to which the templates were fitted (orange). The plot on the upper left-handed side shows a comparison of the normalized distributions. The other plots show the normalized stacked templates according to the fractions obtained by the fit, compared to the normalized distribution of the sample to which the fit was applied. In the plot of the upper right-handed side shows the fractions obtained from the fit of the full set of templates, while the plots on the bottom show the fraction from the fits of the combined templates. The plot on the left-handed side shows the combined templates with known polarization of the W^+ boson and on the right-handed side for known polarization of the Z boson.

C.1 Fit to mixed sample

The figures in this section show the results for the fits to the sample with mixed polarization.

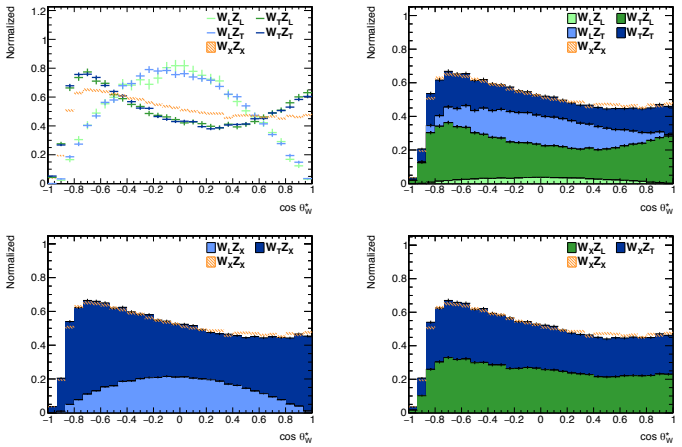

Fit results for $\cos\theta^*_{W^+}$. For more information see beginning of Chapter C on page 93.

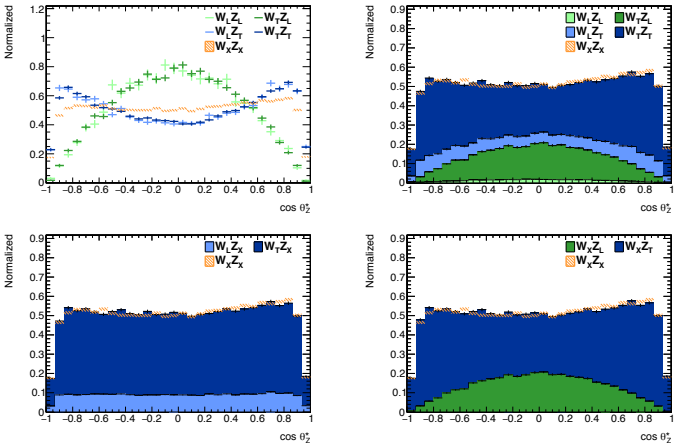

Fit results for $\cos\theta_Z^*$. For more information see beginning of Chapter C on page 93.

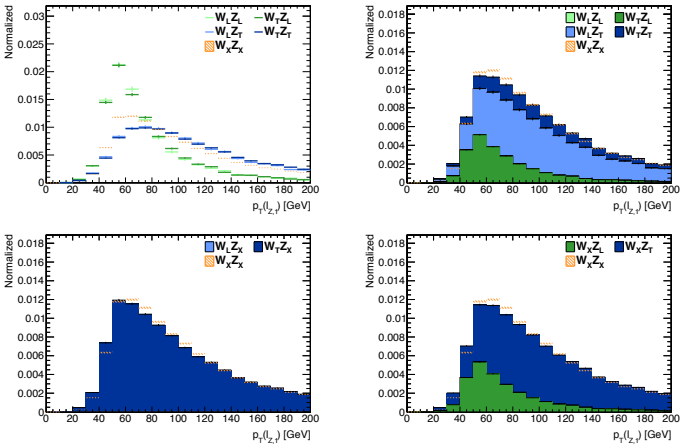

Fit results for $p_{\mathrm{T}}(\ell_1^Z)$. For more information see beginning of Chapter C on page 93.

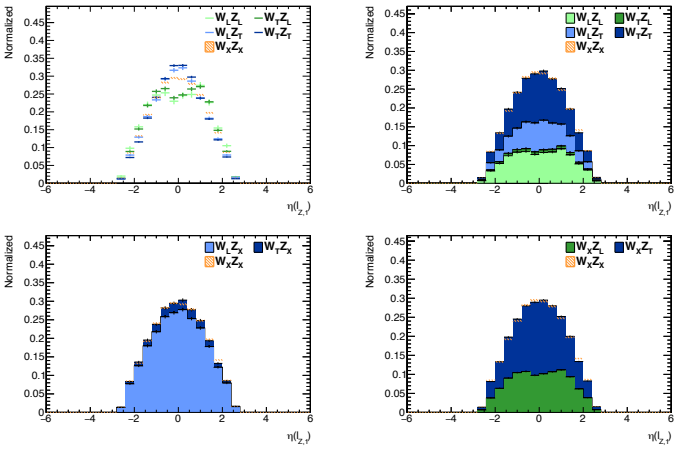

Fit results for $\eta(\ell_1^Z)$. For more information see beginning of Chapter C on page 93.

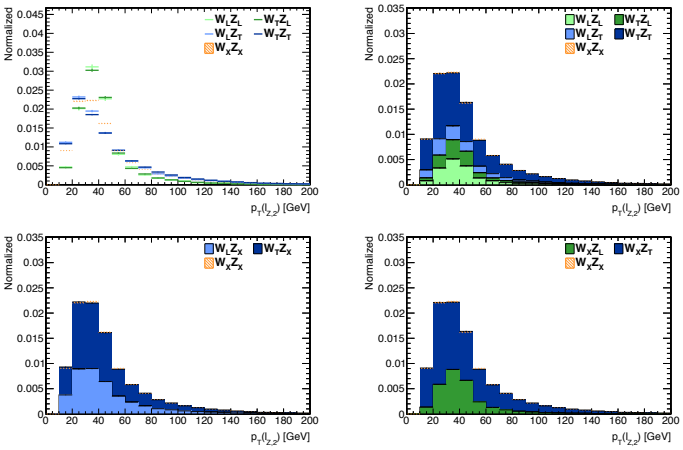

Fit results for $p_{\mathrm{T}}(\ell_2^Z)$. For more information see beginning of Chapter C on page 93.

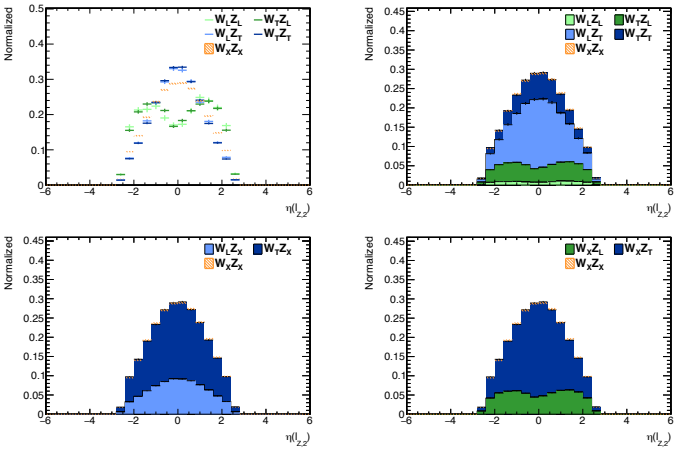

Fit results for $\eta(\ell_2^Z)$. For more information see beginning of Chapter C on page 93.

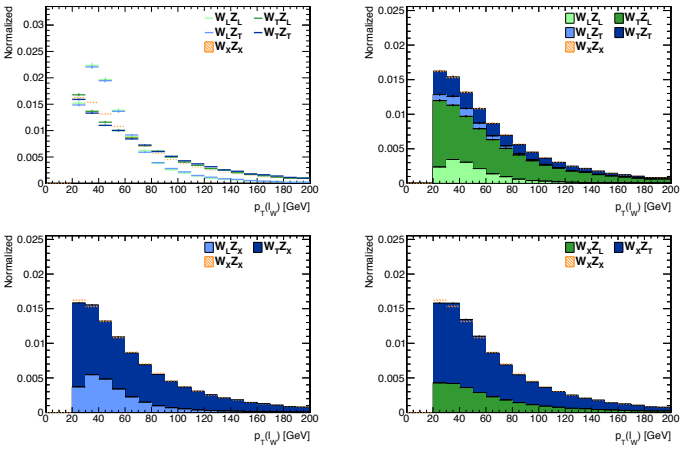

Fit results for $p_{\mathrm{T}}(\ell^W)$. For more information see beginning of Chapter C on page 93.

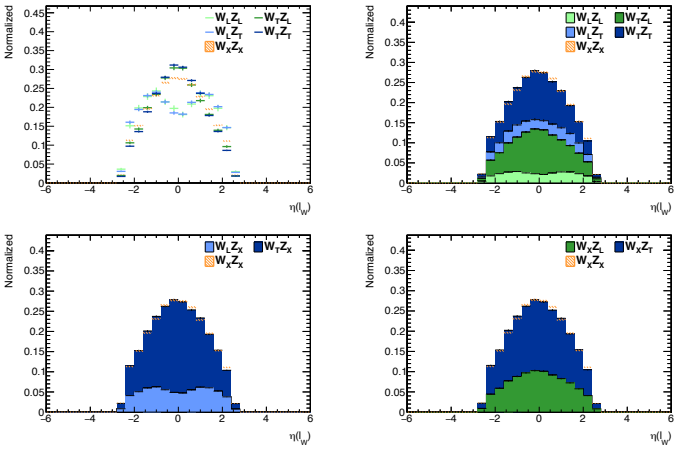

Fit results for $\eta(\ell^W)$. For more information see beginning of Chapter C on page 93.

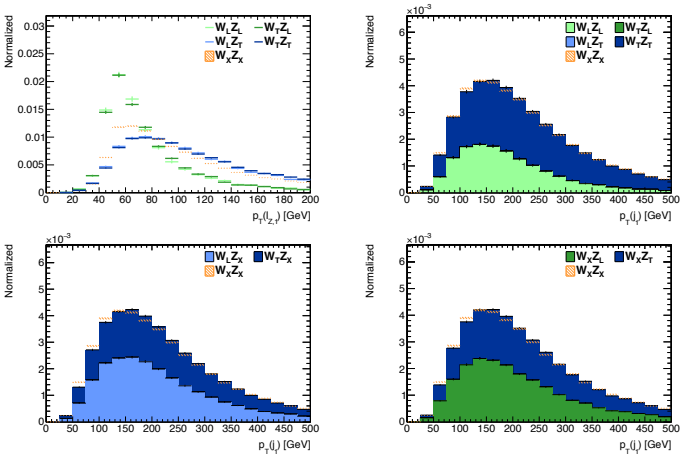

Fit results for $p_{\mathrm{T}}(j_1)$. For more information see beginning of Chapter C on page 93.

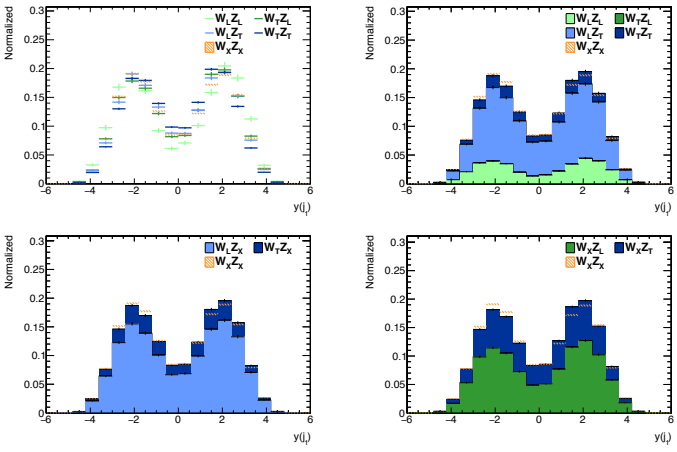

Fit results for $y(j_1)$. For more information see beginning of Chapter C on page 93.

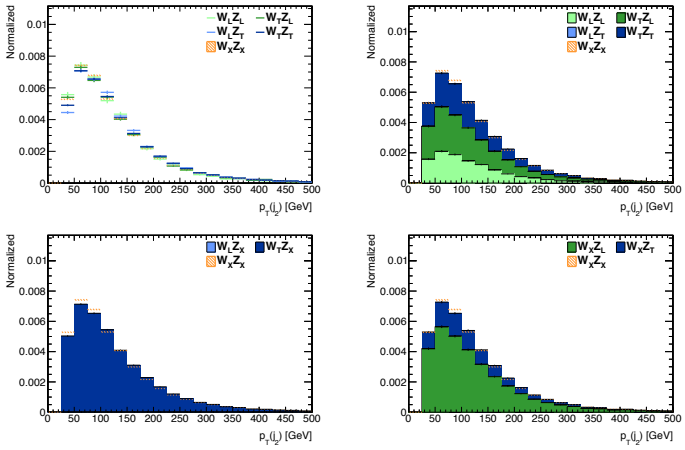

Fit results for $p_T(j_2)$. For more information see beginning of Chapter C on page 93.

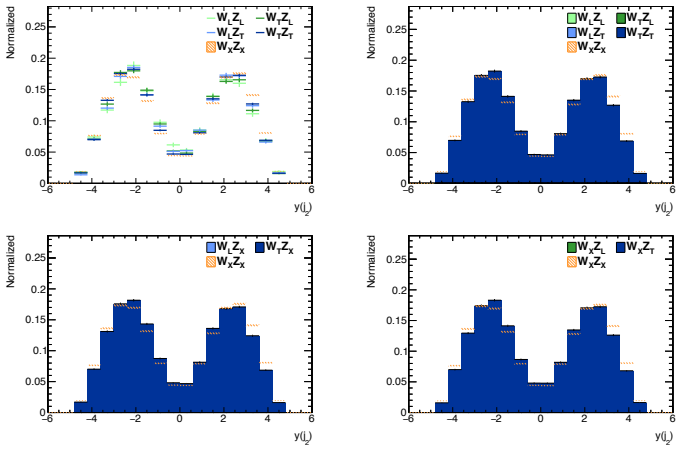

Fit results for $y(j_2)$. For more information see beginning of Chapter C on page 93.

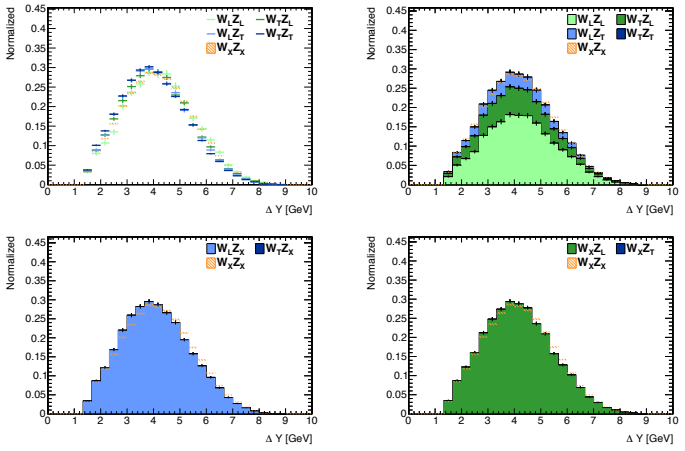

Fit results for Δy_{jj}. For more information see beginning of Chapter C on page 93.

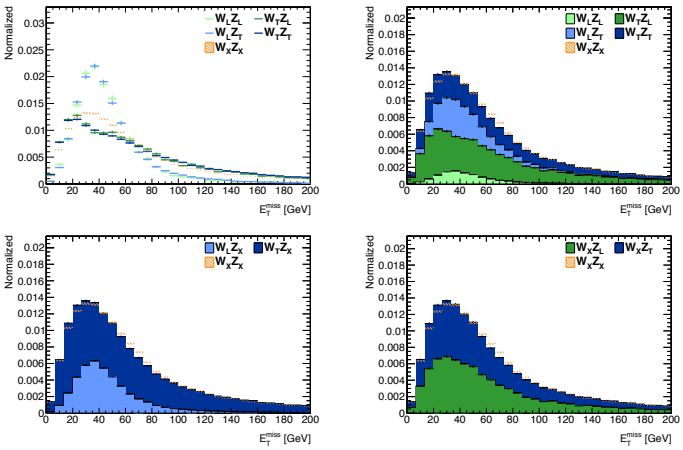

Fit results for $p_{\mathrm{T}}^{\mathrm{miss}}$. For more information see beginning of Chapter C on page 93.

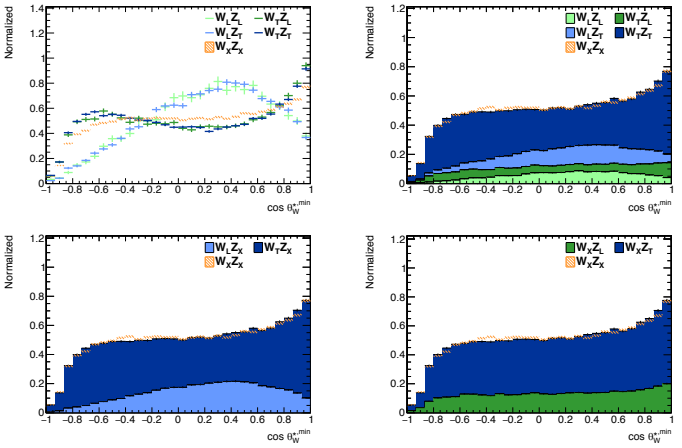

Fit results for $\cos\theta_{W^+}^{*,\,\mathrm{min}}$. For more information see beginning of Chapter C on page 93.

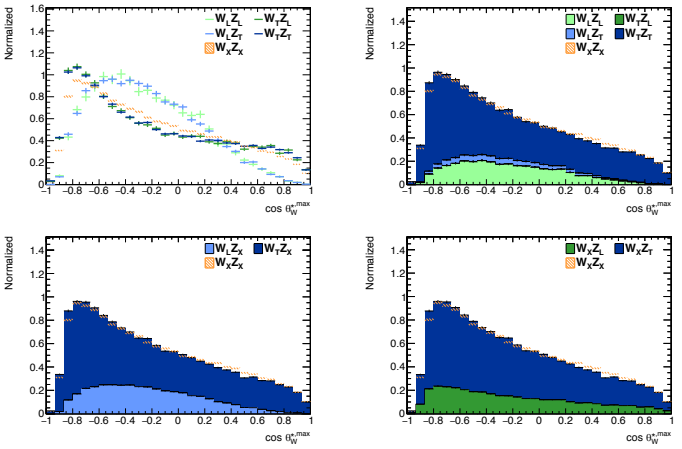

Fit results for $\cos\theta_{W^+}^{*,\,\mathrm{max}}$. For more information see beginning of Chapter C on page 93.

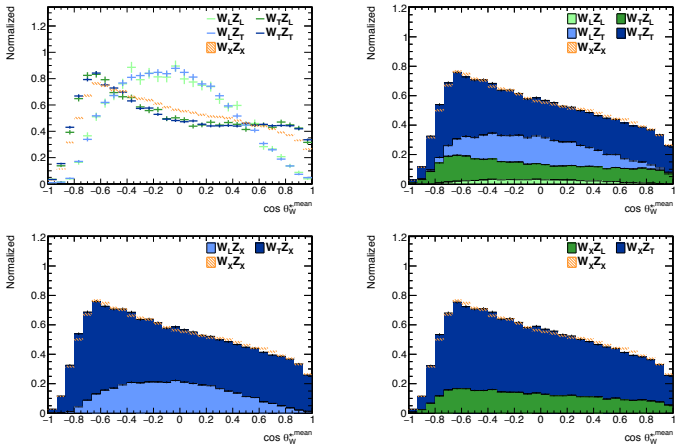

Fit results for $\cos\theta^{*,\,\mathrm{mean}}_{W^+}$. For more information see beginning of Chapter C on page 93.

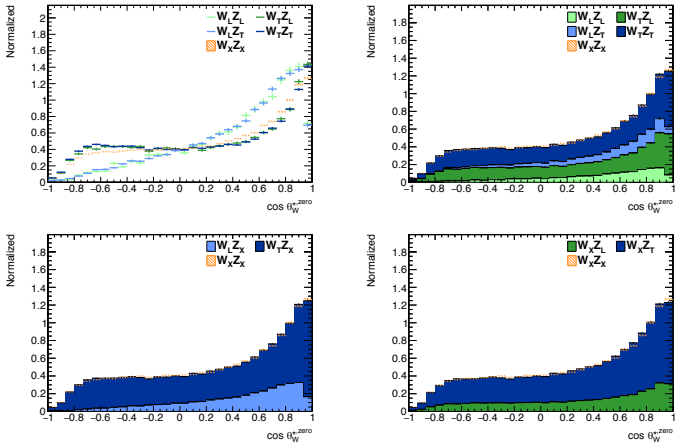

Fit results for $\cos\theta^{*,\,\mathrm{zero}}_{W^+}$. For more information see beginning of Chapter C on page 93.

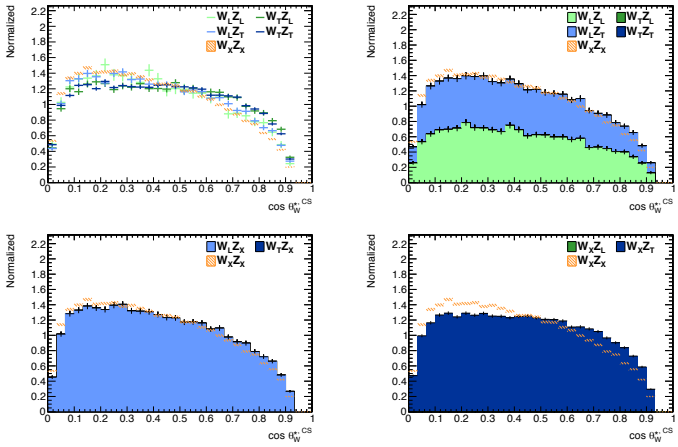

Fit results for $\cos\theta^{*,\,\mathrm{CS}}_{W^+}$. For more information see beginning of Chapter C on page 93.

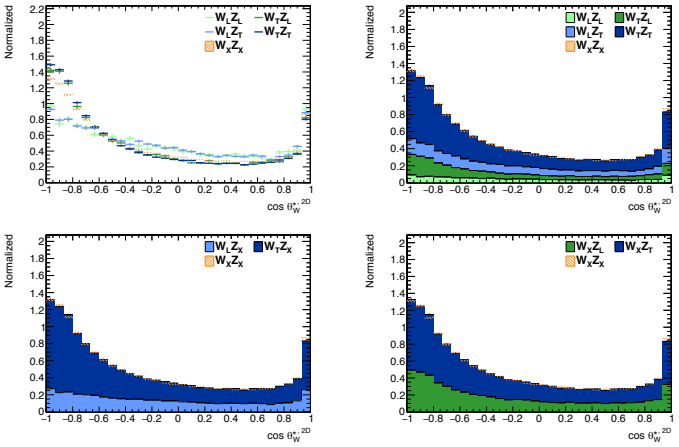

Fit results for $\cos\theta^{*,\,\mathrm{2D}}_{W+}$. For more information see beginning of Chapter C on page 93.

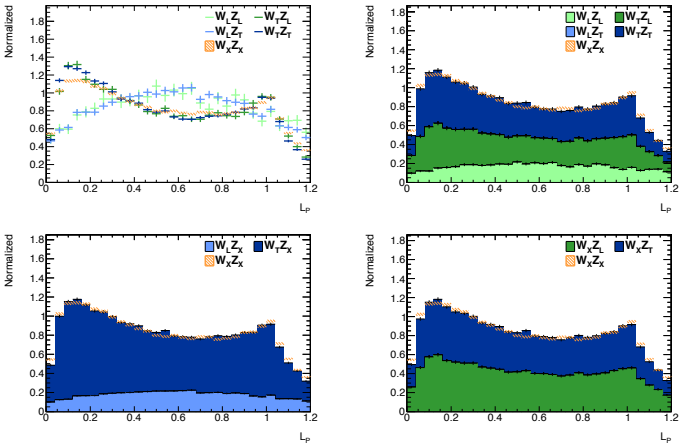

Fit results for L_P. For more information see beginning of Chapter C on page 93.

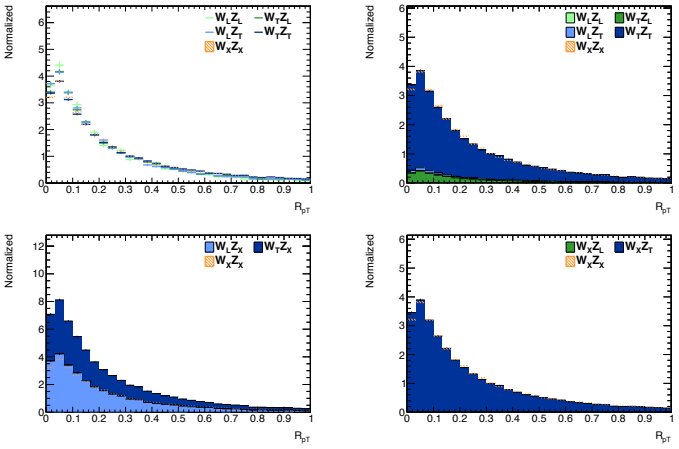

Fit results for R_{p_T}. For more information see beginning of Chapter C on page 93.

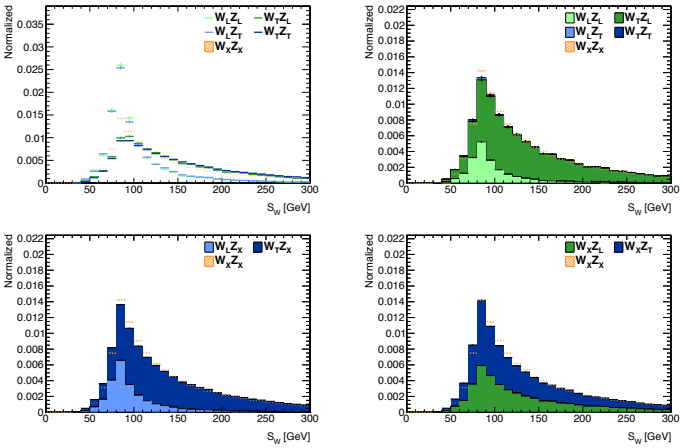

Fit results for S_W. For more information see beginning of Chapter C on page 93.

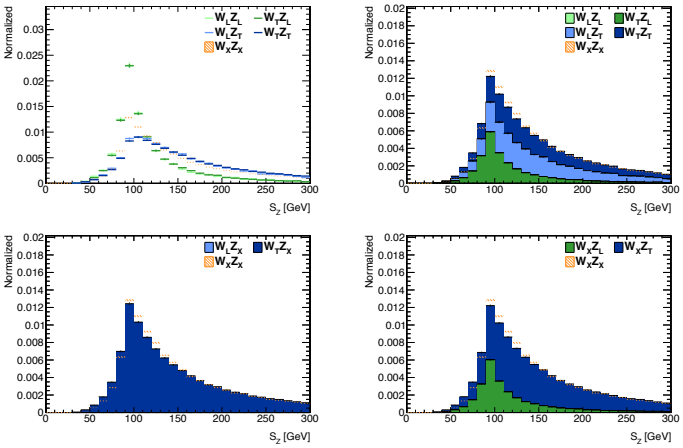

Fit results for S_Z. For more information see beginning of Chapter C on page 93.

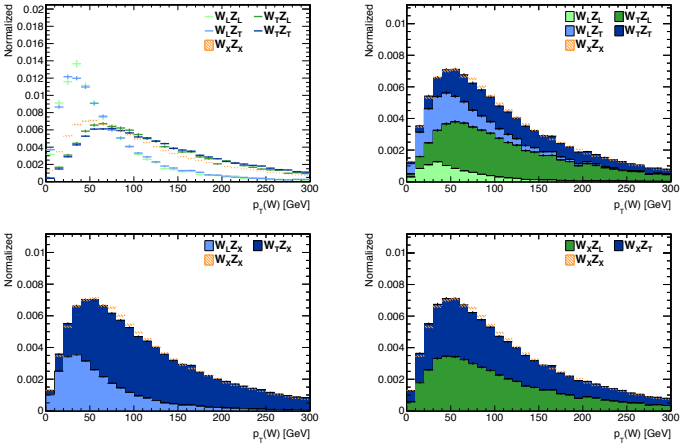

Fit results for $p_{\mathrm{T}}(W^+)$. For more information see beginning of Chapter C on page 93.

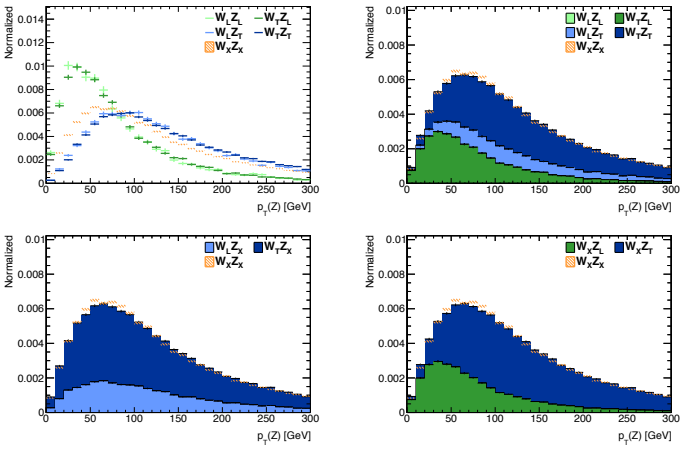

Fit results for $p_{\mathrm{T}}(Z)$. For more information see beginning of Chapter C on page 93.

C.2 Fit to purely transverse sample

The figures in this section show the results for the fits to the sample with purely transverse boson polarization.

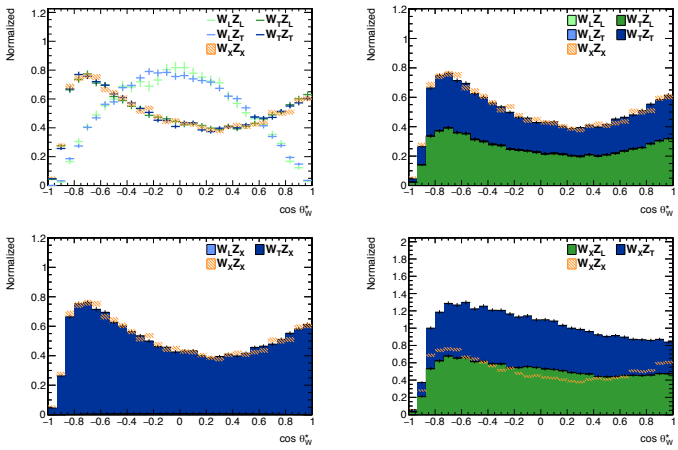

Fit results for $\cos\theta^*_{W+}$. For more information see beginning of Chapter C.2 on page 103.

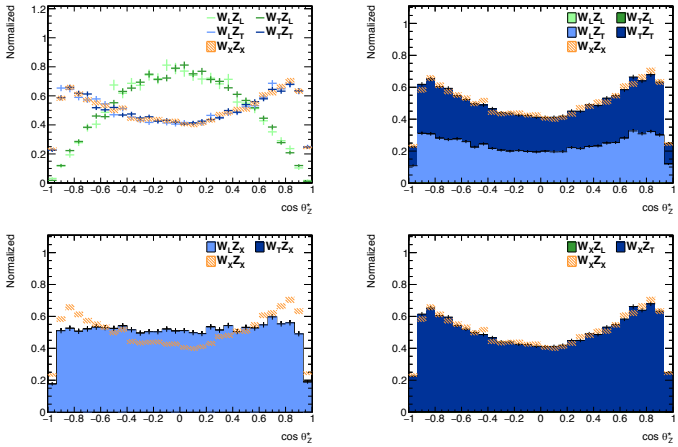

Fit results for $\cos\theta^*_Z$. For more information see beginning of Chapter C.2 on page 103.

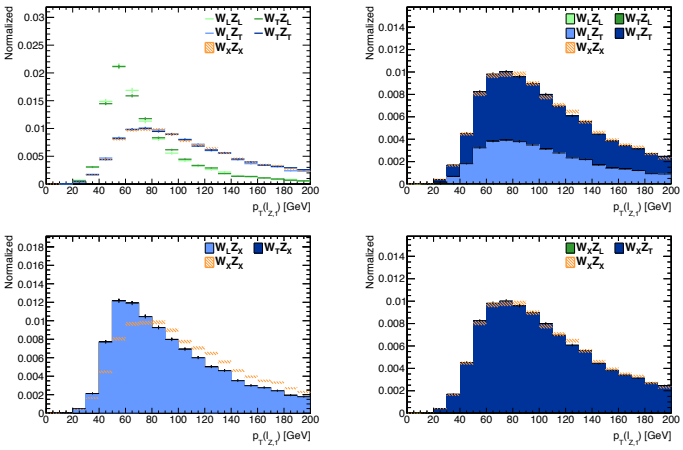

Fit results for $p_{\mathrm{T}}(\ell_1^Z)$. For more information see beginning of Chapter C.2 on page 103.

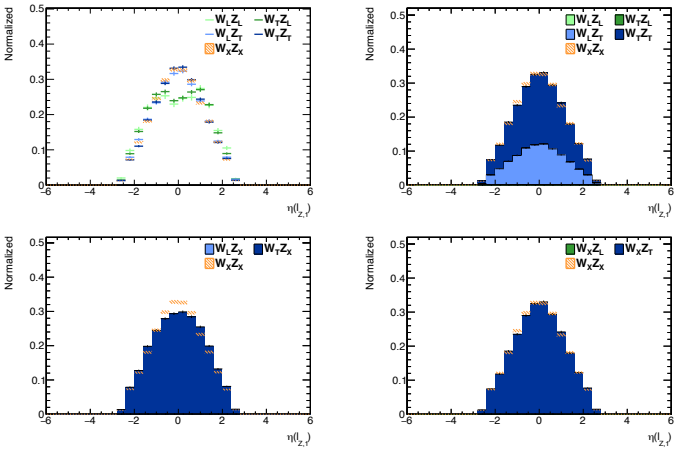

Fit results for $\eta(\ell_1^Z)$. For more information see beginning of Chapter C.2 on page 103.

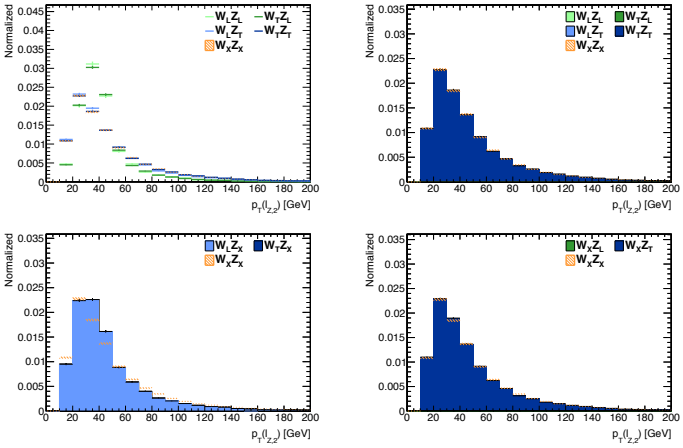

Fit results for $p_{\mathrm{T}}(\ell_2^Z)$. For more information see beginning of Chapter C.2 on page 103.

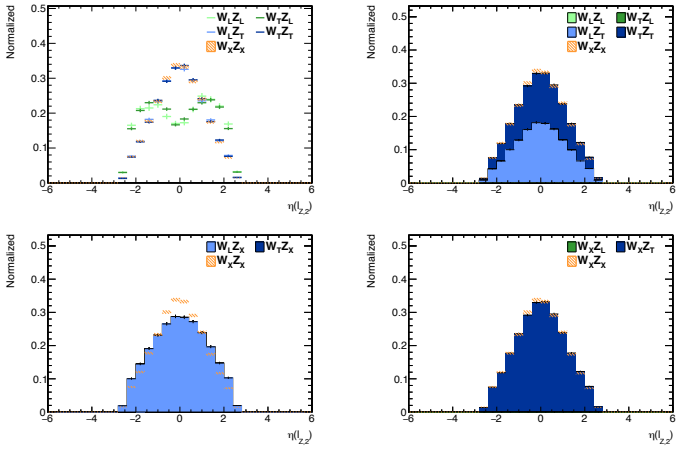

Fit results for $\eta(\ell_2^Z)$. For more information see beginning of Chapter C.2 on page 103.

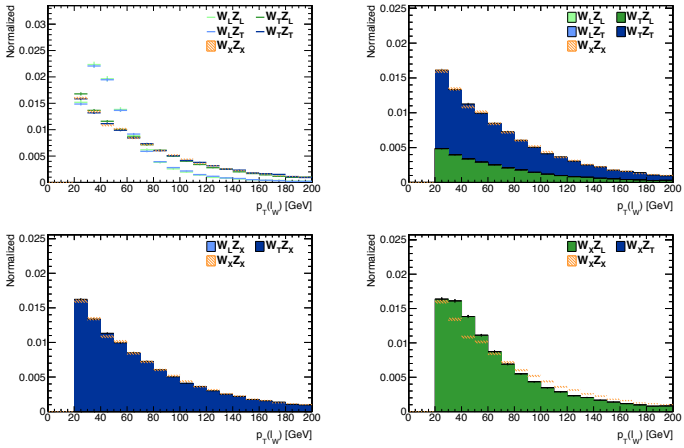

Fit results for $p_{\mathrm{T}}(\ell^W)$. For more information see beginning of Chapter C.2 on page 103.

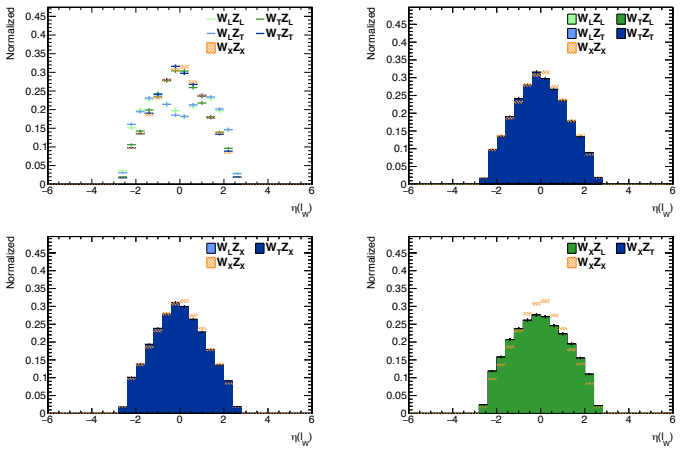

Fit results for $\eta(\ell^W)$. For more information see beginning of Chapter C.2 on page 103.

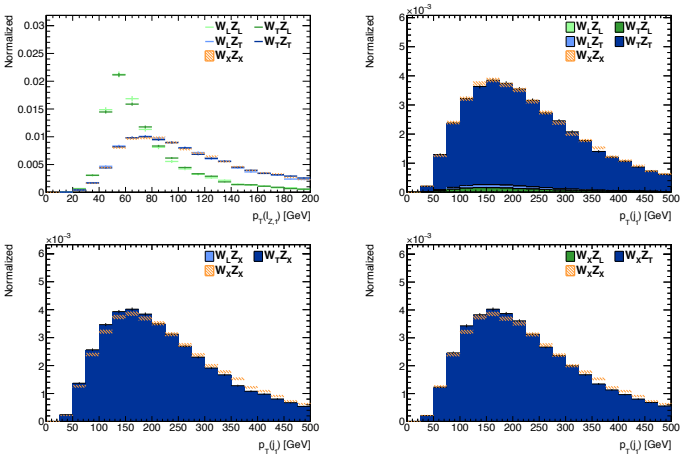

Fit results for $p_T(j_1)$. For more information see beginning of Chapter C.2 on page 103.

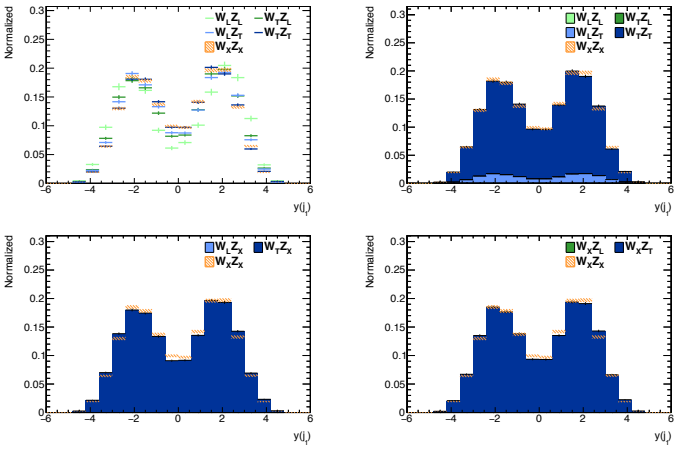

Fit results for $y(j_1)$. For more information see beginning of Chapter C.2 on page 103.

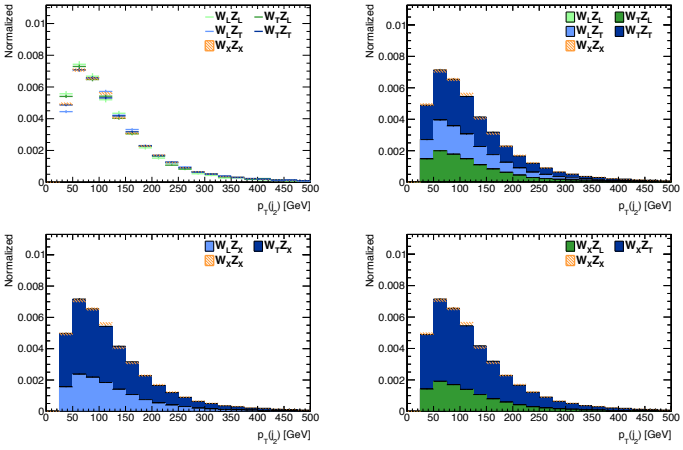

Fit results for $p_T(j_2)$. For more information see beginning of Chapter C.2 on page 103.

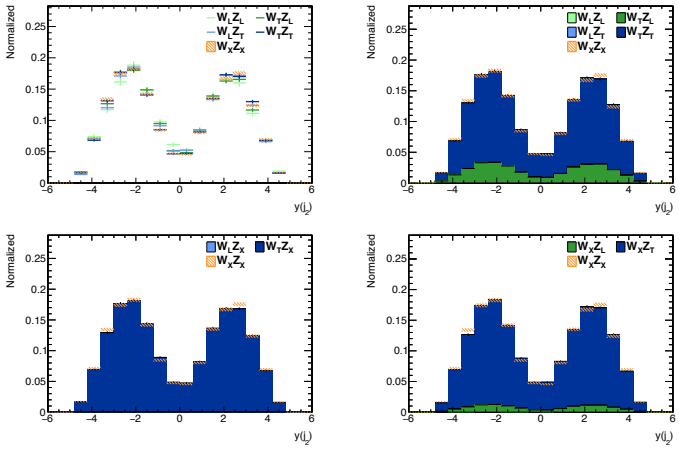

Fit results for $y(j_2)$. For more information see beginning of Chapter C.2 on page 103.

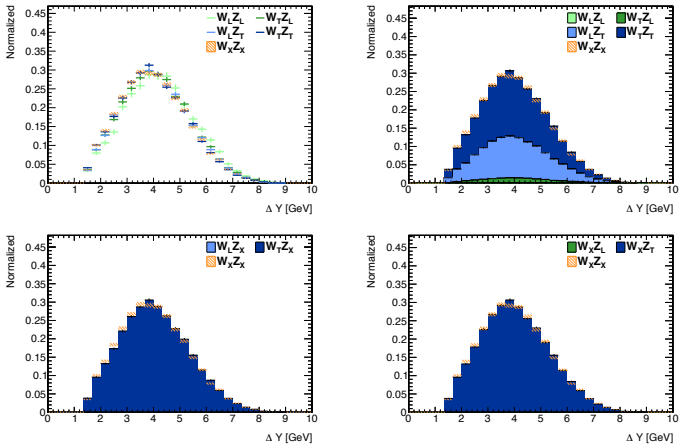

Fit results for Δy_{jj}. For more information see beginning of Chapter C.2 on page 103.

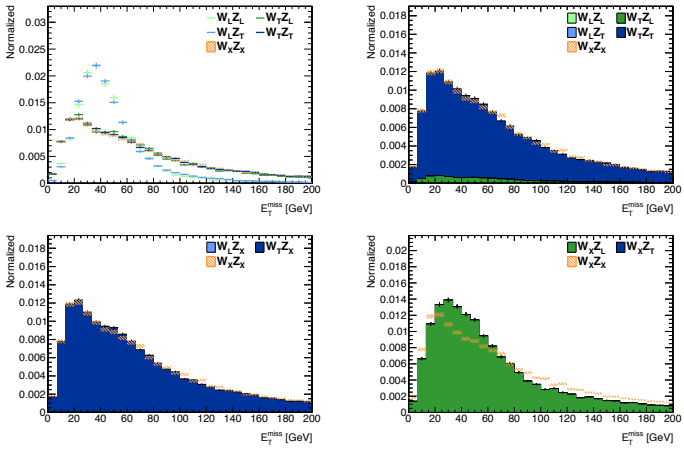

Fit results for $p_{\mathrm{T}}^{\mathrm{miss}}$. For more information see beginning of Chapter C.2 on page 103.

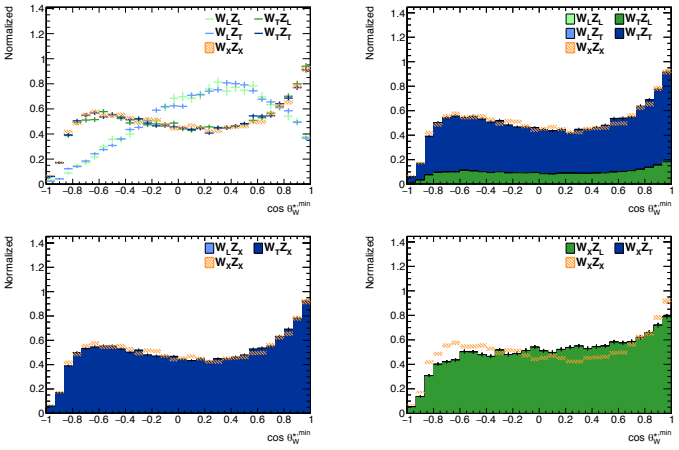

Fit results for $\cos\theta^{*,\,\text{min}}_{W^+}$. For more information see beginning of Chapter C.2 on page 103.

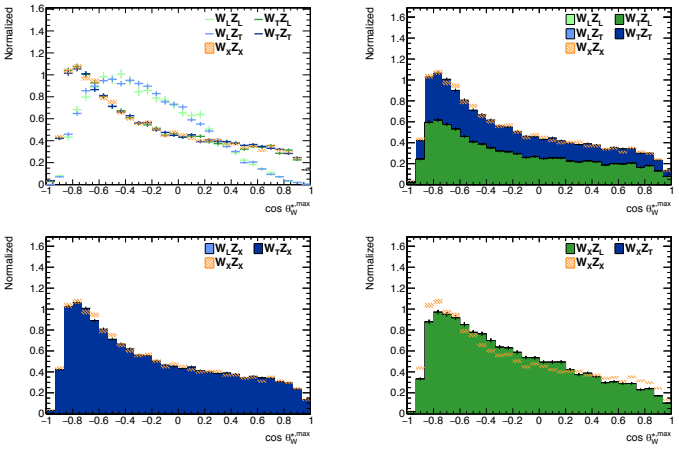

Fit results for $\cos\theta^{*,\,\text{max}}_{W^+}$. For more information see beginning of Chapter C.2 on page 103.

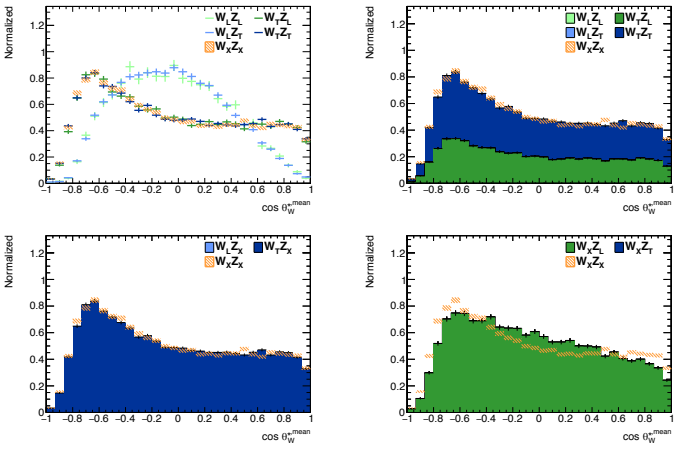

Fit results for $\cos\theta^{*,\,\text{mean}}_{W^+}$. For more information see beginning of Chapter C.2 on page 103.

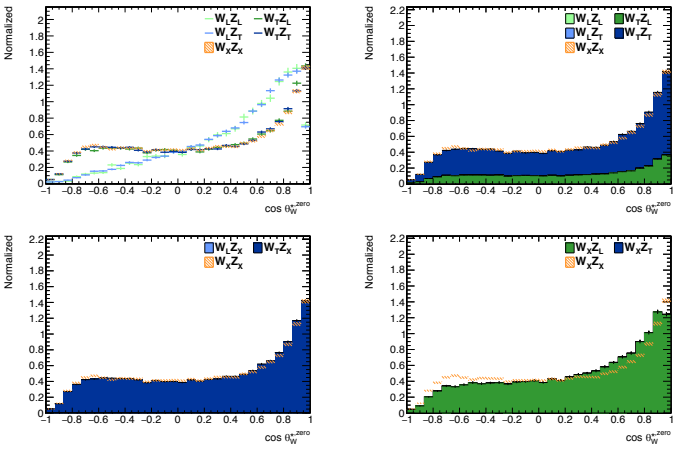

Fit results for $\cos\theta^{*,\,\mathrm{zero}}_{W^+}$. For more information see beginning of Chapter C.2 on page 103.

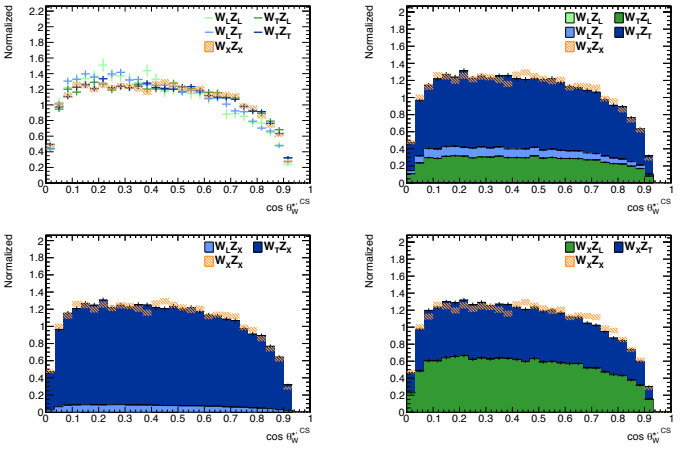

Fit results for $\cos\theta^{*,\,\mathrm{CS}}_{W^+}$. For more information see beginning of Chapter C.2 on page 103.

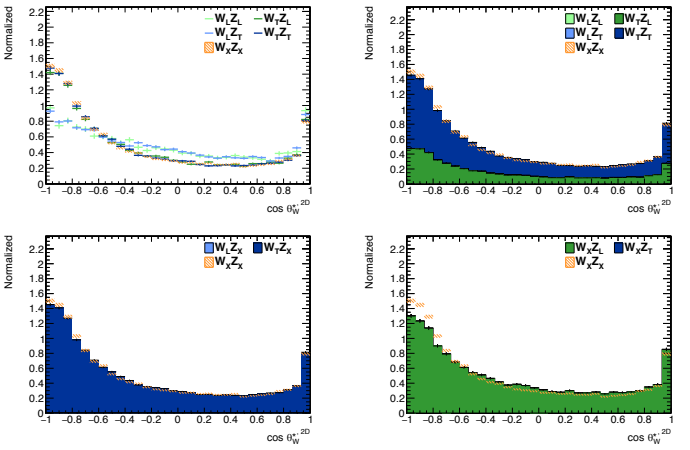

Fit results for $\cos\theta^{*,\,\mathrm{2D}}_{W^+}$. For more information see beginning of Chapter C.2 on page 103.

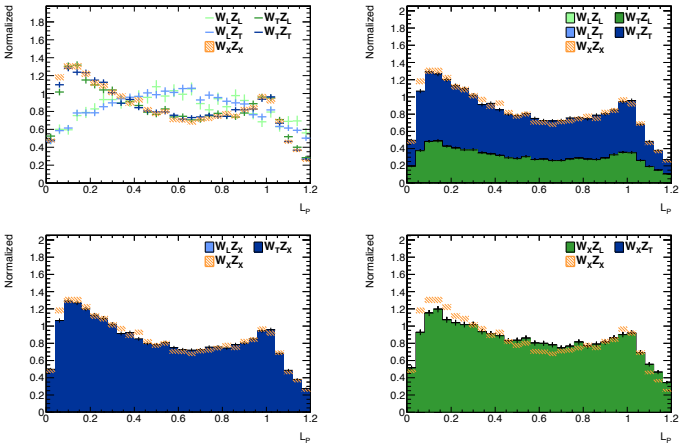

Fit results for L_P. For more information see beginning of Chapter C.2 on page 103.

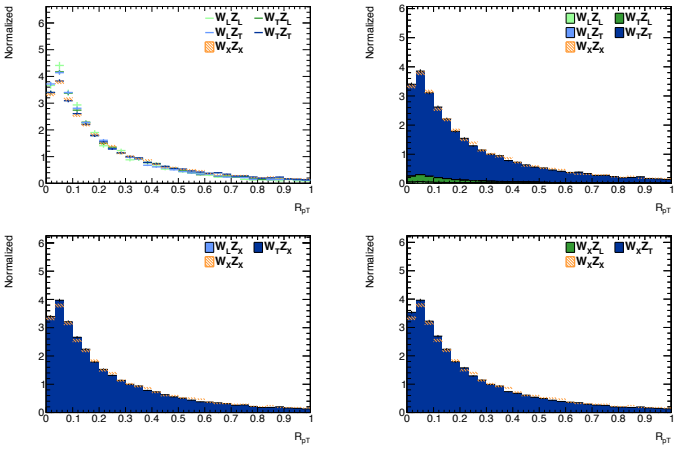

Fit results for $R_{p\mathrm{T}}$. For more information see beginning of Chapter C.2 on page 103.

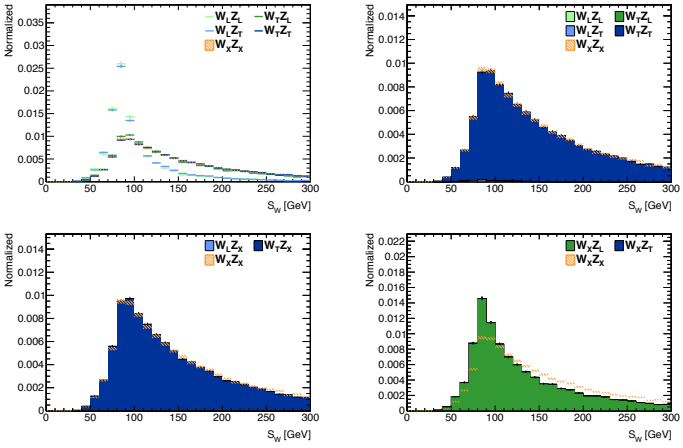

Fit results for S_W. For more information see beginning of Chapter C.2 on page 103.

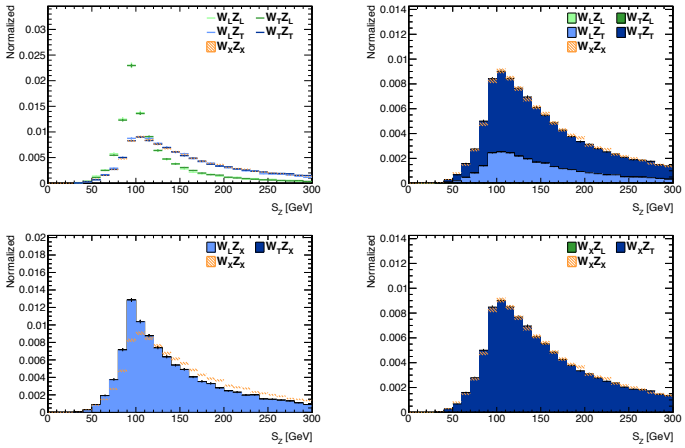

Fit results for S_Z. For more information see beginning of Chapter C.2 on page 103.

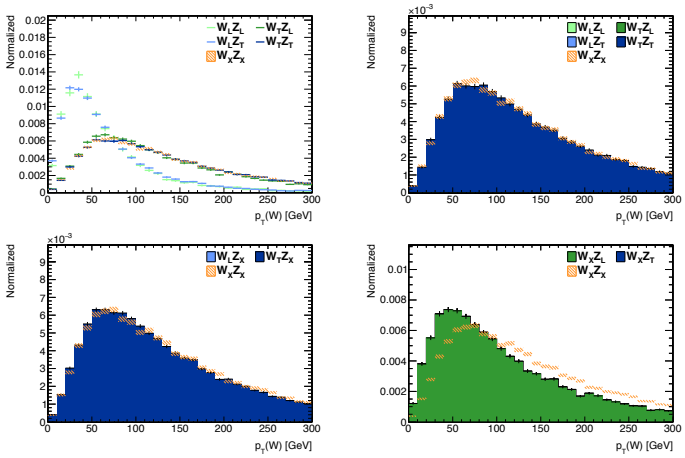

Fit results for $p_{\mathrm{T}}(W^+)$. For more information see beginning of Chapter C.2 on page 103.

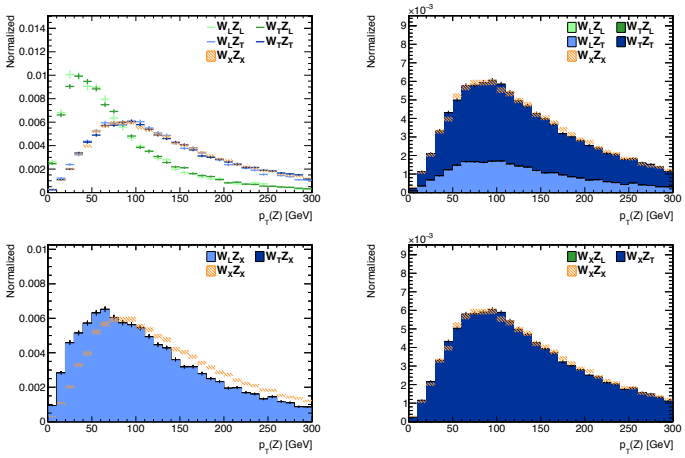

Fit results for $p_{\mathrm{T}}(Z)$. For more information see beginning of Chapter C.2 on page 103.

Appendix D

Additional Plots and Tables

D.1 Polarization changes during scattering

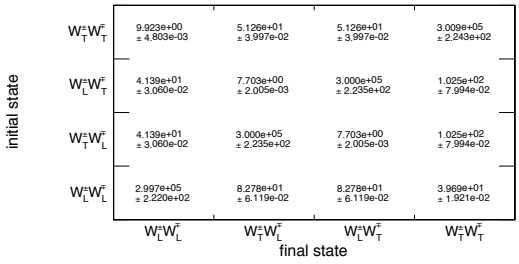

(a) $W^\pm W^\mp \to W^\pm W^\mp$

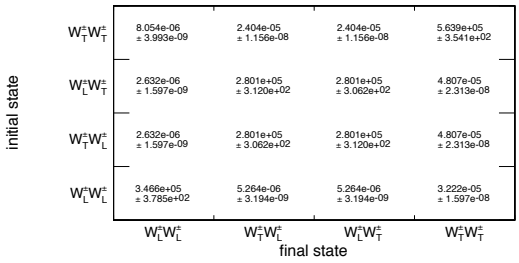

(b) $W^\pm W^\pm \to W^\pm W^\pm$

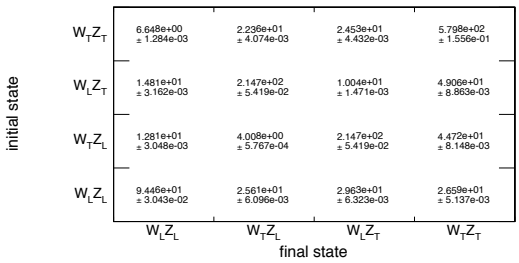

(c) $W^\pm Z \to W^\pm Z$

Figure D.1: The cross section for all helicity combinations in the scattering of the different boson combinations. On the x- (y)-axis all combinations for the final (initial) state bosons are plotted. The cross section σ in pb and its uncertainty are printed in each bin.

D.2 Distributions in p_T-y plane

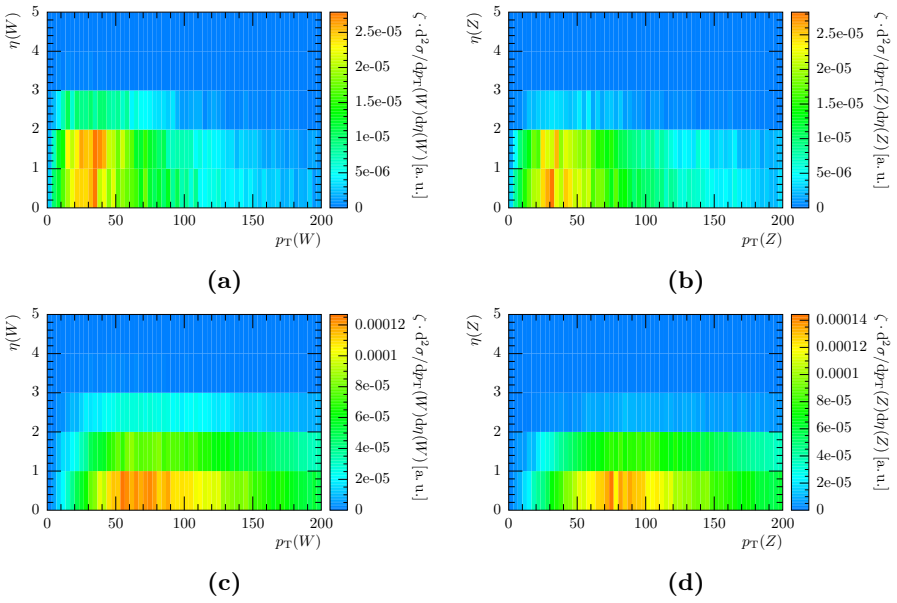

Figure D.2: Distribution of differential cross section in bins of transverse momentum and rapidity of the W^+ (left) or Z (right) boson. In the upper row the distributions of the events with purely longitudinal boson polarization and in the bottom row of the events with purely transverse polarization are shown.

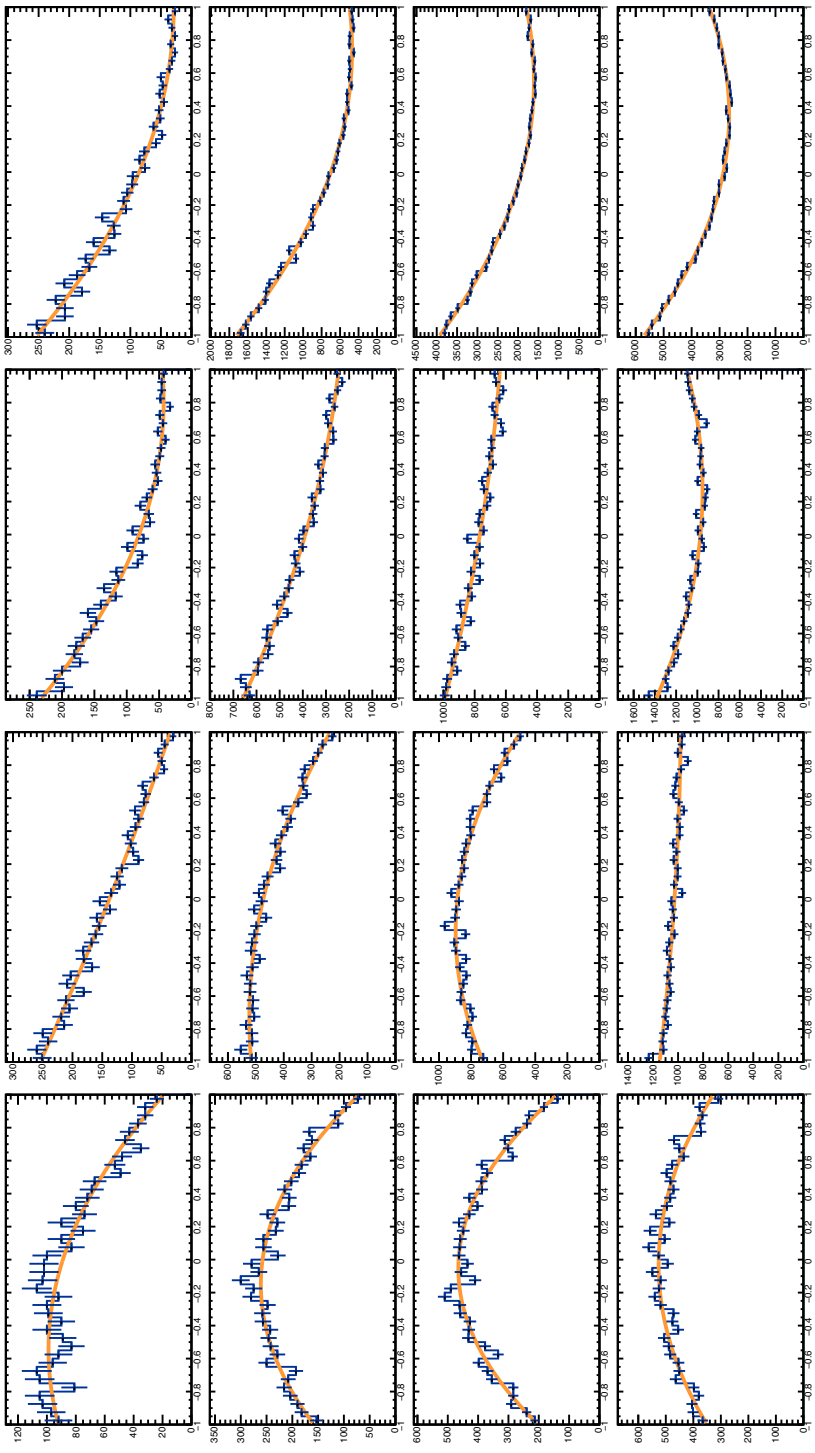

Figure D.3: Visualization of the histogram in the transverse momentum, the absolute value of the rapidity, and the cosine of the decay angle of the W^+ boson of the sample used as input for the reweighting approach. The columns correspond to different bins in the transverse momentum (first column: $p_{\mathrm{T}}(W^+) < 30$ GeV, second column: $30\ \mathrm{GeV} < p_{\mathrm{T}}(W^+) < 60$ GeV, third column: $60\ \mathrm{GeV} < p_{\mathrm{T}}(W^+) < 90$ GeV, fourth column: $p_{\mathrm{T}}(W^+) > 90$ GeV). The rows correspond to different bins of the absolute value of the rapidity (first row: $y(W^+) > 4$, second row: $2 < y(W^+) < 3$, third row: $1 < y(W^+) < 2$, fourth row: $y(W^+) < 1$). In each plot the distribution of the cosine of the decay angle (blue) and theoretical prediction with fitted helicity fractions (orange) are shown.

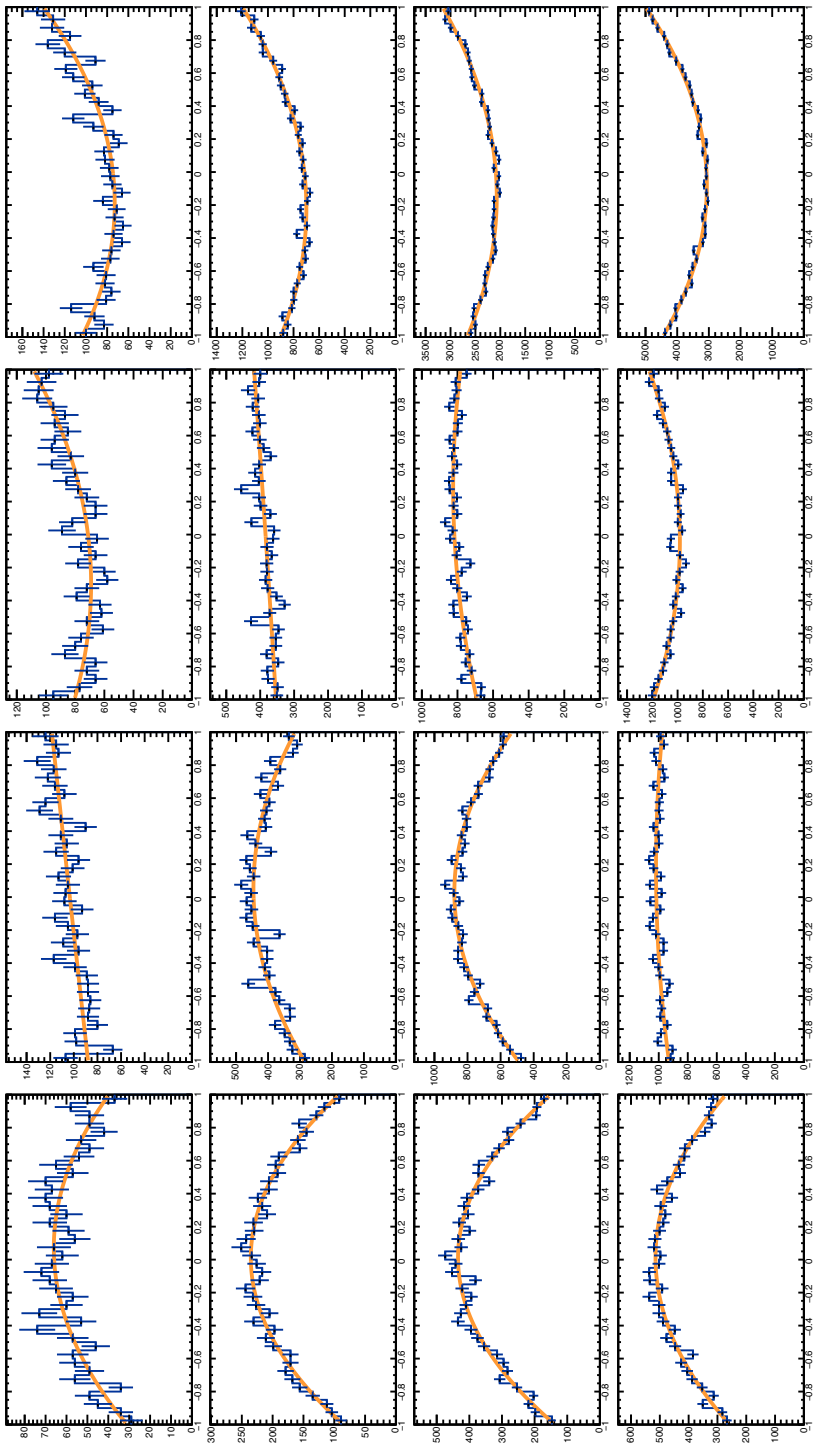

Figure D.4: Visualization of the histogram in the transverse momentum, the absolute value of the rapidity, and the cosine of the decay angle of the Z boson of the sample used as input for the reweighting approach. The columns correspond to different bins in the transverse momentum (first column: $p_{\mathrm{T}}(Z) < 30$ GeV, second column: 30 GeV $< p_{\mathrm{T}}(Z) < 60$ GeV, third column: 60 GeV $< p_{\mathrm{T}}(Z) < 90$ GeV, fourth column: $p_{\mathrm{T}}(Z) > 90$ GeV). The rows correspond to different bins of the absolute value of the rapidity (first row: $y(Z) > 4$, second row: $2 < y(Z) < 3$, third row: $1 < y(Z) < 2$, fourth row: $y(Z) < 1$). In each plot the distribution of the cosine of the decay angle (blue) and theoretical prediction with fitted helicity fractions (orange) are shown.

List of Figures

List of Tables

Bibliography

[1] J. J. Thomson, *Cathode rays*, Philosophical Magazine Series 5. **44** no. 269, (1897) 293–316. http://www.tandfonline.com/doi/abs/10.1080/14786449708621070#.

[2] E. Rutherford, *Nuclear Constitution of Atoms*, Proceedings of the Royal Society**97** 374–400.

[3] J. Chadwick, *Possible Existence of a Neutron*, Nature **129** no. 3252, (1932) 312–312.

[4] ATLAS Collaboration, G. Aad et al, *Observation of a new particle in the search for the Standard Model Higgs boson with the ATLAS detector at the LHC*, Physics Letters B **716** no. 1, (2012) 1 – 29, arXiv:1207.7214 [hep-ex]. http://www.sciencedirect.com/science/article/pii/S037026931200857X.

[5] CMS Collaboration, S. Chatrchyan et al, *Observation of a new boson at a mass of 125 GeV with the CMS experiment at the LHC*, Physics Letters B **716** no. 1, (2012) 30 – 61, arXiv:1207.7235 [hep-ex]. http://www.sciencedirect.com/science/article/pii/S0370269312008581.

[6] S. P. Martin, *A Supersymmetry Primer*, tech. rep., Sept., 1997.

[7] ATLAS Collaboration, G. Aad et al, *Evidence for Electroweak Production of $W^{\pm}W^{\pm}jj$ in pp Collisions at $\sqrt{s} = 8$ TeV with the ATLAS Detector*, Phys. Rev. Lett. **113** (2014) 141803, arXiv:1405.6241 [hep-ex]. http://link.aps.org/doi/10.1103/PhysRevLett.113.141803.

[8] D. J. Griffiths, *Introduction to elementary particles; 2nd rev. version*. Physics textbook. Wiley, New York, NY, 2008.

[9] M. Thomson, *Modern particle physics*. Cambridge University Press, 2013.

[10] E. Noether, *Invariante Variationsprobleme*, Nachrichten von der Gesellschaft der Wissenschaften zu Göttingen, Mathematisch-Physikalische Klasse **1918** (1918) 235–257. http://eudml.org/doc/59024.

[11] J. Beringer et al (Particle Data Group), *The Review of Particle Physics*, Physical Review D **86** (2012) 010001.

[12] ATLAS, CMS Collaboration, *Combined Measurement of the Higgs Boson Mass in pp Collisions at $\sqrt{s} = 7$ and 8 TeV with the ATLAS and CMS Experiments*, arXiv:1503.07589 [hep-ex].

[13] K. Nakamura and P. D. Group, *Review of Particle Physics*, Journal of Physics G: Nuclear and Particle Physics **37** no. 7A, (2010) 075021. http://stacks.iop.org/0954-3899/37/i=7A/a=075021.

[14] H. D. Politzer, *Reliable Perturbative Results for Strong Interactions?*, Phys. Rev. Lett. **30** (1973) 1346–1349. http://link.aps.org/doi/10.1103/PhysRevLett.30.1346.

[15] H. D. Politzer, *Asymptotic freedom: An approach to strong interactions*, Physics Reports **14** no. 4, (1974) 129 – 180. http://www.sciencedirect.com/science/article/pii/0370157374900143.

[16] D. J. Gross and F. Wilczek, *Asymptotically Free Gauge Theories. I*, Phys. Rev. D **8** (1973) 3633–3652. http://link.aps.org/doi/10.1103/PhysRevD.8.3633.

[17] S. L. Glashow, *Partial-symmetries of weak interactions*, Nuclear Physics **22** no. 4, (1961) 579 – 588. http://www.sciencedirect.com/science/article/pii/0029558261904692.

[18] A. Salam and J. Ward, *Weak and electromagnetic interactions*, Il Nuovo Cimento Series 10 **11** no. 4, (1959) 568–577. http://dx.doi.org/10.1007/BF02726525.

[19] S. Weinberg, *A Model of Leptons*, Phys. Rev. Lett. **19** (1967) 1264–1266. http://link.aps.org/doi/10.1103/PhysRevLett.19.1264.

[20] F. Englert and R. Brout, *Broken Symmetry and the Mass of Gauge Vector Mesons*, Phys. Rev. Lett. **13** (1964) 321–323. http://link.aps.org/doi/10.1103/PhysRevLett.13.321.

[21] P. Higgs, *Broken symmetries, massless particles and gauge fields*, Physics Letters **12** no. 2, (1964) 132 – 133. http://www.sciencedirect.com/science/article/pii/0031916364911369.

[22] P. W. Higgs, *Spontaneous Symmetry Breakdown without Massless Bosons*, Phys. Rev. **145** (1966) 1156–1163. http://link.aps.org/doi/10.1103/PhysRev.145.1156.

[23] P. W. Higgs, *Broken Symmetries and the Masses of Gauge Bosons*, Phys. Rev. Lett. **13** (1964) 508–509. http://link.aps.org/doi/10.1103/PhysRevLett.13.508.

[24] G. S. Guralnik, C. R. Hagen, and T. W. B. Kibble, *Global Conservation Laws and Massless Particles*, Phys. Rev. Lett. **13** (1964) 585–587. http://link.aps.org/doi/10.1103/PhysRevLett.13.585.

[25] Y. Nambu, *Quasi-Particles and Gauge Invariance in the Theory of Superconductivity*, Phys. Rev. **117** (1960) 648–663. http://link.aps.org/doi/10.1103/PhysRev.117.648.

[26] J. Goldstone, A. Salam, and S. Weinberg, *Broken Symmetries*, Phys. Rev. **127** (1962) 965–970. http://link.aps.org/doi/10.1103/PhysRev.127.965.

[27] A. Pich, *Aspects of quantum chromodynamics*, arXiv:0001118 [hep-ph].

[28] L. Evans and P. Bryant, *LHC Machine*, Journal of Instrumentation **3** no. 08, (2008) S08001. http://stacks.iop.org/1748-0221/3/i=08/a=S08001.

[29] W. Stirling and E. Vryonidou, *Electroweak gauge boson polarisation at the LHC*, Journal of High Energy Physics **2012** no. 7, (2012), arXiv:1203.2165v2 [hep-ph]. http://dx.doi.org/10.1007/JHEP07%282012%29124.

[30] E. Mirkes, *Angular decay distribution of leptons from W bosons at NLO in hadronic collisions*, Nucl.Phys. **B387** no. TTP-92-12, (1992) 3–85.

[31] ATLAS Collaboration, G. Aad et al, *Measurement of the polarisation of W bosons produced with large transverse momentum in pp collisions at* $\sqrt{s} = 7$ *TeV with the ATLAS experiment*, The European Physical Journal C **72** no. 5, (2012), arXiv:1203.2165v2 [hep-ex]. http://dx.doi.org/10.1140/epjc/s10052-012-2001-6.

[32] P. Anger, M. Kobel, and S. Lammers, *Probing Electroweak Gauge Boson Scattering with the ATLAS Detector at the Large Hadron Collider*. PhD thesis, Dresden, Tech. U., Jun, 2014. https://cds.cern.ch/record/1753849. Presented 01 Sep 2014.

[33] M. S. Chanowitz and M. K. Gaillard, *Multiple production of W and Z as a signal of new strong interactions*, Physics Letters B **142** no. 1–2, (1984) 85 – 90. http://www.sciencedirect.com/science/article/pii/0370269384911419.

[34] B. W. Lee, C. Quigg, and H. B. Thacker, *Weak interactions at very high energies: The role of the Higgs-boson mass*, Phys. Rev. D **16** (1977) 1519–1531. http://link.aps.org/doi/10.1103/PhysRevD.16.1519.

[35] P. Anger et al, *A Measurement of WZ Production in Proton-Proton Collisions at* $\sqrt{\mathbf{s}} = \mathbf{8}$ *TeV with the ATLAS Detector*, Tech. Rep. ATL-COM-PHYS-2014-144, CERN, Geneva, Feb, 2014. https://cds.cern.ch/record/1663539. Access restricted to ATLAS members.

[36] J.-L. Caron, "The LHC injection complex. L'ensemble d'injection du LHC.." AC Collection. Legacy of AC. Pictures from 1992 to 2002., May, 1993.

[37] *Collection of information about LHC*, Feb., 2015. http://www.lhc-facts.ch/index.php?page=home.

[38] ATLAS Collaboration, G. Aad et al, *The ATLAS Experiment at the CERN Large Hadron Collider*, Journal of Instrumentation **3** no. 08, (2008) S08003. http://stacks.iop.org/1748-0221/3/i=08/a=S08003.

[39] CMS Collaboration, S. Chatrchyan et al, *The CMS experiment at the CERN LHC*, Journal of Instrumentation **3** no. 08, (2008) S08004. http://stacks.iop.org/1748-0221/3/i=08/a=S08004.

[40] ALICE Collaboration, K. Aamodt et al, *The ALICE experiment at the CERN LHC*, Journal of Instrumentation **3** no. 08, (2008) S08002. http://stacks.iop.org/1748-0221/3/i=08/a=S08002.

[41] LHCb Collaboration, Augusto Alves Jr et al, A, *The LHCb Detector at the LHC*, Journal of Instrumentation **3** no. 08, (2008) S08005. http://stacks.iop.org/1748-0221/3/i=08/a=S08005.

[42] TOTEM Collaboration, G. Anelli et al, *The TOTEM Experiment at the CERN Large Hadron Collider*, Journal of Instrumentation **3** no. 08, (2008) S08007. http://stacks.iop.org/1748-0221/3/i=08/a=S08007.

[43] LHCf Collaboration, O. Adriani et al, *The LHCf detector at the CERN Large Hadron Collider*, Journal of Instrumentation **3** no. 08, (2008) S08006. http://stacks.iop.org/1748-0221/3/i=08/a=S08006.

[44] MoEDAL Collaboration, J. Pinfold et al, *Technical Design Report of the MoEDAL Experiment*, Tech. Rep. CERN-LHCC-2009-006. MoEDAL-TDR-001, CERN, Geneva, Jun, 2009. https://cds.cern.ch/record/1181486.

[45] C. Pralavorio, *LHC restart back on track*, 2015. http://home.web.cern.ch/about/updates/2015/03/lhc-restart-back-track.

[46] C. O'Luanaigh, *Proton beams are back in the LHC*, 2015. http://home.web.cern.ch/about/updates/2015/04/proton-beams-are-back-lhc.

[47] C. O'Luanaigh, *First successful beam at record energy of 6.5 TeV*, 2015. http://home.web.cern.ch/about/updates/2015/04/first-successful-beam-record-energy-65-tev.

[48] D. Berdine, N. Kauer, and D. Rainwater, *Breakdown of the Narrow Width Approximation for New Physics*, Phys. Rev. Lett. **99** (2007) 111601, arXiv:0703058v2 [hep-ph]. http://link.aps.org/doi/10.1103/PhysRevLett.99.111601.

[49] P. Richardson, *Spin correlations in Monte Carlo simulations*, Journal of High Energy Physics **2001** no. 11, (2001) 029, arXiv:0110108 [hep-ph]. http://stacks.iop.org/1126-6708/2001/i=11/a=029.

[50] W. Kilian, T. Ohl, and J. Reuter, *WHIZARD: Simulating Multi-Particle Processes at LHC and ILC*, Eur.Phys.J. **C71** (2011) 1742, arXiv:0708.4233 [hep-ph].

[51] M. Moretti, T. Ohl, and J. Reuter, *O'Mega: An Optimizing matrix element generator*, arXiv:0102195 [hep-ph].

[52] M. Dobbs and J. B. Hansen, *The HepMC C++ Monte Carlo event record for High Energy Physics*, Computer Physics Communications **134** no. 1, (2001) 41 – 46. http://www.sciencedirect.com/science/article/pii/S0010465500001892.

[53] J. E. Gerken, "Spin correlations in bsm cascades.".

[54] J. Alwall, R. Frederix, S. Frixione, V. Hirschi, F. Maltoni, O. Mattelaer, H.-S. Shao, T. Stelzer, P. Torrielli, and M. Zaro, *The automated computation of tree-level and next-to-leading order differential cross sections, and their matching to parton shower simulations*, Journal of High Energy Physics **2014** no. 7, (2014), arXiv:1405.0301 [hep-ph]. http://dx.doi.org/10.1007/JHEP07%282014%29079.

[55] J. Alwall et al, *A standard format for Les Houches Event Files*, Computer Physics Communications **176** no. 4, (2007) 300 – 304, arXiv:0609017 [hep-ph]. http://www.sciencedirect.com/science/article/pii/S0010465506004164.

[56] O. Mattelaer, *How to generate polarized particles*, Apr., 2015. https://answers.launchpad.net/mg5amcnlo/+faq/2243.

[57] P. Artoisenet, R. Frederix, O. Mattelaer, and R. Rietkerk, *Automatic spin-entangled decays of heavy resonances in Monte Carlo simulations*, Journal of High Energy Physics **2013** no. 3, (2013), arXiv:1212.3460 [hep-ph]. http://dx.doi.org/10.1007/JHEP03%282013%29015.

[58] S. Frixione, E. Laenen, P. Motylinski, and B. R. Webber, *Angular correlations of lepton pairs from vector boson and top quark decays in Monte Carlo simulations*, Journal of High Energy Physics **2007** no. 04, (2007) 081, arXiv:0702198 [hep-ph]. http://stacks.iop.org/1126-6708/2007/i=04/a=081.

[59] CMS Collaboration, S. Chatrchyan et al, *Measurement of the Polarization of W Bosons with Large Transverse Momenta in W + jets Events at the LHC*, Phys. Rev. Lett. **107** (2011) 021802, arXiv:1104.3829 [hep-ex]. http://link.aps.org/doi/10.1103/PhysRevLett.107.021802.

[60] A. Buckley, J. Butterworth, D. Grellscheid, H. Hoeth, L. Lönnblad, J. Monk, H. Schulz, and F. Siegert, *Rivet user manual*, Computer Physics Communications **184** no. 12, (2013) 2803 – 2819, arXiv:1003.0694 [hep-ph]. http://www.sciencedirect.com/science/article/pii/S0010465513001914.

[61] T. Sjöstrand, S. Mrenna, and P. Skands, *PYTHIA 6.4 physics and manual*, Journal of High Energy Physics **2006** no. 05, (2006) 026, arXiv:0603175 [hep-ph]. http://stacks.iop.org/1126-6708/2006/i=05/a=026.

[62] K. Doroba, J. Kalinowski, J. Kuczmarski, S. Pokorski, J. Rosiek, M. Szleper, and S. Tkaczyk, *$W_L W_L$ scattering at the LHC: Improving the selection criteria*, Phys. Rev. D **86** (2012) 036011, arXiv:1201.2768v2 [hep-ph]. http://link.aps.org/doi/10.1103/PhysRevD.86.036011.

[63] *MadSpin Changes the state of polarization only for w-boson*, Apr., 2015. https://answers.launchpad.net/mg5amcnlo/+question/259520.

[64] C. Bittrich, Apr., 2015. https://github.com/carstenbittrich/WZdecay.

[65] C. Bittrich, Apr., 2015. https://svnweb.cern.ch/cern/wsvn/atlas-cbittric/WZdecay.

[66] I. Antcheva et al, *ROOT — A C++ framework for petabyte data storage, statistical analysis and visualization*, Computer Physics Communications **180** no. 12, (2009) 2499 – 2512. http://www.sciencedirect.com/science/article/pii/S0010465509002550.

[67] J. C. Collins and D. E. Soper, *Angular distribution of dileptons in high-energy hadron collisions*, Phys. Rev. D **16** (1977) 2219–2225. http://link.aps.org/doi/10.1103/PhysRevD.16.2219.

[68] G. Cowan, K. Cranmer, E. Gross, and O. Vitells, *Asymptotic formulae for likelihood-based tests of new physics*, The European Physical Journal C **71** no. 2, (2011), arXiv:1007.1727 [physics.data-an]. http://link.springer.com/article/10.1140%2Fepjc%2Fs10052-011-1554-0#.

Danksagung

An dieser Stelle möchte ich mich bei allen bedanken, die zum Gelingen dieser Arbeit und meines Studiums beigetragen haben.

Besonders möchte ich mich bei meinem Betreuer Prof. Michael Kobel für die Möglichkeit bedanken, an diesem interessanten und zukunftsträchtigem Thema arbeiten zu können. Sein Engagement in fachlichen, aber auch in außeruniversitären Themen beeindruckt mich immer wieder und ich bin froh, durch ihn den Weg in die Teilchenphysik gefunden zu haben.

Außerdem bedanke ich mich bei der gesamten VBS-Arbeitsgruppe. Durch die gute Arbeitsathmosphäre habe ich mich immer wohlgefühlt und selbst arbeitsreiche Zeiten haben immer Spaß gemacht. Besonderer Dank geht an Philipp Anger, Christian Gumpert, Ulrike Schnoor, Felix Socher und Anja Vest, mit denen ich sowohl während meiner Bachelor- als auch meiner Masterarbeit arbeiten konnte und viel gelernt habe. Vielen Dank an Stefanie Todt für die vielen Diskussionen und Hinweise, vergangene wie auch noch vor uns liegende. Aber auch bei Christian Gütschow, Johannes Krause, Alexander Melzer, Tobias Sandmann, Lukas Schroeder und Frank Siegert bedanke ich mich für die vielen lustigen Stunden von denen wir vermutlich zu viele am Kickertisch verbracht haben. Bei Philipp Anger, Christian Gumpert, Christian Gütschow, Alexander Melzer, Ulrike Schnoor, Felix Socher, Ulrike Schnoor, Stefanie Todt und Anja Vest bedanke ich mich außerdem fürs Korrekturlesen dieser Arbeit.

Bei David Kirchmeier und Theresa Werner bedanke ich mich für die Begleitung während des Studiums. Dank ihnen haben sogar die üblichen Lernexzesse Spaß gemacht. Vielen Dank fürs gemeinsame Lernen, vielen Dank für die Motivation, vielen Dank für die vielen lustigen Stunden, und vor allem vielen Dank für die stetige Erinnerung daran, dass es auch ein Leben außerhalb des Studiums gibt!

Vielen Dank auch an meine Eltern und Robert für die Unterstützung auch in schweren Zeiten, finanziell und emotional. Sie sind mir stets gute Vorbilder, wofür ich sehr dankbar bin.

Zu guter Letzt herzlichen Dank an Jane, die mich seit vielen Jahren stets begleitet und unterstützt. Außerdem gibt sie mir stets Kraft und Motivation an mir und meinen Zielen zu arbeiten. Vielen Dank für die unzähligen schönen Momente, vielen Dank fürs aus-dem-Herzen-sprechen, vielen Dank, dass es dich gibt!

Erklärung

Hiermit erkläre ich, dass ich diese Arbeit im Rahmen der Betreuung am `Institut für Kern- und Teilchenphysik` ohne unzulässige Hilfe Dritter verfasst habe. Die aus fremden Quellen direkt oder indirekt übernommenen Gedanken sind als solche kenntlich gemacht. Die Arbeit wurde bisher weder im Inland noch im Ausland in gleicher oder ähnlicher Form einer anderen Prüfungsbehörde vorgelegt.

Carsten Bittrich
Dresden, 27.04.2015